JACS
JOURNAL OF THE AMERICAN CHEMICAL SOCIETY

pubs.acs.org/JACS

Perspective

Solid-State NMR and NQR Spectroscopy of Lead-Halide Perovskite Materials

Laura Piveteau, Viktoriia Morad, and Maksym V. Kovalenko*

Cite This: J. Am. Chem. Soc. 2020, 142, 19413−19437

Read Online

ACCESS | Metrics & More | Article Recommendations

ABSTRACT: Two- and three-dimensional lead-halide perovskite (LHP) materials are novel semiconductors that have generated broad interest owing to their outstanding optical and electronic properties. Characterization and understanding of their atomic structure and structure−property relationships are often nontrivial as a result of the vast structural and compositional tunability of LHPs as well as the enhanced structure dynamics as compared with oxide perovskites or more conventional semiconductors. Nuclear magnetic resonance (NMR) spectroscopy contributes to this thrust through its unique capability of sampling chemical bonding element-specifically ($^{1/2}$H, ^{13}C, $^{14/15}$N, $^{35/37}$Cl, ^{39}K, $^{79/81}$Br, ^{87}Rb, ^{127}I, ^{133}Cs, and ^{207}Pb nuclei) and locally and shedding light onto the connectivity, geometry, topology, and dynamics of bonding. NMR can therefore readily observe phase transitions, evaluate phase purity and compositional and structural disorder, and probe molecular dynamics and ionic motion in diverse forms of LHPs, in which they can be used practically, ranging from bulk single crystals (e.g., in gamma and X-ray detectors) to polycrystalline films (e.g., in photovoltaics, photodetectors, and light-emitting diodes) and colloidal nanocrystals (e.g., in liquid crystal displays and future quantum light sources). Herein we also outline the immense practical potential of nuclear quadrupolar resonance (NQR) spectroscopy for characterizing LHPs, owing to the strong quadrupole moments, good sensitivity, and high natural abundance of several halide nuclei ($^{79/81}$Br and ^{127}I) combined with the enhanced electric field gradients around these nuclei existing in LHPs as well as the instrumental simplicity. Strong quadrupole interactions, on one side, make $^{79/81}$Br and ^{127}I NMR rather impractical but turn NQR into a high-resolution probe of the local structure around halide ions.

1. INTRODUCTION TO LEAD-HALIDE PEROVSKITES

Lead-halide perovskites (LHPs) of an $APbX_3$ composition, where A is Cs, methylammonium (MA), or formamidinium (FA) and X = Cl, Br, I, or mixtures thereof, are compounds isostructural to diverse ABO_3-type oxide perovskites. LHPs have recently become a major class of optoelectronic materials owing to their exceptional electronic and optical characteristics.[1−4] These materials are intensely pursued for applications in photovoltaics,[5−10] LCD technologies,[11−13] light-emitting diodes (LEDs),[4,14−16] lasers,[17−20] UV−vis−near-IR photodetectors,[21−28] direct conversion X-ray and gamma detectors,[9,29−36] and scintillators[37,38] and as emerging quantum light sources.[39,40] In these applications, LHPs are used in their diverse forms, as single crystals, thick or thin films, and colloidal nanocrystals (NCs, Figure 1a−f), which are easy to produce by means of solution-phase chemistry or low-temperature melt-growth.[31,41−43] The remarkable characteristics of these materials include long carrier lifetime−mobility products and low densities of electronic traps (on par with GaAs and CdTe)[44−46] despite the large concentrations of structural defects and the enhanced structure dynamics, a seeming paradox often referred to as defect tolerance.[4,47−52] Perovskite $CsPbBr_3$ gamma detectors exhibit energy resolution better than commercial CdTe-based detectors.[30,31,34,53] Perovskite X-ray detectors[54] and UV−vis detectors[21,55,56] exhibit high sensitivities on the order of 10^3 μC Gy^{1-} cm^{-2} and detectivities up to 10^{14} Jones, respectively, which compare favorably with respective commercial technologies. Thin-film solar cells with perovskites as light absorbers exhibit power conversion efficiencies (25.2%)[10,57] that surpass polycrystalline Si and essentially all emerging thin-film technologies and approach the single-crystalline Si world record (26.1%).[10,58] Colloidal ligand-capped LHP NCs (Figure 1b,c) are the first examples of colloidal quantum dots (QDs) exhibiting near-unity photoluminescence quantum yields (PL QYs) across the entire visible spectral range without the need for epitaxial overcoating for electronic passivation.[4,47] These NCs are also shown to exhibit long exciton coherence times and near-transform-limited emission line widths,[39,59] which, along with stable single photon emission,[60,61] makes them attractive for designing future sources of quantum light.[39,40,62]

The crystal structure of $APbX_3$ perovskites is characterized by the 3D corner-interconnection of PbX_6 octahedra. Several polymorphs of such 3D LHPs exist as a result of the octahedral tilting and orientation of the A cation, thus reducing the symmetry from the archetypical cubic phase (to tetragonal, orthorhombic, or monoclinic) and deviating the Pb−X−Pb bond angles from the initial value of 180°. For instance, at room

Received: July 8, 2020
Published: September 28, 2020

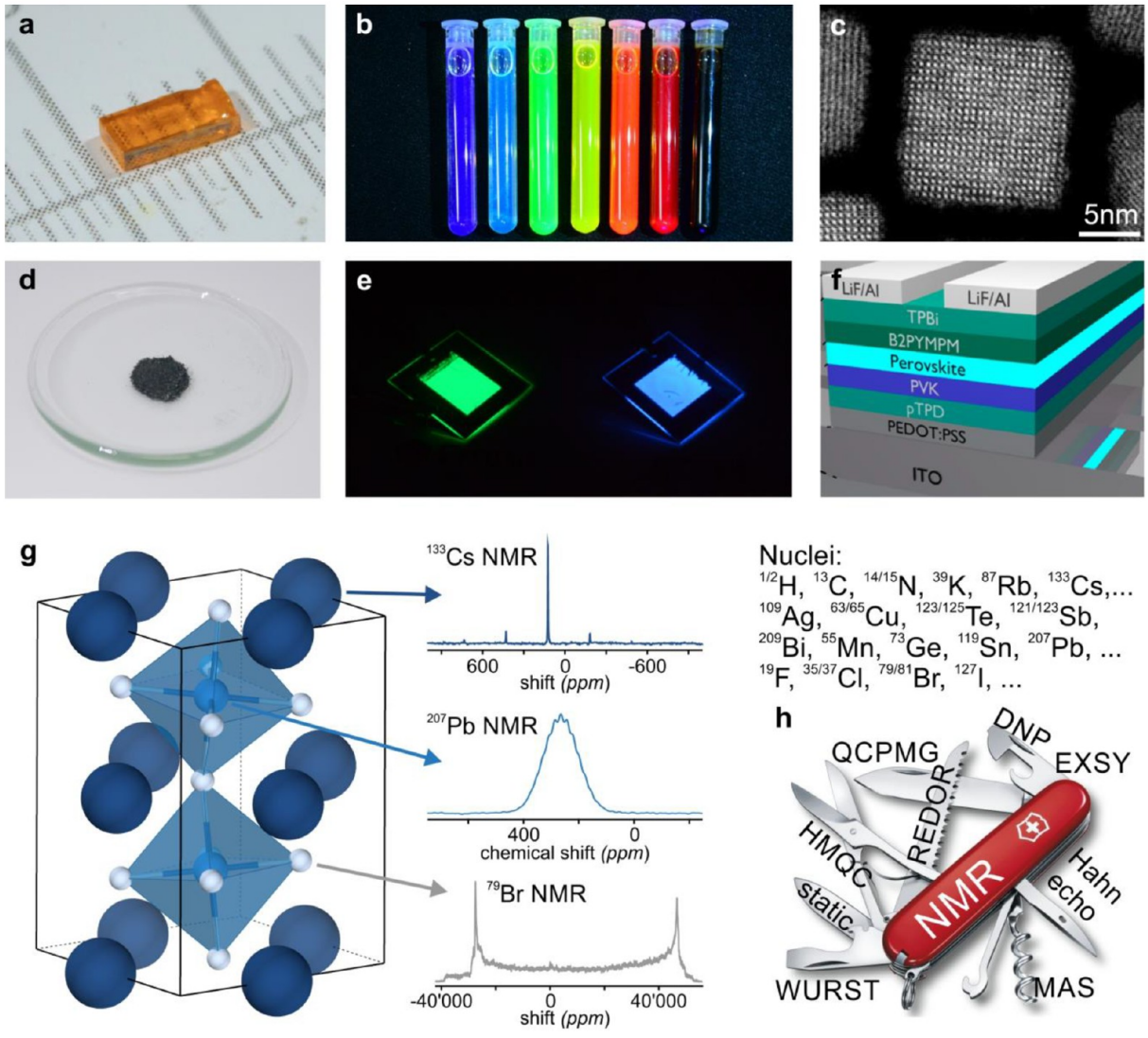

Figure 1. LHP materials and the utility of NMR spectroscopy for their characterization. 3D and 2D LHPs are of practical interest in their various forms: (a) single crystals (Adapted with permission from ref 36. Copyright 2016 American Chemical Society) and (d) bulk powders, (b,c) colloidal NCs (Panel b Credit: Nadia Schwitz; Panel c Credit: Frank Krumeich), and (e,f) continuous films within optoelectronic devices (green and blue LEDs as examples) (Panel e Credit: Yevhen Shynkarenko; Panel f reprinted with permission from ref 83. Copyright 2019 American Chemical Society). (g) All elements of $APbX_3$ LHPs possess NMR-active isotopes, as exemplified for $CsPbBr_3$ using actual solid-state NMR spectra. (h) Modern NMR spectroscopy methods make for a versatile characterization toolbox. Depending on the probed spin interaction (Figure 2) and the structural aspect in question (Figure 3), a diverse range of pulse sequences and signal and resolution enhancing techniques are available (e.g., QCPMG, quadrupolar Carr−Purcell−Meiboom−Gill; REDOR, rotational-echo double resonance; DNP, dynamic nuclear polarization; EXSY, exchange spectroscopy; HMQC, heteronuclear multiple-quantum correlation; WURST, wideband, uniform rate, smooth truncation; MAS, magic-angle spinning). Image of Swiss Army Knife used with permission from Victorinox AG.

temperature (RT), the stable LHP polymorphs are cubic $FAPbBr_3$, $MAPbCl_3$, $MAPbBr_3$, and $FAPbCl_3$, tetragonal $MAPbI_3$, orthorhombic $CsPbBr_3$ (Figure 1d), and monoclinic $CsPbCl_3$, whereas $CsPbI_3$ and $FAPbI_3$ crystallize in non-perovskite 1D polymorphs (with edge- and face-sharing connectivity, respectively).[63−76] The structural instability of the perovskite phases for $CsPbI_3$ and $FAPbI_3$ stems from Cs and FA cations being, respectively, too small and too large to optimally fill the A site.[77−82] Interestingly, stable perovskite phases can be obtained with mixed-ionic compositions $(Cs/FA)PbI_3$ or $(Cs/FA)Pb(Br/I)_3$.[8,84−88] The substitutional A-site doping by other monovalent cations, such as Rb^+, K^+, guanidinium (G), azetidinium, or dimethylammonium (DMA), reportedly results in improved device performance or higher material stability.[89−97] The incorporation of a larger ethylendiammonium cation requires the concomitant formation of lead and halide vacancies, yielding so-called hollow LHPs.[98] The halides and the octahedral tilts define the band-gap energies of LHPs (ca. 1.5−3.0 eV).[99−101] Perovskite lattices also form upon the substitution of Pb^{2+} with Sn^{2+} or Ge^{2+}[76,102−109] or by a combination of monovalent and trivalent cations (e.g., Ag^+, Cu^+, Bi^{3+}, In^{3+}, and Sb^{3+} in so-called double perovskites).[109−114] These lead-free perovskites thus far fall behind in their optoelectronic quality due to both the different electronic structures (flat bands, indirect transitions in double perovskites, etc.)[115] and the limited stability.[84,115]

Recent years have seen a surge of activities beyond $APbX_3$, namely, in 2D LHPs, which are often reported to exhibit greater

https://dx.doi.org/10.1021/jacs.0c07338
J. Am. Chem. Soc. 2020, 142, 19413−19437

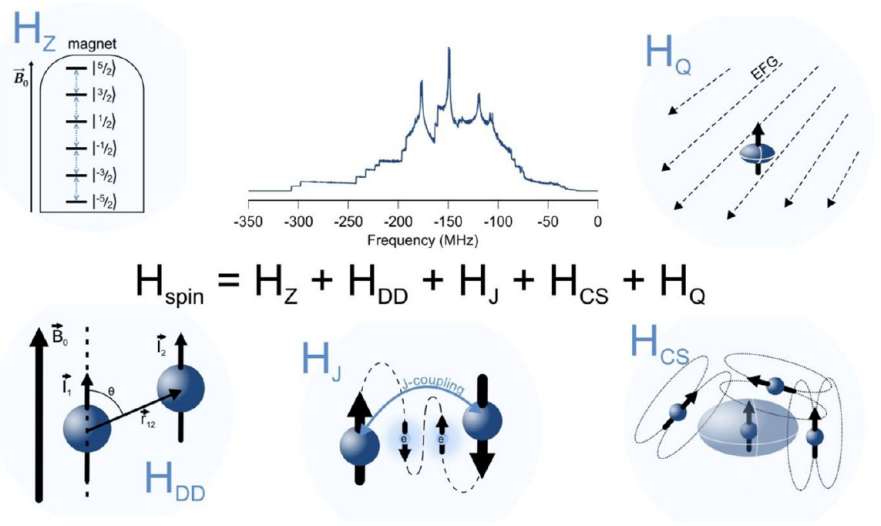

Figure 2. Major interactions contributing to NMR spectra. In NMR spectroscopy, the spin energy transitions are studied. By applying an external magnetic field, the Zeeman interaction (H_Z) lifts the degeneracy between nuclear spin states. A spin of $I = 5/2$ is shown, in the absence of other spin interactions. Spin−spin interactions such as the dipolar coupling (H_{DD}) or the J-coupling (H_J) perturb the spin energies and so do deviations of the local magnetic field relative to the applied magnetic field by shielding and deshielding of neighboring spins (chemical shielding, H_{CS}). Also, nearby charges affect the spin energies through the coupling of the quadrupole moments of spins of $I > 1/2$ with the electric field gradient (EFG) generated by these charges (quadrupole interaction, H_Q). The NMR spectrum, which reflects the spin energy transitions, is affected by all of these interactions through the shift of the resonance frequency, signal broadening, shape distortion, generation of multiplets and tensor line shapes, and so on. Here a simulated ^{127}I NMR spectrum of $MAPbI_3$ at 16.4 T is shown as an illustration of the complexity that NMR spectra can exhibit. For a detailed discussion and mathematical descriptions of these interactions, the interested reader is referred to several NMR textbooks.[175−177]

stability[116,117] and wherein structural variety can be realized by disrupting the connectivity in one dimension, for example, by cutting 3D perovskites into 2D slabs of adjustable thickness.[118−121] Most common are cuts along the <100> direction, as in Dion−Jacobson[122] and Ruddlesden−Popper[123] types, or structures with alternating cations in the interlayer space.[124] 2D slab thicknesses n (number of octahedral layers within the slab) are typically in the range of $n = 1−7$.[121,125−128] The interlayer region comprises bulky spacers, such as long-chain alkyl-, aryl-,[129] adamantantyl-,[130] alkylphenyl-[120] ammonium, and heterocyclic (e.g., benzimidazolium[131] or quaterthiophene derivatives)[132] cations. In general, owing to quantum and dielectric confinement, layered perovskites behave as multiple quantum-well structures,[133,134] with band-gap and exciton binding energies decreasing for larger n.[123,135,136] Larger exciton binding energies and cascade energy structures[137] favor fast radiative recombination, as required in, for instance, LEDs.[138,139] Smaller binding energies ($n > 3$) lead to efficient exciton dissociation into free carriers, as needed in photovoltaics[119,140] and photodetectors.[141,142] Octahedral distortions and tilts within 2D slabs give rise to piezo- and ferroelectric responses.[129,143,144] The chirality of the organic cations allows for the emission or detection of polarized light[145−148] and nonlinear optical responses.[149−152] Static and dynamic structural distortions and defects have a profound impact on the PL line widths and PL QYs (energetic disorder, exciton−phonon coupling, etc.).[117,153−155] Because of their strong spin−orbit coupling, 3D LHPs have long been considered for spintronic applications, and whereas the Rashba effect has been observed experimentally,[156,157] its origin in these applications remains uncertain.[158,159] The reduced dimensionality of 2D perovskites favors symmetry reduction, resulting in larger Rashba splitting.[160,161] Moreover, the manipulation of spin polarization and spin funneling has been recently demonstrated in 2D perovskites.[162−164]

The in situ formation of 2D perovskites at the interfaces or grain boundaries or as individual grains is often invoked in explaining the favorable effects of the addition of bulkier cations into standard protocols for the deposition of 3D perovksite films in optoelectronics.[165−170] Oftentimes, the exact structure of these concomitant phases remains unknown.

We also note that there exist nonperovskite lead halides with 1D corner-sharing or full disconnection of PbX_6 octahedra or those formed by face- and edge-sharing of PbX_6 octahedra as well as compounds with nonoctahedral coordination of Pb.[155,171] These compounds comprise electronically isolated states and hence bound or self-trapped excitons with the characteristic broadband emission and a steep temperature-dependent PL QY.[155,172] Such metal halides are also of great interest for optoelectronics and structural chemistry per se[171,173,174] and will benefit from the development of the magnetic resonance methods.

LHPs represent a transitional case in between rigid crystalline materials and soft, dynamic, and disordered matter. It remains counterintuitive how the defect tolerance emerges, that is, how highly intrinsic electronic and optical characteristics are retained and not hampered by the structural defectiveness and structural dynamics, both being greatly enhanced in comparison with the structurally more rigid, conventional semiconductors. In fact, soft lattices of these halides are increasingly considered to be a favorable factor.[178−181] In particular, the association of charge carriers with lattice vibrations—so-called polarons—may protect carriers from defect states and increase carrier lifetimes, can aid in exciton dissociation, and may slow carrier cooling. Polarons are also increasingly associated with the unusually high dielectric constants in LHPs. The broad compositional and structural engineerability of LHPs makes it possible to engineer their properties à la carte. There exists no perfect and universal structural characterization method for probing the atomic structure both statically and dynamically as well as locally and

https://dx.doi.org/10.1021/jacs.0c07338
J. Am. Chem. Soc. 2020, 142, 19413−19437

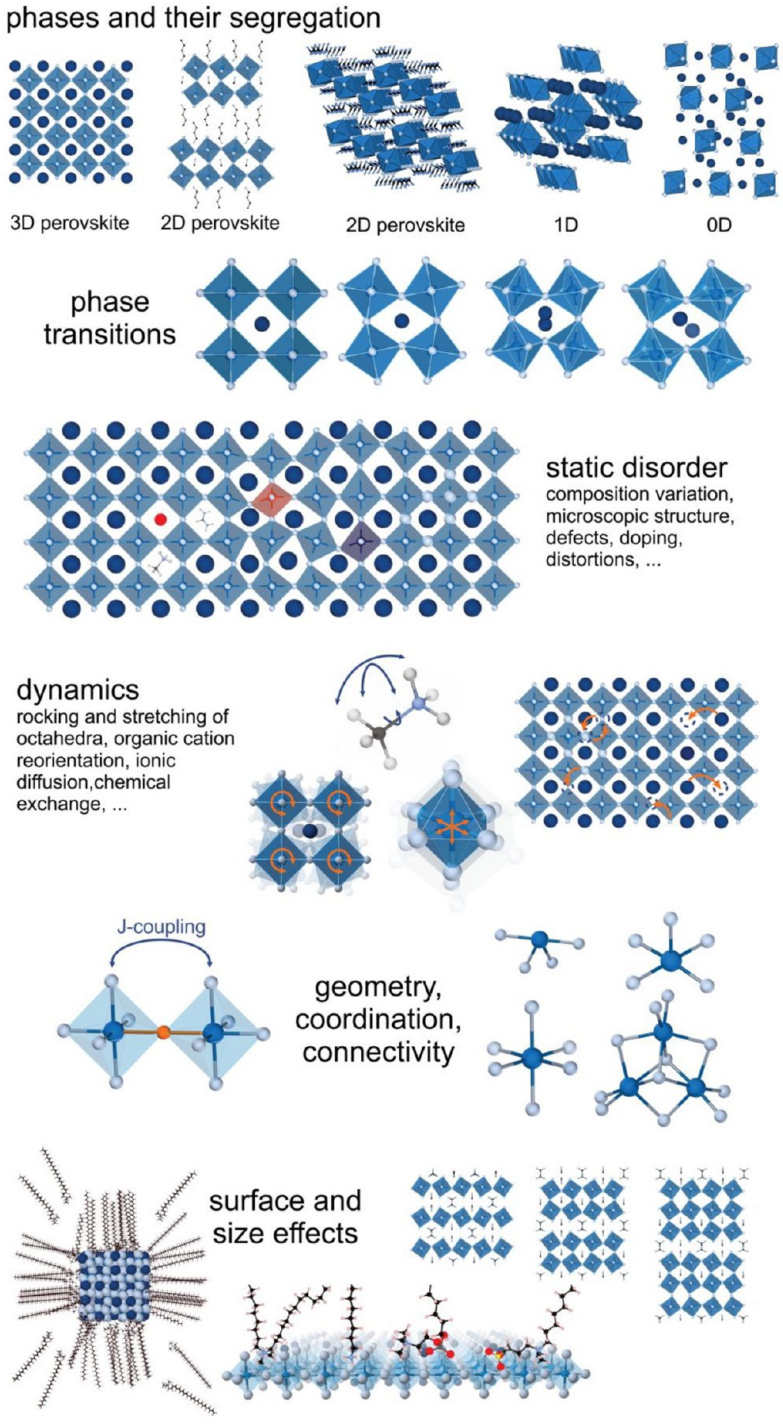

Figure 3. Structural insights about LHPs accessible through NMR and NQR. The figure illustrates a nonexhaustive range of structural aspects that are within the reach of magnetic resonance methods. Besides these structural and chemistry insights, electronic effects of quantum size effects and dielectric confinement are addressable as well.

space-averaged. It is the entirety of observations from diverse methods that allows the complex structure−property relationships to be unveiled. Typically, detailed structural investigations into a new class of inorganic materials start with X-ray/electron/neutron diffraction methods and electron microscopy and may be complemented by vibrational spectroscopy. Time-resolved variants of these methods and their combinations with optical methods give an extra benefit of probing the structure dynamics or excited states.[182,183] This Perspective emphasizes and exemplifies the immense utility of magnetic resonance methods for characterizing LHPs and other metal halide materials and outlines future avenues in this field.

2. UTILITY OF NMR AND NQR FOR LEAD-HALIDE PEROVSKITES

Solid-state nuclear magnetic resonance (NMR) spectroscopy is a versatile tool for sampling the chemical nature, geometry, and topology of the surrounding of atomic nuclei as well as the structure dynamics in materials without prerequisites for the

https://dx.doi.org/10.1021/jacs.0c07338
J. Am. Chem. Soc. 2020, 142, 19413−19437

crystallinity, size, or composition of the sample. All elements constituting LHPs possess NMR-active isotopes (i.e., nuclei with a spin), such as ^{1}H, ^{13}C, $^{14/15}$N, ^{19}F, $^{35/37}$Cl, $^{39/41}$K, ^{55} Mn, $^{63/65}$Cu, ^{73}Ge, $^{79/81}$Br, $^{85/87}$Rb, $^{107/109}$Ag, ^{119}Sn, $^{121/123}$Sb, $^{123/125}$Te, ^{127}I, ^{133}Cs, ^{207}Pb, and ^{209}Bi (Figure 1g,h). NMR spectroscopy is highly chemical-element-specific, as each isotope has a different Larmor frequency (ω_0) corresponding to the Zeeman splitting in the applied magnetic field and hence a very specific frequency range of the NMR signals. NMR spectroscopy is a high-resolution probe of the various interactions of the nuclear spin with other nuclear and electron spins or electromagnetic fields (Figure 2). Spin−spin interactions can provide, for instance, information about connectivity (J-coupling, H_J) or interatomic distance (dipolar coupling, H_{DD}), whereas spectral features produced by the surrounding magnetic field (chemical shift, H_{CS}) and electric field gradient (EFG, quadrupole interaction, H_Q) contain information about the nature and the geometry of the chemical species. Low crystallinity, static and dynamic structural disorder, concomitant phases, and impurities, all being recurring matters in LHP research (Figure 3), are seen very differently by NMR as compared with diffraction-based methods. This important complementarity of NMR methods for LHPs is evident from the surge of research articles containing solid-state multinuclear NMR data. Several recent review articles may serve as initial guidance to the present stake of NMR in LHPs. Franssen et al. reviewed the structural and dynamical aspects,[184] whereas Bernard et al. unified models and provided a perspective about the dynamics of MA in $MAPbX_3$.[185] In their perspective about the "ionics in hybrid halide perovskite", Senocrate et al. summarized insights into the ion conduction in LHP obtained with NMR spectroscopy.[186]

In this Perspective, we bring the reader's attention to the vast insights that NMR spectroscopy yields about the structure and structure dynamics of diverse LHPs (2D and 3D compounds, from NCs to bulk single crystals). We then discuss prospects that highlight the complementarity of nuclear quadrupole resonance (NQR) for $^{79/81}$Br and ^{127}I nuclei, possessing particularly large quadrupole moments and, in LHPs, exhibiting strong quadrupole interactions due to large EFGs. We also underline that a better understanding of the structure dynamics in LHPs should leverage rapid development in computational materials science (i.e., *ab initio* molecular dynamics (AIMD) and its combinations with classical molecular dynamics as well as density functional theory (DFT) calculations).[187−189]

Diverse structural and dynamic aspects of LHP materials (Figure 3) can be studied by both NMR and NQR methods. Various lead-halide compounds and, for an individual compound, also different polymorphs (phase transitions, coexistence of polymorphs) can be readily resolved as signals with different resonance frequencies (usually different chemical shifts in NMR).[190−197] Static disorder in LHPs comprises (i) structural defects such as point defects (e.g., halide vacancies), interstitial atoms, stacking faults, and grain boundaries and (ii) compositional modulations such as the mixed-ionic occupation of lattice sites, ion segregation, and compositional gradients (typical for halide ions) as well as heteroatomic doping. Static disorder is seen as inhomogeneous broadening generated by the distribution of chemical surroundings, forming a continuum of resonance frequencies that define the signal shape. For certain types of defects (e.g., paramagnetic dopants), relaxation of the nuclear spins can be affected as well. The rich structural dynamics in LHPs ranges from the rotational and stretching freedom of the organic constituents or the various stretching and tilting modes of the lead-halide framework to rapid ionic motion. These dynamic processes can be probed through the temporal variation of spin interactions. Depending on the nature and the time scale of the dynamics, the relaxation behavior or the shape and position of the signal may be affected, oftentimes accompanied by significant homogeneous broadening of the respective signals. Surfaces become a chemically distinct feature in high-surface-area LHP materials, such as ligand-capped colloidal NCs or matrix-embedded NCs. NMR offers diverse handles to probe such surfaces by surface-selective excitation (e.g., through cross-polarization), signal enhancing methods (e.g., dynamic nuclear polarization (DNP)), as well as correlation and other types of 2D experiments. Finally, electronic effects of size quantization and dielectric confinement in colloidal LHP NCs or 2D LHPs are also within the reach of NMR spectroscopy. These can be investigated through, for instance, susceptibility effects or quadrupole and chemical shift interactions (paramagnetic shielding term).

3. A-CATIONS: DYNAMICS AND SURFACES

There are only three monovalent cations known to form 3D $APbX_3$—MA^+, FA^+, and Cs^+—owing to their geometric fitness into the 12-coordinate A-site.[198] Mixing these A-cations, concomitantly with mixing halides, is presently the most successful strategy for obtaining best-performing perovskite solar cells. For instance, the incorporation of MA or Cs stabilizes cubic $FAPbI_3$ against spontaneous transition into a non-perovskite lattice. Examples of such heavily substituted multinary perovskites include $FA_{0.83}Cs_{0.17}Pb(I_{0.6}Br_{0.4})_3$,[199] $(FA_{0.3}MA_{0.7})_{0.85}Cs_{0.15}PbI_3$,[200] and $FA_{0.79}MA_{0.16}Cs_{0.05}Pb(I_{0.83}Br_{0.17})_{2.97}$.[201] Further cations (e.g., G and DMA), which are not perovskite formers when used alone, readily incorporate themselves as A-site dopants.[92−95] Interestingly, the analogous substitutional incorporation of the smaller Rb^+ and K^+ onto A-sites was not corroborated by NMR studies, as will be discussed further later. Important pertinent questions that may be addressable with NMR are (i) to what extent different A-cations mix within the perovskite phase, (ii) how they are distributed between different grains, and (iii) the possibility of segregation at the surfaces and interfaces. For instance, the high PL QYs (60−70%) and carrier mobilities (40 $cm^2 V^{-1} s^{-1}$) of potassium-doped $(Cs_{0.06}FA_{0.79}MA_{0.15})Pb(I_{0.85}Br_{0.15})_3$ were attributed to surface and grain-boundary passivation with potassium halides.[96] In MA-free Cs-FA LHP films, the graded A-cation composition of the crystalline grains was rationalized as an inhibiting factor for the transfer of electrons across grain-boundaries.[202] NMR has been used to sample $^{1/2}$H, ^{13}C, $^{14/15}$N, ^{39}K, ^{87}Rb, and ^{133}Cs spins and has permitted us to identify the structural environments of monovalent cations,[192−194,203−219] their dynamics,[185,194,196,206,215,216,219−225] the composition within phases,[98,193,222,226−242] and the distribution between phases of LHPs.[192,193,215,217,222]

Most of the early NMR studies on LHPs focused on $MAPbX_3$ compositions. Starting with the 1985 paper by Wasylishen et al.,[220] the dynamics of the MA cations was assessed through $^{1/2}$H, ^{13}C, and $^{14/15}$N nuclei.[194,196,206,219,221,222,224,225] The MA cation motion can be categorized into two kinds: the fast cone-shaped, wobbling libration (~300 fs in $MAPbI_3$) and the slower, jump-like rotation of the C−N axis of the MA molecule (~3 ps in $MAPbI_3$).[243] The great interest in MA dynamics is attributed to its association with long carrier lifetimes[244] and its

https://dx.doi.org/10.1021/jacs.0c07338
J. Am. Chem. Soc. 2020, 142, 19413−19437

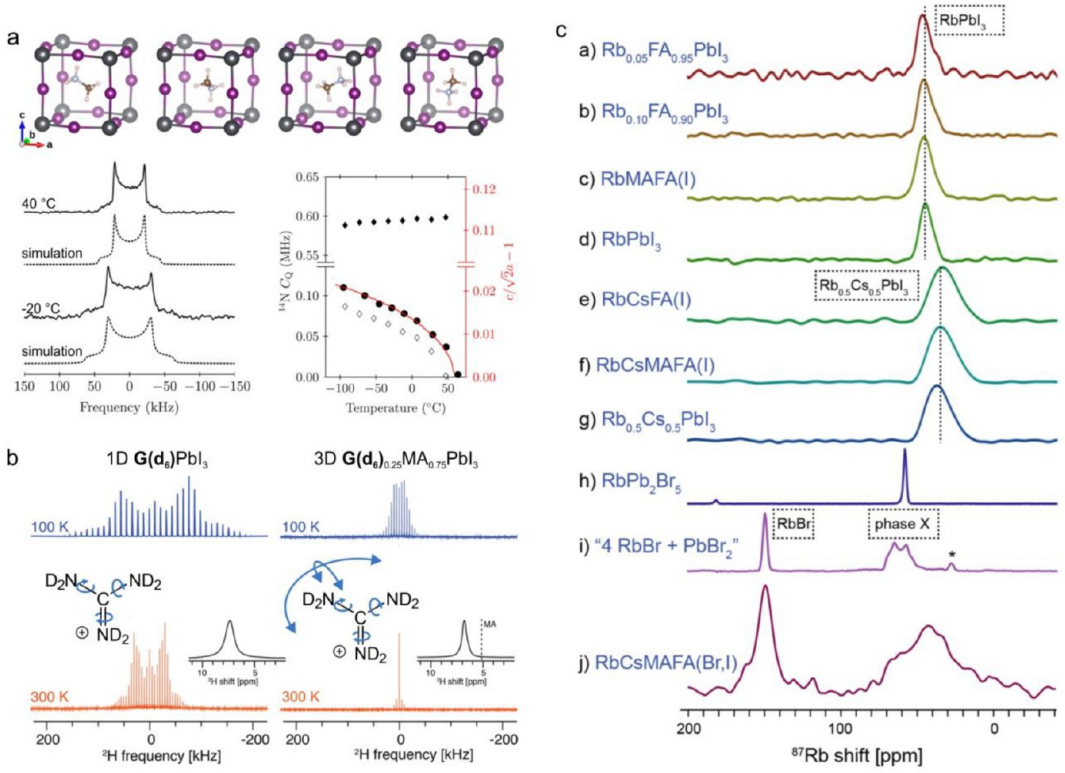

Figure 4. NMR of A-cations in LHPs. (a) Top: Four MA orientations in the crystallographic *ab* plane predicted by Weller et al.[249] Left: Experimental and simulated static ^{14}N solid-state NMR spectra of $MAPbI_3$ spectra. Right: ^{14}N quadrupole coupling constants from the experiment (filled black circles) follow the ratio of the crystallographic *c* and *a* axes with varying temperatures (red, solid line). The filled and empty diamonds represent the individual and the averaged values calculated with DFT for the four MA orientations. Adapted with permission from ref 219. Copyright 2017 American Chemical Society. (b) ^{2}H MAS NMR spectra of $G(d_6)_{0.25}MA_{0.75}PbI_3$ multinary perovskite and 1D $G(d_6)PbI_3$ at 100 and 300 K. Insets are zoom-ins of the center band at higher sample spinning speeds. The dashed line indicates the expected shift of CH_3ND_3. Adapted with permission from ref 215. Copyright 2018 American Chemical Society. (c) Substantial integration of Rb inside the 3D perovskite structure was ruled out, whereas the formation of a 1D structured phase containing Rb could be observed with the help of the ^{87}Rb NMR spectra of $APbX_3$ (A = Cs, FA, MA, Rb; X = Br, I) materials.[192] Reprinted with permission from ref 192. Copyright 2017 American Chemical Society.

contribution to the stabilization of the perovskite electronic structure via hydrogen bonding.[244,245] In general, hydrogen bonding is little studied in LHPs, especially in 2D and lower dimensional derivatives.[246,247] Typical structural characterization methods, that is, X-ray diffraction, are challenging due to the low atomic number of hydrogen. NMR does not experience this limitation. For example, Baikie et al. found, using ^{1}H NMR, that only the amine moiety of MA interacts with the lead-halide framework and used their insights to refine their X-ray and neutron-diffraction data.[221]

The fastest dynamics resolvable with NMR are those affecting the T_1 relaxation rates. Here the theoretical limit corresponds to the Larmor frequency range, which is several tens to hundreds of megahertz (depending on the gyromagnetic ratio of the nucleus and the applied magnetic field strength), corresponding to the time scale of a few picoseconds to several nanoseconds. Even faster dynamics is experienced by the nuclear spins as averaged electromagnetic fields, whereas slower dynamics from a few microseconds up to hundreds of milliseconds impacts T_2 relaxation rates. Slower dynamics (seconds and slower) may also be resolvable, for instance, by the sequential acquisition of spectra. Hence, because of the fast dynamics of MA compared with the NMR time scale, ^{1}H and ^{13}C spectra of $MAPbX_3$ exhibit only narrow lines with a very similar chemical shifts across different halide compositions,[206,209,221,222] but proton T_1 relaxation times change sharply at phase transitions.[196,209,221,248]

Quadrupolar couplings of the nuclear spins ^{14}N and ^{2}H (both spins of $I = 1$) were often used to investigate MA dynamics. ^{14}N and ^{2}H NMR spectra show no quadrupole splitting in the high-symmetry cubic phase due to isotropic spin surroundings and the fast reorientation of MA (Figure 4a).[194,206,219,220,222,224,225] At lower temperatures, $MAPbX_3$ crystallizes in tetragonal and orthorhombic crystal systems, and small quadrupole couplings arise due to the loss of symmetry from the slower dynamics of the MA molecule.[194,206,219,220,224,225] On the basis of the values and the temperature dependence of the line width, the relaxation constants, and the quadrupole coupling strengths, the contribution of the different rotations of MA (correlated and uncorrelated C_3 reorientation along the C−N axis, tunneling rotation, reorientation of the C−N axis, etc.) and their activation energies could be determined,[194,196,206,219−222,224,225] as was comprehensively surveyed in ref 185. DFT calculations were used to determine the exact space group of $MAPbI_3$ at RT.[219] ^{14}N quadrupole couplings constants (C_Q) were calculated for four symmetrically identical orientations of MA in the crystallographic *ab* plane predicted by Weller et al. (top of Figure 4a).[249] The simulated spectra agreed well with the experimentally observed temperature behavior of the static ^{14}N solid-state NMR spectra (Figure 4a). The temperature-dependent experimental and calculated C_Q values follow the ratio of the crystallographic *c* and *a* axes, thus permitting the space group of $MAPbI_3$ to be determined to be *I*4/*mcm*.

https://dx.doi.org/10.1021/jacs.0c07338
J. Am. Chem. Soc. 2020, 142, 19413−19437

There are further studies investigating the dynamics of organic cations in pure-phase ($FAPbBr_3$,[250] $FAPbI_3$)[209,222] and increasingly mixed-ionic LHPs ($FA_{0.67}MA_{0.33}PbI_3$;[222] $G_{0.25}MA_{0.75}PbI_3$,[215] Figure 4b; $DMA_{1-x}MA_xPbI_3$).[251] The capability to distinguish between dynamic and static disorder by separating homogeneous and inhomogeneous line width contributions is not unique to NMR spectroscopy, as, for instance, the PL line width as well as the PL QY and the radiative lifetime are also affected by temporal and spatial disorder.[153−155] However, NMR holds the advantage that the involved chemical structures can be traced because the NMR signals of the concerned structural moieties are the ones exhibiting homogeneous or inhomogeneous line broadening, respectively. By sampling organic and inorganic A-cations in mixed LHPs, insights into the dynamics, the A-cation distribution, and their incorporation are available for a vast range of compositions involving organic (MA^+, FA^+, DMA^+, and G^+) or inorganic (Cs^+, Rb^+, and K^+) monovalent cations.[192,193,215,217,222,250,252] For instance, Kubicki et al. showed that K^+ and Rb^+ ions do not substitutionally dope the lattice of 3D LHPs, as can be seen in the absence of a continuously shifting signal with gradual compositional change (Figure 4c). The results rather point to the formation of new, structurally unidentified phases.[192,193] The situation is different for the G-cation, which at low concentrations occupies the A-site positions.[215] Noticeably, ^2H NMR indicated that the reorientation of G^+ in 3D structures is accelerated compared with the dynamics in a nonperovskite 1D $GPbI_3$ (Figure 4b). The ^2H quadrupole splitting of deuterated G^+ reflects the reorientational dynamics of this cation within the structure. The broader splitting in nonperovskite $G(d_6)PbI_3$ indicates that the dynamics is restricted to rotations along the C−N axes, whereas isotropic reorientations on top of a fast C−N axial rotation are required to explain the narrow lines observed for $G(d_6)_{0.25}MA_{0.75}PbI_3$ perovskite materials. Kubicki et al. suggested that the reorientations of G-cations, which are faster than 10^6 s^{-1}, could explain the improved performance of this material in solar cells,[215,229] in a similar way as the fast MA reorientation prolongs charge-carrier lifetimes in $MAPbI_3$.[244] Grottel et al. have used ^1H NMR relaxation as a probe for the G-cation dynamics and activation energies of the latter as well as phase transitions in 1D $GPbI_3$ and 2D G_2PbI_4 structures.[253]

NMR spectroscopy is also increasingly instrumental for characterizing and elucidating the role of organic cations in 2D perovskites.[130,253−257] For instance, the distinction between different molecules is straightforward, and their locations within slabs or interstitials can be clearly determined.[130,253−255] Milić et al. could distinguish the FA cations in the slabs of 2D $A_2FA_{n-1}Pb_nI_{3n+1}$ (A: (adamantan-1-yl)methanammonium spacers) from those incorporated into a concomitant 3D $FAPbI_3$ using 2D $^1H-^1H$ spin-diffusion NMR spectra (Figure 5a).[130] The dynamics of organic cations extracted from ^1H relaxation times in different 2D LHP structures made it possible to draw conclusions about the crystal rigidity and, in turn, relate the softness of the lattice to the PL line width (exciton−phonon coupling) and other PL characteristics.[257]

The known NMR studies on inorganic A-cations are mainly focused on phase transitions in $CsPbX_3$ LHPs and the structural implications (tilting of lead-halide octahedra, symmetry loss/increase, increase in disorder, etc.) arising from temperature variations.[203−205,258−260] In particular, ^{133}Cs spins were found to be valuable probes to study ferroelastic, twinned domain structures in $CsPbCl_3$.[258,260−264]

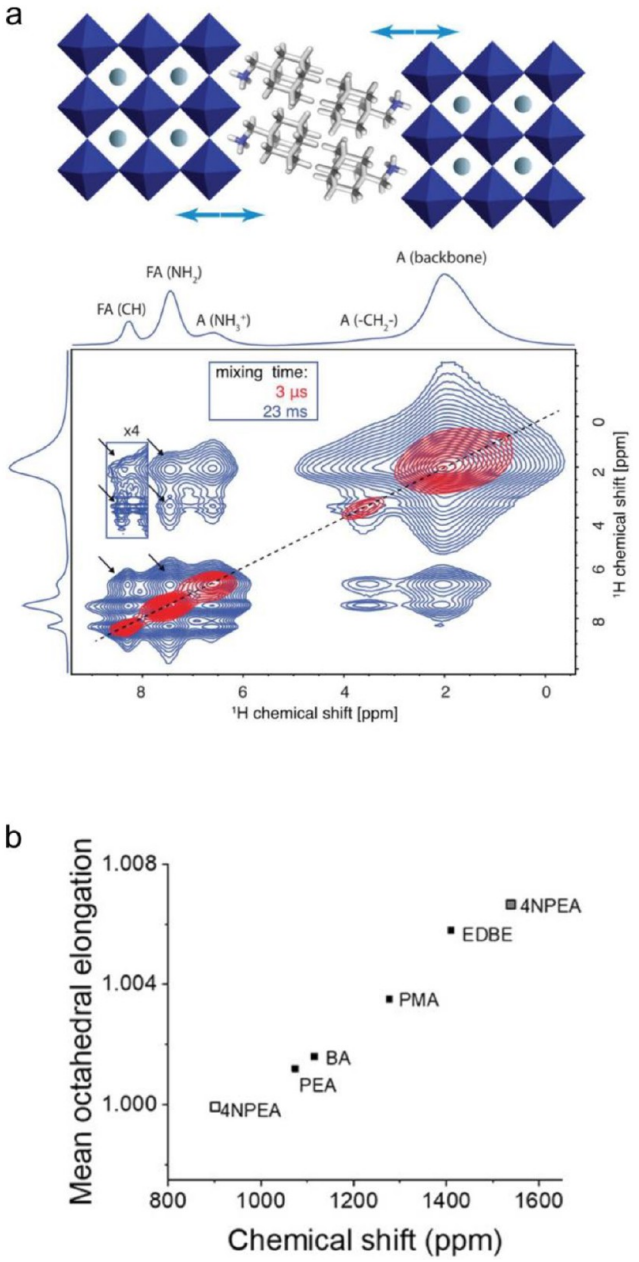

Figure 5. NMR of 2D LHPs. (a) Schematic of a 2D $A_2FA_2Pb_3I_{10}$ structure proposed by Milić et al., corroborated by $^1H-^1H$ spin-diffusion solid-state MAS NMR spectra recorded at different mixing times.[130] The cross peaks highlighted by the arrows in the spectra with longer mixing times indicate the proximity between some FA cations and the spacer cation (adamantan-1-yl)methanammonium (blue arrows in the scheme) and support the proposed structure. Reprinted with permission from ref 130. Copyright 2019 by John Wiley and Sons. (b) Relationship between the mean elongation of lead-halide octahedra in 2D A_2PbI_4 structures with various A cations (4NPEA, 4-nitrophenylethylammonium (two ^{207}Pb NMR signals); PEA, phenylethylammonium; BA, butylammonium; PMA, phenylmethylammonium; EDBE, $NH_3(CH_2)_2O(CH_2)_2O(CH_2)_2NH_3$) and their ^{207}Pb NMR isotropic chemical shifts. Reprinted with permission from ref 255. Copyright 2019 American Chemical Society.

4. ^{207}PB NMR SPECTROSCOPY OF LEAD-HALIDE PEROVSKITES

The large chemical shift range of ^{207}Pb NMR (~20 000 ppm) makes it a highly sensitive probe of major and subtle structural

https://dx.doi.org/10.1021/jacs.0c07338
J. Am. Chem. Soc. 2020, 142, 19413−19437

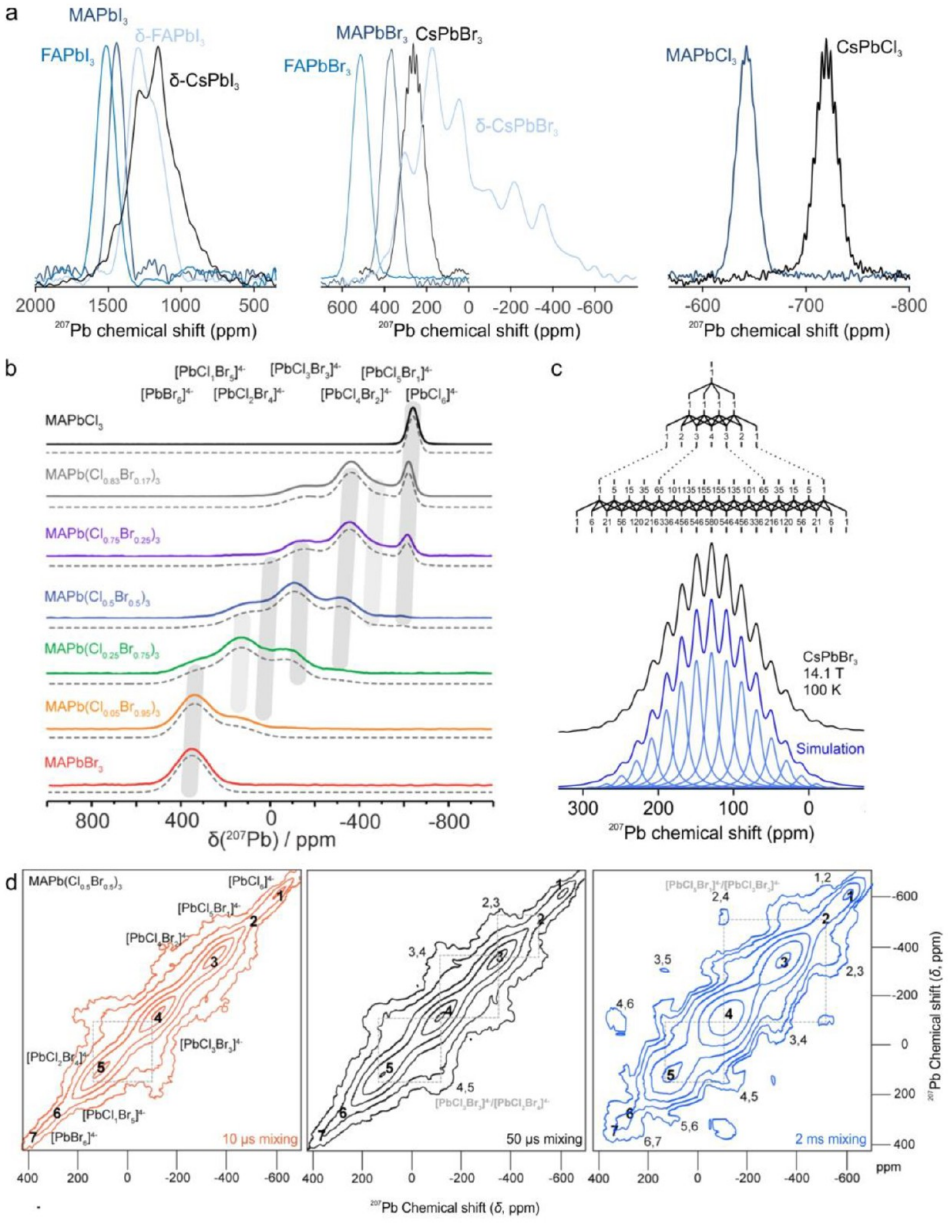

Figure 6. ^{207}Pb NMR of LHPs. (a) ^{207}Pb solid-state NMR spectra of $APbX_3$ compounds. Adapted with permission from ref 273 (Copyright 2020 by Wiley and Sons), ref 270 (Copyright 2019 Springer Nature), and ref 272 (Copyright 2018 American Chemical Society). (b) Gradual change of the halide composition, here from $MAPbCl_3$ to $MAPbBr_3$, results in lead environments with mixed-halide composition $PbX_xX'_{6-x}$ (x = 0−6), whose positions in the spectra correspond almost exactly to the linear interpolation of the pure compounds $APbX_3$ and $APbX'_3$. Reprinted with permission from ref 269. Copyright 2018 American Chemical Society. (c) ^{207}Pb LHP NMR of $CsPbBr_3$ at 100 K. The signal splitting is a 19-fold multiplet generated by the J-coupling to six bromine nuclei. The spikelet conforms with Pascal's triangle. Reprinted with permission from ref 270. Copyright 2019 Springer Nature. (d) $MAPbCl_{1.5}Br_{1.5}$ ^{207}Pb EXSY NMR spectra with increasing exchange times from left to right. The exchange between two of the seven lead environments (1: $[PbCl_6]^{4-}$, 2: $[PbCl_5Br]^{4-}$, 3: $[PbCl_4Br_2]^{4-}$, 4: $[PbCl_3Br_3]^{4-}$, 5: $[PbCl_2Br_4]^{4-}$, 6: $[PbClBr_5]^{4-}$, 7: $[PbBr_6]^{4-}$) produces a cross peak at their frequencies' intersections, indicated by n,m for the exchange between environments n and m. With increasing mixing time, environments not only with one different halide atom (small squares) but also with two changing halides exchange (large squares). Adapted with permission from ref 269. Copyright 2018 American Chemical Society.

changes in the lead surroundings, including first, second, or third coordination shells. The ^{207}Pb NMR signal of $APbX_3$ compounds is more deshielded for heavier halides: $\delta(APbCl_3) < \delta(APbBr_3) < \delta(APbI_3)$ (Figure 6a).[206,265−270] In the mixed-halide perovskites $APbCl_xBr_{3-x}$ and $APbBr_xI_{3-x}$ (A = MA, FA; x = 0−3), seven distinct lead environments $PbX_xX'_{6-x}$ (x = 0−6) were found with chemical shift spanning the range between two monohalide counterparts (Figure 6b), and the ^{207}Pb NMR chemical shifts evolved linearly with the composition.[266−269]

Any substantial dynamics of halide ions should manifest itself in ^{207}Pb NMR, owing to the imparted changes in Pb−X bonding. 2D exchange spectroscopy (EXSY) captured the constantly changing Pb environment due to the exchange of halide atoms (Figure 6d),[268,269] in agreement with the known high diffusivity of halide ions in these materials.[271] The analysis of ^{207}Pb NMR spectra from mixed-halide LHPs obtained with various synthetic procedures differentiates between solid solutions with different degrees of homogeneity and halide miscibility as well as

https://dx.doi.org/10.1021/jacs.0c07338
J. Am. Chem. Soc. 2020, 142, 19413−19437

crystallinity.[266−269] In the ^{207}Pb NMR spectrum of solution-grown $MAPbI_{1.5}Br_{1.5}$, two phases were observed, assigned as $MAPbIBr_2$ and $MAPbBr_3$ based on their chemical shifts.[267] However, the $MAPbBr_3$ phase was not seen in X-ray diffraction patterns, indicating its low crystallinity or localization as a thin layer around $MAPbIBr_2$ grains.

The influence of the composition of the halide coordination sphere of the lead atom on the lead isotropic chemical shifts (^{207}Pb δ_{iso}) is stronger than the effect of connectivity between lead-halide octahedra or octahedral tilts. This is exemplified in Figure 6a, wherein different $APbX_3$ compounds are grouped by composition.[191,270,272,273,191] Of these, nonperovskite lattices are δ-$CsPbBr_3$ and δ-$CsPbI_3$ (1D chains of edge-sharing octahedra) and δ-$FAPbI_3$ (face-sharing, 1D connectivity as well). A-cation substitution in 3D LHPs results in the ^{207}Pb δ_{iso} trend $CsPbX_3$ < $MAPbX_3$ < $FAPbX_3$ in monohalide series (Figure 6a). Besides the structural effect of A-cations (octahedral tilts), the different magnetic properties of the A-cations (different gyromagnetic ratios, polarizabilities, spin multiplicities, etc.) may also contribute to the observed trend. Different octahedral tilts and hence a change in the symmetry also occur upon temperature-induced phase transitions. For instance, $MAPbI_3$ undergoes a transition from tetragonal to orthorhombic polymorphs upon cooling from 20 to −130 °C, seen as a reduction of ^{207}Pb δ_{iso} from 1450 to ∼1100 ppm[219] and accompanied by the gradual appearance of spinning sidebands (i.e., a chemical shift anisotropy (CSA) tensor) due to reduced structure symmetry. Because of the strong temperature dependence of the ^{207}Pb chemical shifts, Bernard et al. proposed the use of $MAPbCl_3$ as an internal thermometer for solid-state NMR experiments,[274] alternative to the commonly used $Pb(NO_3)_2$ salt.[275] In the ^{207}Pb NMR spectra of $MAPbCl_3$, there is no apparent CSA, unlike $Pb(NO_3)_2$, which facilitates the temperature calibration in static solid-state NMR experiments. Furthermore, the ^{13}C NMR signal from MA could serve as an internal standard.

In general, the line width of ^{207}Pb NMR signals is large, from a few kilohertz up to tens of kilohertz, and arises from several line-broadening effects. These include the CSA, the positional disorder leading to a distribution of isotropic chemical shifts, the dipole−dipole coupling (at least for static spectra), and the dispersion of J-coupling values due to variations of the bond lengths and geometries. For $MAPbCl_3$, $CsPbCl_3$, $MAPbBr_3$, and $CsPbBr_3$, it was shown that the signal width is dominated by the lead-halide J-coupling, which is on the order of ca. 400 Hz ($^1J_{Pb-Cl}$) and 2.3 kHz ($^1J_{Pb-Br}$).[185,252,270] 19-Fold multiplets were detected for these LHPs (only at low temperatures in the case of $MAPbBr_3$) due to the (almost) identical couplings of ^{207}Pb nuclei with the six coordinating halide atoms, which all possess spins of I = 3/2 (Figure 6c). The signal width of other $APbX_3$ compounds is also likely to be defined by the lead-halide J-coupling patterns, but because of the increased inhomogeneous line width and lower structural symmetry, the lines of the pattern cannot be resolved.[270] Although often overseen due to the inhomogeneous broadening of the signal or unsuited signal acquisition or processing, the lead-halide couplings had already been observed more than 20 years ago in the doctoral thesis of Holger Ulman (University Dortmund).[276] A plethora of binary, ternary, and quaternary lead-halide materials were synthesized and characterized, and, for a large number of these compounds, the lead-halide coupling was recorded. ^{207}Pb solid-state NMR can also be used to study decomposition products of $MAPbI_3$ when exposed to humidity or thermal stress[277] or to unravel side reactions. For instance, *in situ* DMA formation was captured as a result of the dimethylformamide (solvent) reaction with MA^+ during the preparation of $MAPbI_3$ thin films.[236]

The lower symmetry and the partially disrupted connectivity of the lead-halide octahedra in 2D LHPs affect the chemical shielding of ^{207}Pb nuclei, leading to shifting of the isotropic value[255,272] and the appearance of spinning sidebands due to an increased CSA, which differ for lead atoms within and at the edges of the slabs.[255,278] Tremblay et al. delineated a linear dependence between the chemical shift and the elongation of the lead-halide octahedra produced by different slab-separating cations (Figure 5b).[255] In 2D LHPs, the quantum confinement alters the energy levels of the conduction band (CB) and valence band (VB), resulting in different band-gap energies, whereas the dielectric effect does not alter the band -gap energy but equally shifts the CB and VB on an absolute energy scale. The isotropic and anisotropic chemical shifts may be highly potent probes of these confinement effects because changes in the electronic structure, affecting both the absolute energy values (isotropic chemical shift) as well as the electronic inhomogeneities (anisotropic chemical shift), impact the local magnetic field of ^{207}Pb nuclei. The changes in the VB and CB energies might be compared with the HOMOs and LUMOs in Ramsey's description of chemical shieldings in molecules,[279] which was already applied to explain the observations in NMR spectra of quantized semiconductor materials (in particular, colloidal NCs and nanoplatelets).[280−283] However, one should expect that for the elucidation of the relationship of confinement effects with the chemical shift in 2D perovskites, computational approaches, considering many-body interactions and spin−orbit couplings, are required.

The broad signal width of $APbX_3$ materials, the modest gyromagnetic ratio (5.58×10^7 rad s^{-1} T^{-1}; about five times smaller than that of a proton), and the low natural abundance (22.1%) of ^{207}Pb make it a relatively unreceptive nucleus. Accordingly, recording conventional ^{207}Pb NMR spectra of LHPs usually requires measurement times of several hours. Hanrahan et al. have therefore investigated and quantitatively compared several experimental procedures, such as magic-angle spinning (MAS), low temperatures, dynamic nuclear polarization (DNP), and proton detection, which improve the signal intensity and reduce the acquisition time of ^{207}Pb NMR spectra to a few minutes.[265] They noted that the low-temperature spectra must be interpreted with care because phase transitions can occur, and the dynamics is influenced by the temperature change. Although their DNP enhancement factors were moderate for $MAPbCl_3$ (15−20) and $MAPbBr_3$ (3 to 4) at the applied magnetic field strength (9.4 T) and negligible for $MAPbI_3$, their results showcased a path to the efficient sampling of both LHP thin films and surface species in LHP NCs, which are morphologies with even lower lead concentrations than microcrystalline powders. Besides the experimentally demanding methods previously mentioned, another practically attractive avenue is the development of benchtop, low-magnetic field ^{207}Pb NMR spectroscopy (with a permanent magnet) for the routine characterization of LHPs, as recently demonstrated for $MAPbCl_3$.[284]

5. HALIDE NMR AND NQR

All heavier halides possess a quadrupole moment because they have spins of I > 1/2 ($^{35/37}$Cl I = 3/2, $^{79/81}$Br I = 3/2, ^{127}I I = 5/2), whereas ^{19}F has I = 1/2. Because fluorine is not a structure-

https://dx.doi.org/10.1021/jacs.0c07338
J. Am. Chem. Soc. 2020, 142, 19413−19437

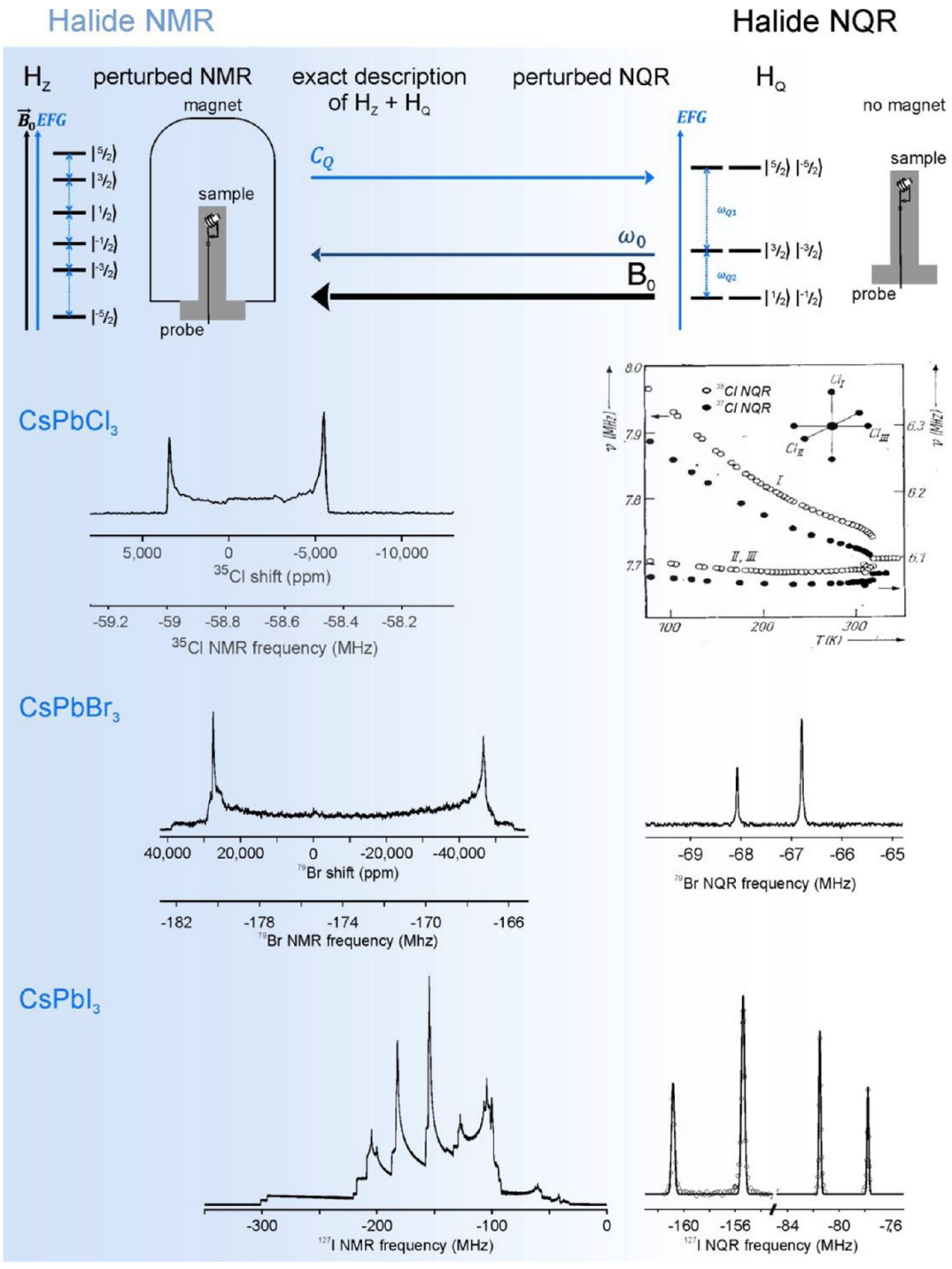

Figure 7. Halide NMR versus NQR, exemplified for $CsPbX_3$. Spins of $I > 1/2$ ($I = 5/2$ depicted example) possess a quadrupole moment, which interacts with the EFG generated by surrounding charges. This quadrupole interaction (H_Q) can, depending on its strength relative to the Zeeman interaction (H_Z), either perturb the NMR transitions (left part of the scheme) or, for strong quadrupole coupling strengths, be the dominant interaction. In the latter case, a perturbed NQR spectrum would be obtained, which would be further simplified by removing the magnetic field, producing a pure NQR spectrum, as shown on the right for $CsPbBr_3$ and $CsPbI_3$. For $CsPbCl_3$, only the resonance frequencies (ν) are shown (at various temperatures, T). Reprinted with permission from ref 190. Copyright 1983 by John Wiley and Sons. For halide quadrupole couplings ($C_Q(^{35}Cl, CsPbCl_3) = 15.5$ MHz, $C_Q(^{79}Br, CsPbBr_3) = 133.6, 136.4$ MHz), which are smaller than the Larmor frequencies ($\omega_0(^{35}Cl) = -58.8$ MHz @ 14.1 T and $\omega_0(^{79}Br) = 175.4$ MHz @ 16.4 T inhere), halide NMR spectra can be recorded, but with involved experimental conditions. Iodine C_Q values in LHPs are larger (ca. 500−600 MHz) than the ^{127}I Larmor frequencies (e.g., 140.1 MHz @ 16.4 T). Hence ^{127}I NMR is complex and too broad for practical acquisition. Only a simulation of the $CsPbI_3$ ^{127}I NMR spectrum at 16.4 T can be provided. Adapted with permission from ref 320. Copyright 2020 American Chemical Society.

former for LHPs, we focus on quadrupolar halide nuclei, yet we must note that ^{19}F NMR is highly instrumental to the study of the fluorine-containing organic moieties of LHPs. For instance, Ruiz-Preciado et al. used it, in combination with DFT calculations, to probe halogen bonding at LHP surfaces.[285] The occasional use of ^{19}F NMR to characterize hybrid LHPs can

https://dx.doi.org/10.1021/jacs.0c07338
J. Am. Chem. Soc. 2020, 142, 19413−19437

Table 1. Summary of Reported Halide Quadrupole Parameters Obtained from Monohalide LHP NQR and NMR Spectra

compound	nucleus	NQR lines (MHz)	C_Q (MHz)	η_Q	temperature	source
$CsPbCl_3$	^{35}Cl	7.69−7.97			77−360 K	ref 190
			15.48 (bulk)	0 (bulk)	100−273 K	ref 320
			15.49−15.51 (NCs)	0 (NCs)	100−273 K	ref 320
	^{37}Cl	7.66−7.89			77−360 K	ref 190
$MAPbCl_3$	^{35}Cl	8.128			298 K	ref 196
$CsPbBr_3$	^{79}Br	70.43, 67.155, 38.42, 37.11			77 K	ref 195
		68.068, 66.781, 37.28			300 K	ref 195
			133.59, 136.36	0.006, 0.03	RT	ref 320
	^{81}Br	58.84, 56.14, 32.091, 30.975			77 K	ref 195
		56.87, 55.782, 31.17			300 K	ref 195
$MAPbBr_3$	^{79}Br	70.451			298 K	ref 196
		69.701, 73.819			77.4 K	ref 196
			141.0185	0.0099	RT	ref 320
	^{81}Br	58.842			298 K	ref 196
		58.239, 61.678			77.4 K	ref 196
$FAPbBr_3$	^{79}Br		149.1034	0.0642	RT	ref 320
	^{79}Br	74.6			RT	ref 250
		73.2, 74.4			160 K	ref 250
δ-$CsPbI_3$	^{127}I	56.55, 94.84; 71.07, 126.10	325.4; 428.6	0.397; 0.319	77 K	ref 195
		56.2, 92.3; 70.15, 125.2	317.9; 425.1	0.423; 0.311	300 K	ref 195
		56.1744, 92.9890; 70.0794, 124.9071	319.7; 424.3	0.415; 0.311	RT	ref 320
γ-$CsPbI_3$	^{127}I		517.98; 537.36.7	0.025; 0.101	RT	ref 320
$MAPbI_3$	^{127}I	83.430, 166.840; 82.062, 164.094	556.139; 573.063	0.010; 0.012	298 K	ref 196
		85.973, 160.192; 84.895, 159.161	539.974; 536.132	0.241; 0.229	77.4 K	ref 196
		82.057, 164.002; 83.449, 167.002	−528.1; −558.6	0.29; 0.34	298 K	ref 194
		83.430, 166.846; 82.073, 164.114	556.16; 547.06	0.00; 0.01	297.3 K	ref 197
		82.13, 164.28	547.59	0.00	350.8 K	ref 197
α-$FAPbI_3$	^{127}I	87.294, 174.59; 85.205, 170.34	581.96; 567.84	0.00; 0.018	189.5 K	ref 197
		86.61, 173.22	577.40	0.00	292.7 K	ref 197
δ-$FAPbI_3$	^{127}I	57.315, 87.935	306.50	0.508	300.0 K	ref 197

also be found in refs 286 and 287. We also note that ^{19}F solid-state NMR has been applied to numerous metal fluoride perovskites (ABF_3)[288−307] and 2D fluoride perovskites,[308] where A = Li, Na, K, Cs, Rb, and ammonium (NH_4^+) and B = Mg, Ca, Ba, Sr, Mn, Co, Zn, and Ho, to study diverse materials aspects, such as fluoride ion mobility[309] or the material's paramagnetism.[299,305]

Quadrupolar halide nuclei are subject not only to the Zeeman interaction (H_Z, Figures 2 and 7) but also to the quadrupole interaction (H_Q) as their quadrupole moment couples to the EFG. The symmetry and the strength of the quadrupole interaction are described by, respectively, the asymmetry (η_Q) and the quadrupole coupling constant (C_Q). The latter scales with the quadrupole moment of the nuclear spin. Together, C_Q and η_Q parametrize the EFG, which contains structural, geometrical, and topological information about the nuclei's surroundings, as they all reflect the charge distribution around the nuclear spin. With the continued advancements of higher magnetic fields, recently extending beyond 1 GHz for commercial devices, halide NMR spectroscopy of LHPs has a fruitful road ahead. For halide NMR to be feasible, the Zeeman interaction, which lifts the degeneracy of nuclear spin energies, must be at least of equal size as the quadrupole interaction. However, C_Q constants reported for LHP are all quite large. Table 1 is a survey of known halide NQR and NMR signals of $APbX_3$. The combination of the large quadrupole moments of the halide spins (Table 2) and the exceptionally large EFGs in LHPs leads to some of the largest C_Q values reported for halide nuclei.[310−312] Magnetic field strengths required to produce Larmor frequencies, ω_0, that are comparable to or larger in size than halide C_Q values in LHPs are at the limits of commercial spectrometers in the case of Cl and Br nuclei and are inaccessible for I nuclei. Therefore, NQR has been a method of choice for studying halide nuclear spin transitions (Figure 7). NQR is a zero-to-low-field sibling of NMR spectroscopy. In NQR, the EFG leads to the splitting of spin energy states, whose energy can be perturbed by a weak magnetic field, similarly to how NMR transitions are perturbed by the quadrupole interaction. A continuous transition from NQR to NMR is obtained with decreasing quadrupole coupling and by increasing the magnetic field strength (Figure 7). Theoretically, all of the material's structure and dynamics aspects contained in the quadrupole interaction are equally accessible through NQR or NMR

Table 2. NMR Properties of Quadrupolar Halide Nuclei

nucleus	spin[321]	natural abundance (%)[321]	gyromagnetic ratio γ (10^6 rad s^{-1} T^{-1})[321]	quadrupole moment Q ($e{\cdot}fm^{-2}$)[a 321]
^{35}Cl	3/2	75.76	26.241991	−8.165
^{37}Cl	3/2	24.24	21.843688	−6.435
^{79}Br	3/2	50.69	67.25619	30.5
^{81}Br	3/2	49.31	72.49779	25.4
^{127}I	5/2	100	53.8957	−71

[a] e stands for the elementary charge 1.602·× 10^{-19} C, with which the tabulated value Q must be multiplied to obtain the quadrupole moment in C/fm^2.

https://dx.doi.org/10.1021/jacs.0c07338
J. Am. Chem. Soc. 2020, 142, 19413−19437

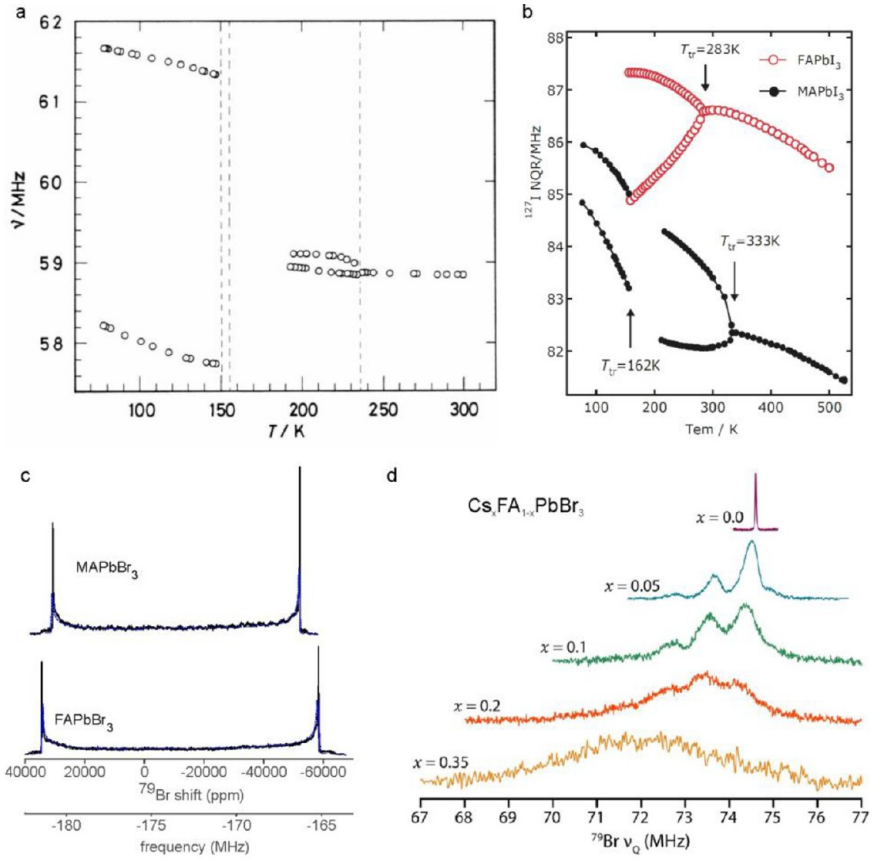

Figure 8. Halide NMR of organic−inorganic LHPs. (a) ^{81}Br NQR frequencies of $MAPbBr_3$ recorded at various temperatures, evidencing the continuous structural changes and sharp phase transitions (dashed lines). Between 150 and 180 K, the signals were too weak to be detected. Reprinted with permission from ref 196. Copyright 1991 De Gruyter. (b) Temperature dependence of low-frequency ^{127}I NQR transitions of $MAPbI_3$ and $FAPbI_3$. Phase transitions are indicated by arrows. Upon cooling from the cubic (>333 K for $MAPbI_3$ and >283 K for $FAPbI_3$) to tetragonal crystal structure, the single ^{127}I NQR signal splits into two signals with an intensity ratio of 2:1, corresponding to the unequal equatorial and axial iodine atoms. Reprinted with permission from ref 197. Copyright 2018 Chemical Society of Japan. (c) High magnetic field strengths (here 16.4 T) make the acquisition of bromine NMR spectra of LHP possible. ^{79}Br NMR spectra of $MAPbBr_3$ and $FAPbBr_3$ are displayed, exhibiting the perfect axial symmetry of the bromine sites. Adapted with permission from ref 320. Copyright 2020 American Chemical Society. (d) ^{79}Br NQR spectra of $Cs_xFA_{1-x}PbBr_3$ (x = 0.0 to 0.35). The three signals observed at low Cs concentrations were attributed to Br with zero, one, and two Cs atoms as nearest neighbors. Adapted with permission from ref 250. Copyright 2020 American Chemical Society.

because the quadrupole parameters can be extracted either from the frequency of the NQR lines[313−317] or from the width and the shape of NMR signals.[318,319] Both kinds of nuclear resonance can be recorded on the same material; see, for instance, the chlorine and bromine NMR and NQR spectra of $CsPbCl_3$ and $CsPbBr_3$ in Figure 7. However, for very large quadrupole couplings, as in iodine-based LHPs, the presently available magnetic field strengths are low compared with the large C_Q, and the acquisition of the complex and broad ^{127}I NMR spectra (see the simulated spectrum in Figure 7) is impractical, whereas narrow-line ^{127}I NQR spectra can be rapidly recorded (Figure 7). Finding the resonance frequency of the signal is far more difficult in NQR than in NMR, as a frequency range from a few hertz up to several hundreds of megahertz must be screened because the NQR resonances scale with the quadrupole coupling.

Unsurprisingly, halide NQR transitions in LHPs were investigated long before chloride and bromide NMR spectra, which were reported only recently.[320] We have not found ^{127}I NMR spectra attributable to LHPs in the literature and have not succeeded in obtaining them ourselves. The first halide NQR of $CsPbX_3$ studies dates to the late 1960s and early 1970s,[195,322,323] a decade after Møller reported the determination of a perovskite lattice for $CsPbX_3$.[324,325] ^{35}Cl NQR was used to explore the phase transitions and structural properties of $CsPbCl_3$.[190,322,323,326] Possible crystal systems could be deduced from the number of NQR lines, their resonance frequencies, and their relaxation behavior. Furthermore, phase transitions and their order could be monitored and explained by the appearance of phonon vibrations. Some controversy existed about the temperatures of the phase transitions,[327] possibly due to the various degrees of twinning in the $CsPbCl_3$ structure[258,259,261,262] and the influence of the thermal history of the sample on the spectroscopic results.[323,326] Although fewer in number, similar $^{79/81}$Br NQR studies on $CsPbBr_3$ were conducted in the past.[195,205]

After Weber reported the synthesis of $MAPbX_3$ in 1978,[328] the phase transitions in these materials were investigated using ^{35}Cl, $^{79/81}$Br, and ^{127}I NQR.[196] Upon cooling, the signal from the single halide species in the cubic phase splits into two signals, corresponding to the inequivalent axial and equatorial halides of lead-halide octahedra in tetragonal and orthorhombic structures; see the ^{81}Br NQR data of $MAPbBr_3$ in Figure 8a. The advent of efficient perovskite photovoltaics also fueled the interest in $MAPbI_3$ from the perspective of nuclear resonance studies. The recently reported ^{127}I NQR spectra of

https://dx.doi.org/10.1021/jacs.0c07338
J. Am. Chem. Soc. 2020, 142, 19413−19437

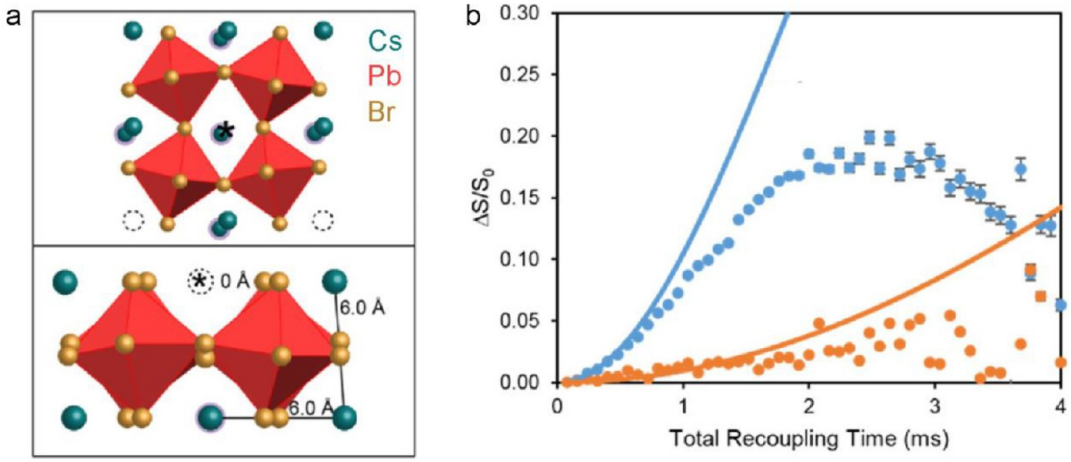

Figure 9. NMR of the NC surface. (a) Structural models of the orthorhombic (010) $CsPbBr_3$ surface. The position of an ammonium proton is indicated by an asterisk. Its simulated $^1H\{^{133}Cs\}/^1H\{^{207}Pb\}$ multispin RESPDOR/S-REDOR curves in panel b (blue/orange lines) match the best experimental data of oleylamine- and oleic-acid-terminated $CsPbBr_3$ NCs. The curves correspond to the evolution of the ^1H signal intensity, $\Delta S/S_0 = (S - S_0)/S_0$, where S is the signal at a given recoupling time and S_0 is the initial signal intensity over the exposure time (total recoupling time) of the ^1H spins to the dipolar coupling with $^{133}Cs/^{207}Pb$ nuclei, respectively. Adapted with permission from ref 337. Copyright 2020 American Chemical Society.

$MAPbI_3$[194,197,219] correlated the line width to the powder quality[219] as well as to the short-range dynamics (e.g., rotational/vibrational motion) of the iodine.[194] The reported ^{127}I quadrupole parameters of $MAPbI_3$ vary in publications, but the NQR resonance frequencies are comparable (Table 1). Discrepancies could originate from slightly different experimental temperatures (Figure 8b), diverse synthetic procedures, and different approaches to determining C_Q and η_Q.

Meanwhile, NQR spectra of other iodine-based LHPs are rare. Yamada et al. found the ^{127}I NQR lines for two polymorphs of $FAPbI_3$ (cubic 3D and nonperovskite 1D phases). They also observed a phase transition from the cubic to tetragonal perovskite lattice at 283 K,[197] seen as the splitting of the single ^{127}I NQR line (only the low-frequency one is shown in Figure 8b) of the cubic phase into two lines corresponding to the inequivalent iodine atoms in the tetragonal phase. A similar study by Volkov et al. reported the ^{127}I NQR transitions and the corresponding quadrupole parameters of yellow nonperovskite δ-$CsPbI_3$ at 77 and 300 K.[195] Our group reproduced these findings recently and completed them with ^{127}I NQR spectra of γ-$CsPbI_3$ (Figure 7).[320]

The ^{35}Cl NMR spectrum of $CsPbCl_3$ and the ^{79}Br NMR spectra of $CsPbBr_3$, $MAPbBr_3$, and $FAPbBr_3$ are shown in Figures 7 and 8c. The large signal width requires the acquisition of multiple subspectra under static conditions with broadband excitation combined with the echo-train collection, as conventional signal averaging (e.g., MAS) brings no improvement. The acquisition of ^{127}I NMR spectra is impractical, as can be seen from the simulated ^{127}I NMR spectrum of orthorhombic γ-$CsPbI_3$ at 16.4 T in Figure 7. The spectrum is >300 MHz broad and exhibits a complex shape, whose spectral features are not trivial to interpret.

Very recently, the impact of Cs incorporation on the inorganic lattice of $FAPbBr_3$ was probed with ^{79}Br NQR, showing signal broadening with increasing Cs content. For low Cs concentrations (up to 10%), the signal splits into three lines, which the authors assigned to Br with zero, one, and two Cs atoms as nearest neighbors (Figure 8d).[250]

6. LEAD-HALIDE PEROVSKITE COLLOIDAL NANOCRYSTALS AND THIN FILMS

LHP NCs are the latest generation of colloidal inorganic semiconductors.[69,329] Colloidal NCs comprise a crystalline core of typically 3−20 nm in diameter. When the NC size is comparable to or smaller than the Bohr diameter of a photogenerated electron−hole pair (exciton), the NC's electronic structure is altered; in particular, the band-gap energy increases with decreasing NC size (quantum-size effect).[40,330] There exists an interface between the inorganic crystalline core and the long-hydrocarbon-chain capping ligands anchored to the surface via a suitable binding group. These ligands ensure the structural integrity of NCs and impart colloidal stability in apolar solvents. The surface state is also of paramount importance for the optical and electronic characteristics of semiconductor NCs.[331] Understanding and characterizing the NC surfaces has always been nontrivial. NMR spectroscopy is a rare analytical method that is (nearly) fully forgiving yet is highly sensitive to the degree and disruption of atomic order at the surface. For the investigation of the organic−inorganic interface, it is most desired to study the colloidal NCs in their native colloidal state. Ligands' binding motifs and binding dynamics can be deduced from the line width and position of signals in 1D NMR spectra as well as from the information about internuclear distances and mobility from 2D NMR experiments (nuclear Overhauser effect spectroscopy (NOESY), diffusion ordered spectroscopy (DOSY), etc.). This suite of solution-state NMR methods for characterizing ligand shells has been well established for conventional colloidal semiconductor NCs[332,333] and recently extended to LHP NCs.[334−336] Also, solid-state NMR was used to probe the inorganic surface termination of $CsPbBr_3$ NCs.[337] In ref 337, the distance dependence of the dipolar coupling (Figure 2) was utilized to probe the outmost Cs and Pb atoms by performing $^1H\{^{133}Cs\}$ RESPDOR (resonance-echo saturation-pulse double-resonance)and $^1H\{^{207}Pb\}$ S-REDOR (symmetry-based resonance-echo double-resonance) experiments. These experiments probed the distance between the ammonium protons of the oleylammonium ligands and the closest ^{133}Cs and ^{207}Pb nuclei. The dipolar coupling leads to a decrease in the intensity of the oleylammonium proton signal with increasing

https://dx.doi.org/10.1021/jacs.0c07338
J. Am. Chem. Soc. 2020, 142, 19413−19437

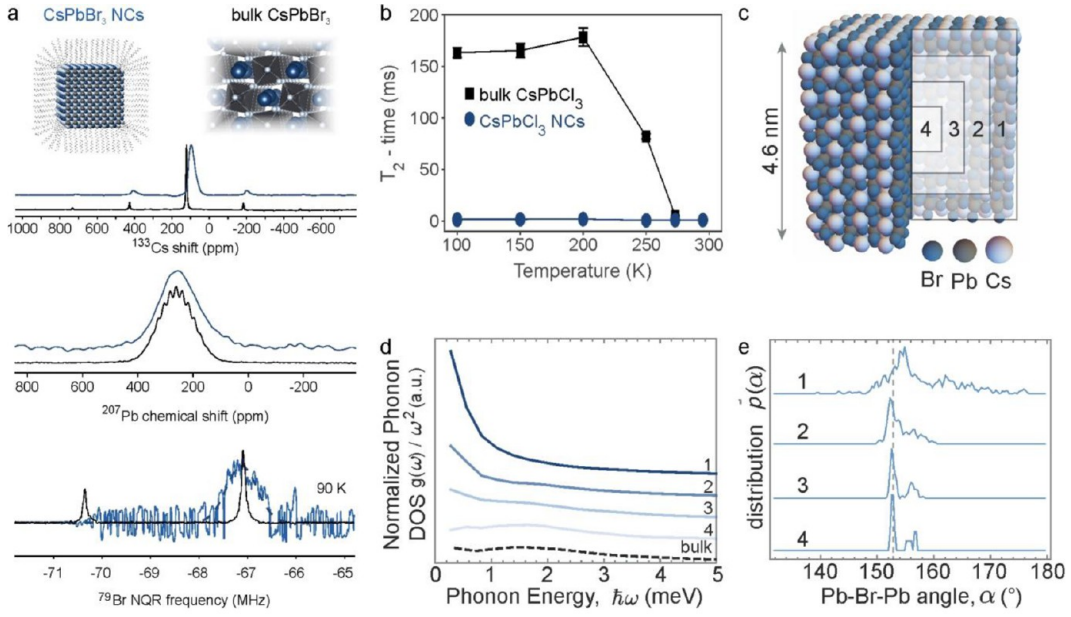

Figure 10. Structure disorder and dynamics in LHP NCs. (a) Both in bulk (black) and in NCs (blue), all atoms are accessible with magnetic resonance, as exemplified by $CsPbBr_3$ (A-cation: ^{133}Cs NMR spectra, unpublished; Pb(II) cation;[270] halides: ^{79}Br NQR spectra at 90 K).[320] (b) Temperature-dependent ^{35}Cl NMR T_2 relaxation times of bulk and nanocrystalline $CsPbCl_3$. (c) Regions 1−4 within a $CsPbBr_3$ NCs. (d) Plot of the partial phonon density of states in each of the four NC regions, normalized to the phonon frequency squared to accentuate the low-energy region. (e) Plots of the statistical distribution of Pb−Cl−Pb angles, α, within each NC region. Adapted from ref 270 (Copyright 2020 Springer Nature) and ref 320 (Copyright 2020 American Chemical Society).

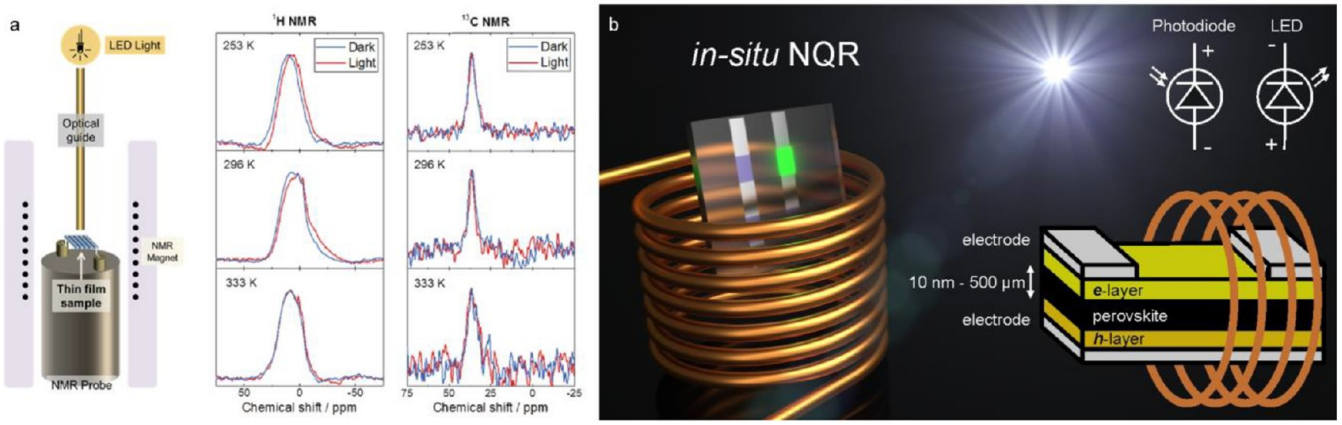

Figure 11. Magnetic resonance of LHP thin films and devices. (a) *In situ* NMR setup and ^{1}H and ^{13}C NMR *in situ* spectra of a ^{13}C-enriched $MAPbI_3$ thin film at various temperatures under irradiation (light) and under identical conditions in the dark. Adapted with permission from ref 223. Copyright 2018 American Chemical Society. (b) We outline NQR as a highly suitable method for acquiring spectra from LHP optoelectronic devices, including *in situ* and *in operando* measurements. "e-layer" and "h-layer" denote electron- and hole-conducting or injecting layer(s), respectively. The device structure may employ electron- and hole-blocking layers. Electrodes are commonly metallic or transparent conductive oxides of a suitable workfunction for injecting electrons and holes. Credit: Yevhen Shynkarenko.

duration of the total recoupling time (the time during which the dipolar coupling is reintroduced). Strong couplings lead to a fast decrease in the signal intensity, and hence the behavior of the signal intensity over different recoupling times contains information about the number of, and the distance to, neighboring heteronuclei. The experimental initial rates were compared with the simulated curves obtained for four possible surface terminations. From this comparison, it was concluded that the studied $CsPbBr_3$ NCs exhibit Cs termination, and some of the surface Cs ions are replaced by oleylammonium ligands (Figure 9). In general, both the surface and the inorganic core of LHP NCs are addressable by NMR methods. The ^{207}Pb NMR spectra of $MAPbX_3$ NCs[265,266] and $CsPbBr_3$ NCs[270,337] exhibit rather featureless signals at similar chemical shifts as their bulk counterparts (Figure 10a) but with much greater signal line width due to chemical and electronic disorder (inhomogeneous broadening). The ^{35}Cl NMR spectra of $CsPbCl_3$ NCs and the ^{79}Br and ^{127}I NQR lines of $CsPbBr_3$ and $CsPbI_3$ NCs are also closely matching those of the bulk counterparts in terms of the resonance frequencies and the spectral shape.[320] However, the ^{79}Br NQR lines of $CsPbBr_3$ NCs are six times broader than those of the bulk due to inhomogeneous contributions. These NCs' ^{79}Br NQR signals are also much less intense, such that the higher frequency line could not be detected (Figure 10a). A characteristic difference between the bulk and the NCs is the accelerated spin−spin relaxation (T_2) of halide nuclei in NCs.[320]

https://dx.doi.org/10.1021/jacs.0c07338
J. Am. Chem. Soc. 2020, 142, 19413−19437

For instance, ^{35}Cl NMR signals relax faster in $CsPbCl_3$ NCs than in the bulk (Figure 10b), and the discrepancy between the T_1 and T_2 relaxation behaviors in the two sample morphologies is a strong indication of the accelerated structure dynamics in NCs, which was corroborated by AIMD calculations. These simulations indicated that surface and near-surface regions in NCs exhibit a much higher density of low-frequency phonon states (Figure 10c,d) and a larger distribution of lead-halide bond angles (Figure 10e). An alternative or complementary explanation to this anharmonic dynamics driven by low-energy modes could be the existence of a new pathway for ionic motion, for example, surface ionic mobility with extremely low activation energies, which could also account for the observed disparity in the T_2 behavior between NCs and bulk LHPs. A further computational analysis involving AIMD and DFT calculations would be needed to explore this and other structural hypotheses. We expect that embarking on the combination of magnetic resonance methods and increasingly powerful atomistic computational tools for materials is a strategy that will be indispensable for rationalizing the observed T_1 and T_2 behaviors in diverse solid-state materials.

Thin films of LHPs find use in LEDs (thicknesses down to few nanometers),[14] photodetectors, and solar cells (hundreds of nanometers)[5,6] as well as in lasers.[17,338,339] Thicker films of up to and above 50 μm are required in X-ray and gamma detectors.[29] These films may greatly vary in their crystallinity[41,340] Furthermore, such films can be fully planar or may conformally coat diverse objects and shapes, such as in the case of LHP-coated microbeads for lasing.[341] Arguably, it is most desired to characterize such forms of LHPs intact, without, for instance, scraping the material of the film into a powder. Any such sample preparation is invasive by nature, especially for such soft materials as LHPs. There exist scarce examples of NMR measurements on thin films of LHPs.[192,215,342] Senocrate et al. have investigated the effect of light absorption on $MAPbI_3$ thin films by illuminating them *in situ* during the acquisition of NMR signals from MA cations (Figure 11a). They found no apparent difference between dark and illuminated samples, which corroborates the absence of the anticipated translational motion of MA cations.[223] As discussed previously, the detection of ^{207}Pb NMR LHP signals is time-demanding, and small sample quantities exacerbate the sensitivity issue. The sensitivity-enhancement experiments, however, have showcased the feasibility of the direct acquisition of the ^{207}Pb NMR signal in thin films.[265] As for halide nuclei, there have been no reports on NMR (or NQR) nuclear halide signals from LHP thin films. To this end, we would like to emphasize the practical feasibility of halide NQR studies of LHP thin films due to the high sensitivity of $^{79/81}$Br and ^{127}I NQR. As an illustration, extrapolating from the ^{127}I NQR of the α-$FAPbI_3$ bulk signal, a thin film with a thickness of 10 nm and an area of 1 cm^2 (ca. 4 μg) should yield a detectable signal within several minutes (ca. 10 min for S/N > 3). The experimental simplicity and the low costs of the NQR setup as well as its noninvasive nature predispose the NQR for the direct probing of LHPs incorporated within the devices, possibly even *in situ* during device operation or upon external stimuli (Figure 11b). Most electron- or hole-conducting, metallic, or other layers will not affect the NQR experiment, and integrating simultaneous irradiation or optical spectroscopy is easier to implement compared with NMR spectroscopy. Such direct application of the NQR of devices eliminates the sample-altering manipulations for the removal of perovskite layers from the devices

7. CONCLUDING REMARKS

LHPs and other metal halides comprise chemical elements, most of which are easily accessible with magnetic resonance methods, and element specificity reduces the interference from other materials present in the sample. Magnetic resonance methods are applicable to crystalline and amorphous materials, including large single crystals, NCs, thin films, and so on. NMR and NQR probe both static and dynamic structural disorder, peculiarities of chemical bonding, and electronic effects. Highly porous materials, surfaces, and interfaces can be discriminatively probed with suitable adaptations of the methods. On top of reduced/disrupted crystallinity, as in LHP NCs and polycrystalline thin films, anomalous distributions and gradients of elements may emerge as well. NC surfaces and surface-bound ligands are structurally distinct regions, too. These effects are all within the reach of NMR and NQR techniques.

The strong quadrupole interaction imparts further potential to probe the material's structure with accuracies comparable to those of synchrotron X-ray diffraction. For instance, the expansion of the crystal unit cell of $CsPbBr_3$ by just 0.001 Å produces, according to DFT calculations, a change of tens of kilohertz in the ^{79}Br C_Q.[320] The effect on the ^{127}I C_Q values will be even more extreme due to the larger quadrupole moment of iodine nuclei (Table 2).

NQR spectra, while containing similar information on the structure and dynamics, can be easier to acquire for nuclei with stronger quadrupole coupling, such as those of halides. NQR also has a very useful practical twist—it does not require high-field magnets. Hence NQR can be more easily adapted for *in situ* and *in operando* studies. It does not require special sample preparation or separation from other components (e.g., conducting or protective layers). For instance, ^{14}N and ^{35}Cl NQR are commonplace for drug, landmine, and explosive detection[343] as well as for chemical quality and quantity control in the pharmaceutical industry.[344−346] In both cases, opening of containers or moving of the sample is either not desired or not possible (too heavy, consecutive degradation, explosion, destruction, etc.), a problem that is also faced with thin-film LHP devices. Hence, NQR spectroscopy has the potential to become a highly sensitive fingerprint quality-control tool for LHP devices or may give unique insight into the LHP material structure in relation to the operation conditions or the device fabrication methods.

AUTHOR INFORMATION

Corresponding Author

Maksym V. Kovalenko − *Department of Chemistry and Applied Biosciences, ETH Zürich, Zurich CH-8093, Switzerland; Empa-Swiss Federal Laboratories for Materials Science and Technology, Dübendorf CH-8600, Switzerland;* orcid.org/0000-0002-6396-8938; Email: mvkovalenko@ethz.ch

Authors

Laura Piveteau − *Department of Chemistry and Applied Biosciences, ETH Zürich, Zurich CH-8093, Switzerland; Empa-Swiss Federal Laboratories for Materials Science and Technology, Dübendorf CH-8600, Switzerland; CNRS, UPR 3079, CEMHTI, Orléans 45071 Cedex 02, France;* orcid.org/0000-0001-6275-5116

Viktoriia Morad − *Department of Chemistry and Applied Biosciences, ETH Zürich, Zurich CH-8093, Switzerland; Empa-Swiss Federal Laboratories for Materials Science and Technology, Dübendorf CH-8600, Switzerland*

https://dx.doi.org/10.1021/jacs.0c07338
J. Am. Chem. Soc. 2020, 142, 19413−19437

Complete contact information is available at:
https://pubs.acs.org/10.1021/jacs.0c07338

Author Contributions

L.P., V.M., and M.K. prepared the manuscript.

Notes

The authors declare no competing financial interest.

■ ACKNOWLEDGMENTS

M.K. acknowledges financial support from the European Union through the FP7 (ERC Starting Grant NANOSOLID, grant agreement no. [306733]) and through Horizon 2020 (ERC Consolidator Grant SCALE-HALO grant agreement no. [819740]). L.P. acknowledges financial support from the Scholarship Fund of the Swiss Chemical Industry (SSCI Award 2015) and from the Swiss National Science Foundation (Early Postdoc Mobility scholarship, P2EYP2_188002). Marcel Aebli is acknowledged for fruitful discussions. Kyle McCall is acknowledged for reading the manuscript.

■ REFERENCES

(1) Pazos-Outón, L. M.; Szumilo, M.; Lamboll, R.; Richter, J. M.; Crespo-Quesada, M.; Abdi-Jalebi, M.; Beeson, H. J.; Vrućinić, M.; Alsari, M.; Snaith, H. J.; Ehrler, B.; Friend, R. H.; Deschler, F. Photon recycling in lead iodide perovskite solar cells. *Science* **2016**, *351* (6280), 1430−1433.

(2) Xing, G.; Mathews, N.; Sun, S.; Lim, S. S.; Lam, Y. M.; Grätzel, M.; Mhaisalkar, S.; Sum, T. C. Long-Range Balanced Electron- and Hole-Transport Lengths in Organic-Inorganic $CH_3NH_3PbI_3$. *Science* **2013**, *342* (6156), 344.

(3) Shi, D.; Adinolfi, V.; Comin, R.; Yuan, M.; Alarousu, E.; Buin, A.; Chen, Y.; Hoogland, S.; Rothenberger, A.; Katsiev, K.; Losovyj, Y.; Zhang, X.; Dowben, P. A.; Mohammed, O. F.; Sargent, E. H.; Bakr, O. M. Low trap-state density and long carrier diffusion in organolead trihalide perovskite single crystals. *Science* **2015**, *347* (6221), 519−522.

(4) Kovalenko, M. V.; Protesescu, L.; Bodnarchuk, M. I. Properties and Potential Optoelectronic Applications of Lead Halide Perovskite Nanocrystals. *Science* **2017**, *358* (6364), 745−750.

(5) Kim, H.-S.; Lee, C.-R.; Im, J.-H.; Lee, K.-B.; Moehl, T.; Marchioro, A.; Moon, S.-J.; Humphry-Baker, R.; Yum, J.-H.; Moser, J. E.; Grätzel, M.; Park, N.-G. Lead iodide perovskite sensitized all-solid-state submicron thin film mesoscopic solar cell with efficiency exceeding 9%. *Sci. Rep.* **2012**, *2* (1), 591.

(6) Lee, M. M.; Teuscher, J.; Miyasaka, T.; Murakami, T. N.; Snaith, H. J. Efficient Hybrid Solar Cells Based on Meso-Superstructured Organometal Halide Perovskites. *Science* **2012**, *338* (6107), 643−647.

(7) Kojima, A.; Teshima, K.; Shirai, Y.; Miyasaka, T. Organometal Halide Perovskites as Visible-Light Sensitizers for Photovoltaic Cells. *J. Am. Chem. Soc.* **2009**, *131* (17), 6050−6051.

(8) Saliba, M.; Matsui, T.; Seo, J.-Y.; Domanski, K.; Correa-Baena, J.-P.; Nazeeruddin, M. K.; Zakeeruddin, S. M.; Tress, W.; Abate, A.; Hagfeldt, A.; Grätzel, M. Cesium-Containing Triple Cation Perovskite Solar Cells: Improved Stability, Reproducibility and High Efficiency. *Energy Environ. Sci.* **2016**, *9* (6), 1989−1997.

(9) Shi, Z.; Jayatissa, A. H. Perovskites-Based Solar Cells: A Review of Recent Progress, Materials and Processing Methods. *Materials* **2018**, *11* (5), 729.

(10) NREL, Best Research-Cell Efficiencies, 2020. https://www.nrel.gov/pv/assets/pdfs/best-research-cell-efficiencies.20200406.pdf.

(11) Yoon, H. C.; Lee, H.; Kang, H.; Oh, J. H.; Do, Y. R. Highly efficient wide-color-gamut QD-emissive LCD□s using red and green perovskite core/shell QDs. *J. Mater. Chem. C* **2018**, *6* (47), 13023−13033.

(12) Chen, N.; Bai, Z.; Wang, Z.; Ji, H.; Liu, R.; Cao, C.; Wang, H.; Jiang, F.; Zhong, H. P-119: Low Cost Perovskite Quantum Dots Film Based Wide Color Gamut Backlight Unit for LCD TVs. *Dig. Tech. Pap. - Soc. Inf. Disp. Int. Symp.* **2018**, *49* (1), 1657−1659.

(13) He, Z.; Zhang, C.; Dong, Y.; Wu, S.-T. Emerging Perovskite Nanocrystals-Enhanced Solid-State Lighting and Liquid-Crystal Displays. *Crystals* **2019**, *9*, 59.

(14) Wang, Q.; Wang, X.; Yang, Z.; Zhou, N.; Deng, Y.; Zhao, J.; Xiao, X.; Rudd, P.; Moran, A.; Yan, Y.; Huang, J. Efficient sky-blue perovskite light-emitting diodes via photoluminescence enhancement. *Nat. Commun.* **2019**, *10* (1), 5633.

(15) Kumawat, N. K.; Liu, X.-K.; Kabra, D.; Gao, F. Blue perovskite light-emitting diodes: progress, challenges and future directions. *Nanoscale* **2019**, *11* (5), 2109−2120.

(16) Xu, W.; Hu, Q.; Bai, S.; Bao, C.; Miao, Y.; Yuan, Z.; Borzda, T.; Barker, A. J.; Tyukalova, E.; Hu, Z.; Kawecki, M.; Wang, H.; Yan, Z.; Liu, X.; Shi, X.; Uvdal, K.; Fahlman, M.; Zhang, W.; Duchamp, M.; Liu, J.-M.; Petrozza, A.; Wang, J.; Liu, L.-M.; Huang, W.; Gao, F. Rational molecular passivation for high-performance perovskite light-emitting diodes. *Nat. Photonics* **2019**, *13* (6), 418−424.

(17) Jia, Y.; Kerner, R. A.; Grede, A. J.; Rand, B. P.; Giebink, N. C. Continuous-wave lasing in an organic−inorganic lead halide perovskite semiconductor. *Nat. Photonics* **2017**, *11* (12), 784−788.

(18) Xing, G.; Mathews, N.; Lim, S. S.; Yantara, N.; Liu, X.; Sabba, D.; Grätzel, M.; Mhaisalkar, S.; Sum, T. C. Low-Temperature Solution-Processed Wavelength-Tunable Perovskites for Lasing. *Nat. Mater.* **2014**, *13* (5), 476−480.

(19) Zhu, H.; Fu, Y.; Meng, F.; Wu, X.; Gong, Z.; Ding, Q.; Gustafsson, M. V.; Trinh, M. T.; Jin, S.; Zhu, X. Y. Lead Halide Perovskite Nanowire Lasers with Low Lasing Thresholds and High Quality Factors. *Nat. Mater.* **2015**, *14* (6), 636−642.

(20) Yakunin, S.; Protesescu, L.; Krieg, F.; Bodnarchuk, M. I.; Nedelcu, G.; Humer, M.; De Luca, G.; Fiebig, M.; Heiss, W.; Kovalenko, M. V. Low-Threshold Amplified Spontaneous Emission and Lasing from Colloidal Nanocrystals of Caesium Lead Halide Perovskites. *Nat. Commun.* **2015**, *6* (1), 8056.

(21) Dou, L.; Yang, Y.; You, J.; Hong, Z.; Chang, W.-H.; Li, G.; Yang, Y. Solution-Processed Hybrid Perovskite Photodetectors with High Detectivity. *Nat. Commun.* **2014**, *5* (1), 5404.

(22) Zhang, M.; Zhang, F.; Wang, Y.; Zhu, L.; Hu, Y.; Lou, Z.; Hou, Y.; Teng, F. High-Performance Photodiode-Type Photodetectors Based on Polycrystalline Formamidinium Lead Iodide Perovskite Thin Films. *Sci. Rep.* **2018**, *8* (1), 11157.

(23) Saidaminov, M. I.; Adinolfi, V.; Comin, R.; Abdelhady, A. L.; Peng, W.; Dursun, I.; Yuan, M.; Hoogland, S.; Sargent, E. H.; Bakr, O. M. Planar-Integrated Single-Crystalline Perovskite Photodetectors. *Nat. Commun.* **2015**, *6* (1), 8724.

(24) Fang, Y.; Dong, Q.; Shao, Y.; Yuan, Y.; Huang, J. Highly Narrowband Perovskite Single-Crystal Photodetectors Enabled by Surface-Charge Recombination. *Nat. Photonics* **2015**, *9* (10), 679−686.

(25) Wang, X.; Li, M.; Zhang, B.; Wang, H.; Zhao, Y.; Wang, B. Recent Progress in Organometal Halide Perovskite Photodetectors. *Org. Electron.* **2018**, *52*, 172−183.

(26) Ahmadi, M.; Wu, T.; Hu, B. A Review on Organic−Inorganic Halide Perovskite Photodetectors: Device Engineering and Fundamental Physics. *Adv. Mater.* **2017**, *29* (41), 1605242.

(27) Feng, J.; Gong, C.; Gao, H.; Wen, W.; Gong, Y.; Jiang, X.; Zhang, B.; Wu, Y.; Wu, Y.; Fu, H.; Jiang, L.; Zhang, X. Single-Crystalline Layered Metal-Halide Perovskite Nanowires for Ultrasensitive Photodetectors. *Nat. Electron.* **2018**, *1* (7), 404−410.

(28) García de Arquer, F. P.; Armin, A.; Meredith, P.; Sargent, E. H. Solution-processed semiconductors for next-generation photodetectors. *Nat. Rev. Mater.* **2017**, *2* (3), 16100.

(29) Wei, H.; Huang, J. Halide lead perovskites for ionizing radiation detection. *Nat. Commun.* **2019**, *10* (1), 1066.

(30) Kim, Y. C.; Kim, K. H.; Son, D.-Y.; Jeong, D.-N.; Seo, J.-Y.; Choi, Y. S.; Han, I. T.; Lee, S. Y.; Park, N.-G. Printable Organometallic Perovskite Enables Large-Area, Low-Dose X-ray Imaging. *Nature* **2017**, *550* (7674), 87−91.

(31) He, Y.; Matei, L.; Jung, H. J.; McCall, K. M.; Chen, M.; Stoumpos, C. C.; Liu, Z.; Peters, J. A.; Chung, D. Y.; Wessels, B. W.; Wasielewski, M. R.; Dravid, V. P.; Burger, A.; Kanatzidis, M. G. High

spectral resolution of gamma-rays at room temperature by perovskite $CsPbBr_3$ single crystals. *Nat. Commun.* **2018**, *9* (1), 1609.
(32) Dong, Q.; Fang, Y.; Shao, Y.; Mulligan, P.; Qiu, J.; Cao, L.; Huang, J. Electron-Hole Diffusion Lengths > 175 μm in solution-grown $CH_3NH_3PbI_3$ single crystals. *Science* **2015**, *347* (6225), 967−970.
(33) Yakunin, S.; Dirin, D. N.; Protesescu, L.; Sytnyk, M.; Tollabimazraehno, S.; Humer, M.; Hackl, F.; Fromherz, T.; Bodnarchuk, M. I.; Kovalenko, M. V.; Heiss, W. High Infrared Photoconductivity in Films of Arsenic-Sulfide-Encapsulated Lead-Sulfide Nanocrystals. *ACS Nano* **2014**, *8* (12), 12883−12894.
(34) Wei, H.; DeSantis, D.; Wei, W.; Deng, Y.; Guo, D.; Savenije, T. J.; Cao, L.; Huang, J. Dopant Compensation in Alloyed $CH_3NH_3PbBr_{3-x}Cl_x$ Perovskite Single Crystals for Gamma-Ray Spectroscopy. *Nat. Mater.* **2017**, *16* (8), 826−833.
(35) Yakunin, S.; Dirin, D. N.; Shynkarenko, Y.; Morad, V.; Cherniukh, I.; Nazarenko, O.; Kreil, D.; Nauser, T.; Kovalenko, M. V. Detection of gamma photons using solution-grown single crystals of hybrid lead halide perovskites. *Nat. Photonics* **2016**, *10* (9), 585−589.
(36) Dirin, D. N.; Cherniukh, I.; Yakunin, S.; Shynkarenko, Y.; Kovalenko, M. V. Solution-Grown $CsPbBr_3$ Perovskite Single Crystals for Photon Detection. *Chem. Mater.* **2016**, *28* (23), 8470−8474.
(37) Birowosuto, M. D.; Cortecchia, D.; Drozdowski, W.; Brylew, K.; Lachmanski, W.; Bruno, A.; Soci, C. X-Ray Scintillation in Lead Halide Perovskite Crystals. *Sci. Rep.* **2016**, *6* (1), 37254.
(38) Chen, Q.; Wu, J.; Ou, X.; Huang, B.; Almutlaq, J.; Zhumekenov, A. A.; Guan, X.; Han, S.; Liang, L.; Yi, Z.; Li, J.; Xie, X.; Wang, Y.; Li, Y.; Fan, D.; Teh, D. B. L.; All, A. H.; Mohammed, O. F.; Bakr, O. M.; Wu, T.; Bettinelli, M.; Yang, H.; Huang, W.; Liu, X. All-inorganic perovskite nanocrystal scintillators. *Nature* **2018**, *561* (7721), 88−93.
(39) Utzat, H.; Sun, W.; Kaplan, A. E. K.; Krieg, F.; Ginterseder, M.; Spokoyny, B.; Klein, N. D.; Shulenberger, K. E.; Perkinson, C. F.; Kovalenko, M. V.; Bawendi, M. G. Coherent single-photon emission from colloidal lead halide perovskite quantum dots. *Science* **2019**, *363* (6431), 1068.
(40) Rainò, G.; Becker, M. A.; Bodnarchuk, M. I.; Mahrt, R. F.; Kovalenko, M. V.; Stöferle, T. Superfluorescence from lead halide perovskite quantum dot superlattices. *Nature* **2018**, *563* (7733), 671−675.
(41) Matt, G. J.; Levchuk, I.; Knüttel, J.; Dallmann, J.; Osvet, A.; Sytnyk, M.; Tang, X.; Elia, J.; Hock, R.; Heiss, W.; Brabec, C. J. Sensitive Direct Converting X-Ray Detectors Utilizing Crystalline $CsPbBr_3$ Perovskite Films Fabricated via Scalable Melt Processing. *Adv. Mater. Interfaces* **2020**, *7* (4), 1901575.
(42) Pan, W.; Yang, B.; Niu, G.; Xue, K.-H.; Du, X.; Yin, L.; Zhang, M.; Wu, H.; Miao, X.-S.; Tang, J. Hot-Pressed $CsPbBr_3$ Quasi-Monocrystalline Film for Sensitive Direct X-ray Detection. *Adv. Mater.* **2019**, *31* (44), 1904405.
(43) Zhang, P.; Sun, Q.; Xu, Y.; Li, X.; Liu, L.; Zhang, G.; Tao, X. Enhancing Carrier Transport Properties of Melt-grown $CsPbBr_3$ Single Crystals by Eliminating Inclusions. *Cryst. Growth Des.* **2020**, *20* (4), 2424−2431.
(44) Jiang, J.; Sun, X.; Chen, X.; Wang, B.; Chen, Z.; Hu, Y.; Guo, Y.; Zhang, L.; Ma, Y.; Gao, L.; Zheng, F.; Jin, L.; Chen, M.; Ma, Z.; Zhou, Y.; Padture, N. P.; Beach, K.; Terrones, H.; Shi, Y.; Gall, D.; Lu, T.-M.; Wertz, E.; Feng, J.; Shi, J. Carrier lifetime enhancement in halide perovskite via remote epitaxy. *Nat. Commun.* **2019**, *10* (1), 4145.
(45) Herz, L. M. Charge-Carrier Mobilities in Metal Halide Perovskites: Fundamental Mechanisms and Limits. *ACS Energy Lett.* **2017**, *2* (7), 1539−1548.
(46) Zhang, Z.; Yang, G. Recent advancements in using perovskite single crystals for gamma-ray detection. *J. Mater. Sci.: Mater. Electron.* **2020**, DOI: 10.1007/s10854-020-03519-z.
(47) Akkerman, Q. A.; Rainò, G.; Kovalenko, M. V.; Manna, L. Genesis, Challenges and Opportunities for Colloidal Lead Halide Perovskite Nanocrystals. *Nat. Mater.* **2018**, *17* (5), 394−405.
(48) Huang, H.; Bodnarchuk, M. I.; Kershaw, S. V.; Kovalenko, M. V.; Rogach, A. L. Lead Halide Perovskite Nanocrystals in the Research Spotlight: Stability and Defect Tolerance. *ACS Energy Lett.* **2017**, *2* (9), 2071−2083.
(49) Li, W.; Wang, Z.; Deschler, F.; Gao, S.; Friend, R. H.; Cheetham, A. K. Chemically Diverse and Multifunctional Hybrid Organic−Inorganic Perovskites. *Nat. Rev. Mater.* **2017**, *2* (3), 16099.
(50) Ball, J. M.; Petrozza, A. Defects in Perovskite-Halides and their Effects in Solar Cells. *Nat. Energy* **2016**, *1* (11), 16149.
(51) Wang, F.; Bai, S.; Tress, W.; Hagfeldt, A.; Gao, F. Defects Engineering for High-Performance Perovskite Solar Cells. *npj Flex. Electron.* **2018**, *2* (1), 22.
(52) Huang, J.; Yuan, Y.; Shao, Y.; Yan, Y. Understanding the Physical Properties of Hybrid Perovskites for Photovoltaic Applications. *Nat. Rev. Mater.* **2017**, *2* (7), 17042.
(53) Takahashi, T.; Watanabe, S. Recent progress in CdTe and CdZnTe detectors. *IEEE Trans. Nucl. Sci.* **2001**, *48* (4), 950−959.
(54) Zhang, H.; Wang, F.; Lu, Y.; Sun, Q.; Xu, Y.; Zhang, B.-B.; Jie, W.; Kanatzidis, M. G. High-sensitivity X-ray detectors based on solution-grown caesium lead bromide single crystals. *J. Mater. Chem. C* **2020**, *8* (4), 1248−1256.
(55) Sutherland, B. R.; Johnston, A. K.; Ip, A. H.; Xu, J.; Adinolfi, V.; Kanjanaboos, P.; Sargent, E. H. Sensitive, Fast, and Stable Perovskite Photodetectors Exploiting Interface Engineering. *ACS Photonics* **2015**, *2* (8), 1117−1123.
(56) Zhao, Y.; Li, C.; Shen, L. Recent advances on organic-inorganic hybrid perovskite photodetectors with fast response. *InfoMat* **2019**, *1* (2), 164−182.
(57) Green, M. A.; Dunlop, E. D.; Hohl-Ebinger, J.; Yoshita, M.; Kopidakis, N.; Ho-Baillie, A. W. Y. Solar cell efficiency tables (Version 55). *Prog. Photovoltaics* **2020**, *28* (1), 3−15.
(58) Hollemann, C.; Haase, F.; Rienäcker, M.; Barnscheidt, V.; Krügener, J.; Folchert, N.; Brendel, R.; Richter, S.; Großer, S.; Sauter, E.; Hübner, J.; Oestreich, M.; Peibst, R. Separating the two polarities of the POLO contacts of an 26.1%-efficient IBC solar cell. *Sci. Rep.* **2020**, *10* (1), 658.
(59) Becker, M. A.; Scarpelli, L.; Nedelcu, G.; Rainò, G.; Masia, F.; Borri, P.; Stöferle, T.; Kovalenko, M. V.; Langbein, W.; Mahrt, R. F. Long Exciton Dephasing Time and Coherent Phonon Coupling in $CsPbBr_2Cl$ Perovskite Nanocrystals. *Nano Lett.* **2018**, *18* (12), 7546−7551.
(60) Rainò, G.; Nedelcu, G.; Protesescu, L.; Bodnarchuk, M. I.; Kovalenko, M. V.; Mahrt, R. F.; Stöferle, T. Single Cesium Lead Halide Perovskite Nanocrystals at Low Temperature: Fast Single-Photon Emission, Reduced Blinking, and Exciton Fine Structure. *ACS Nano* **2016**, *10* (2), 2485−2490.
(61) Tamarat, P.; Bodnarchuk, M. I.; Trebbia, J.-B.; Erni, R.; Kovalenko, M. V.; Even, J.; Lounis, B. The ground exciton state of formamidinium lead bromide perovskite nanocrystals is a singlet dark state. *Nat. Mater.* **2019**, *18* (7), 717−724.
(62) Zhao, X.; Ng, J. D. A.; Friend, R. H.; Tan, Z.-K. Opportunities and challenges in perovskite light-emitting devices. *ACS Photonics* **2018**, *5* (10), 3866−3875.
(63) Imran, M.; Caligiuri, V.; Wang, M.; Goldoni, L.; Prato, M.; Krahne, R.; De Trizio, L.; Manna, L. Benzoyl Halides as Alternative Precursors for the Colloidal Synthesis of Lead-Based Halide Perovskite Nanocrystals. *J. Am. Chem. Soc.* **2018**, *140* (7), 2656−2664.
(64) Levchuk, I.; Osvet, A.; Tang, X.; Brandl, M.; Perea, J. D.; Hoegl, F.; Matt, G. J.; Hock, R.; Batentschuk, M.; Brabec, C. J. Brightly Luminescent and Color-Tunable Formamidinium Lead Halide Perovskite $FAPbX_3$ (X = Cl, Br, I) Colloidal Nanocrystals. *Nano Lett.* **2017**, *17* (5), 2765−2770.
(65) Chen, C.; Hu, X.; Lu, W.; Chang, S.; Shi, L.; Li, L.; Zhong, H.; Han, J.-B. Elucidating the phase transitions and temperature-dependent photoluminescence of $MAPbBr_3$ single crystal. *J. Phys. D: Appl. Phys.* **2018**, *51* (4), No. 045105.
(66) Whitfield, P. S.; Herron, N.; Guise, W. E.; Page, K.; Cheng, Y. Q.; Milas, I.; Crawford, M. K. Structures, Phase Transitions and Tricritical Behavior of the Hybrid Perovskite Methyl Ammonium Lead Iodide. *Sci. Rep.* **2016**, *6* (1), 35685.
(67) Hirotsu, S.; Harada, J.; Iizumi, M.; Gesi, K. Structural Phase Transitions in $CsPbBr_3$. *J. Phys. Soc. Jpn.* **1974**, *37* (5), 1393−1398.

(68) Schueller, E. C.; Laurita, G.; Fabini, D. H.; Stoumpos, C. C.; Kanatzidis, M. G.; Seshadri, R. Crystal Structure Evolution and Notable Thermal Expansion in Hybrid Perovskites Formamidinium Tin Iodide and Formamidinium Lead Bromide. *Inorg. Chem.* **2018**, *57* (2), 695−701.
(69) Protesescu, L.; Yakunin, S.; Bodnarchuk, M. I.; Bertolotti, F.; Masciocchi, N.; Guagliardi, A.; Kovalenko, M. V. Monodisperse Formamidinium Lead Bromide Nanocrystals with Bright and Stable Green Photoluminescence. *J. Am. Chem. Soc.* **2016**, *138* (43), 14202−14205.
(70) Fujii, Y.; Hoshino, S.; Yamada, Y.; Shirane, G. Neutron-Scattering Study on Phase Transitions of $CsPbCl_3$. *Phys. Rev. B* **1974**, *9* (10), 4549−4559.
(71) Binek, A.; Hanusch, F. C.; Docampo, P.; Bein, T. Stabilization of the Trigonal High-Temperature Phase of Formamidinium Lead Iodide. *J. Phys. Chem. Lett.* **2015**, *6* (7), 1249−1253.
(72) Weber, O. J.; Ghosh, D.; Gaines, S.; Henry, P. F.; Walker, A. B.; Islam, M. S.; Weller, M. T. Phase behavior and polymorphism of formamidinium lead iodide. *Chem. Mater.* **2018**, *30* (11), 3768−3778.
(73) Poglitsch, A.; Weber, D. Dynamic Disorder in Methylammoniumtrihalogenoplumbates (II) observed by Millimeter-Wave Spectroscopy. *J. Chem. Phys.* **1987**, *87* (11), 6373−6378.
(74) Chi, L.; Swainson, I.; Cranswick, L.; Her, J.-H.; Stephens, P.; Knop, O. The ordered phase of methylammonium lead chloride $CH_3ND_3PbCl_3$. *J. Solid State Chem.* **2005**, *178* (5), 1376−1385.
(75) Sutton, R. J.; Filip, M. R.; Haghighirad, A. A.; Sakai, N.; Wenger, B.; Giustino, F.; Snaith, H. J. Cubic or Orthorhombic? Revealing the Crystal Structure of Metastable Black-Phase $CsPbI_3$ by Theory and Experiment. *ACS Energy Lett.* **2018**, *3* (8), 1787−1794.
(76) Stoumpos, C. C.; Malliakas, C. D.; Kanatzidis, M. G. Semiconducting Tin and Lead Iodide Perovskites with Organic Cations: Phase Transitions, High Mobilities, and Near-Infrared Photoluminescent Properties. *Inorg. Chem.* **2013**, *52* (15), 9019−9038.
(77) Goldschmidt, V. M. Die Gesetze der Krystallochemie. *Naturwissenschaften* **1926**, *14* (21), 477−485.
(78) Kieslich, G.; Sun, S.; Cheetham, A. K. An Extended Tolerance Factor Approach for Organic−Inorganic Perovskites. *Chem. Sci.* **2015**, *6* (6), 3430−3433.
(79) Kieslich, G.; Sun, S.; Cheetham, A. K. Solid-State Principles Applied to Organic−Inorganic Perovskites: New Tricks for an Old Dog. *Chem. Sci.* **2014**, *5* (12), 4712−4715.
(80) Li, Z.; Yang, M.; Park, J.-S.; Wei, S.-H.; Berry, J. J.; Zhu, K. Stabilizing Perovskite Structures by Tuning Tolerance Factor: Formation of Formamidinium and Cesium Lead Iodide Solid-State Alloys. *Chem. Mater.* **2016**, *28* (1), 284−292.
(81) Travis, W.; Glover, E. N. K.; Bronstein, H.; Scanlon, D. O.; Palgrave, R. G. On the Application of the Tolerance Factor to Inorganic and Hybrid Halide Perovskites: a Revised System. *Chem. Sci.* **2016**, *7* (7), 4548−4556.
(82) Filip, M. R.; Eperon, G. E.; Snaith, H. J.; Giustino, F. Steric Engineering of Metal-Halide Perovskites with Tunable Optical Band Gaps. *Nat. Commun.* **2014**, *5*, 5757.
(83) Shynkarenko, Y.; Bodnarchuk, M. I.; Bernasconi, C.; Berezovska, Y.; Verteletskyi, V.; Ochsenbein, S. T.; Kovalenko, M. V. Direct Synthesis of Quaternary Alkylammonium-Capped Perovskite Nanocrystals for Efficient Blue and Green Light-Emitting Diodes. *ACS Energy Letters* **2019**, *4* (11), 2703−2711.
(84) Leijtens, T.; Eperon, G. E.; Noel, N. K.; Habisreutinger, S. N.; Petrozza, A.; Snaith, H. J. Stability of Metal Halide Perovskite Solar Cells. *Adv. Energy Mater.* **2015**, *5* (20), 1500963.
(85) Bella, F.; Renzi, P.; Cavallo, C.; Gerbaldi, C. Caesium for Perovskite Solar Cells: An Overview. *Chem. - Eur. J.* **2018**, *24* (47), 12183−12205.
(86) Gong, J.; Guo, P.; Benjamin, S. E.; Van Patten, P. G.; Schaller, R. D.; Xu, T. Cation Engineering on Lead Iodide Perovskites for Stable and High-Performance Photovoltaic Applications. *J. Energy Chem.* **2018**, *27* (4), 1017−1039.
(87) Ono, L. K.; Juarez-Perez, E. J.; Qi, Y. Progress on Perovskite Materials and Solar Cells with Mixed Cations and Halide Anions. *ACS Appl. Mater. Interfaces* **2017**, *9* (36), 30197−30246.
(88) Xu, F.; Zhang, T.; Li, G.; Zhao, Y. Mixed Cation Hybrid Lead Halide Perovskites with Enhanced Performance and Stability. *J. Mater. Chem. A* **2017**, *5* (23), 11450−11461.
(89) Zhao, P.; Yin, W.; Kim, M.; Han, M.; Song, Y. J.; Ahn, T. K.; Jung, H. S. Improved carriers injection capacity in perovskite solar cells by introducing A-site interstitial defects. *J. Mater. Chem. A* **2017**, *5* (17), 7905−7911.
(90) Saliba, M.; Matsui, T.; Domanski, K.; Seo, J.-Y.; Ummadisingu, A.; Zakeeruddin, S. M.; Correa-Baena, J.-P.; Tress, W. R.; Abate, A.; Hagfeldt, A.; Grätzel, M. Incorporation of rubidium cations into perovskite solar cells improves photovoltaic performance. *Science* **2016**, *354* (6309), 206−209.
(91) Zhou, Y.; Chen, J.; Bakr, O. M.; Sun, H.-T. Metal-Doped Lead Halide Perovskites: Synthesis, Properties, and Optoelectronic Applications. *Chem. Mater.* **2018**, *30* (19), 6589−6613.
(92) De Marco, N.; Zhou, H.; Chen, Q.; Sun, P.; Liu, Z.; Meng, L.; Yao, E.-P.; Liu, Y.; Schiffer, A.; Yang, Y. Guanidinium: A Route to Enhanced Carrier Lifetime and Open-Circuit Voltage in Hybrid Perovskite Solar Cells. *Nano Lett.* **2016**, *16* (2), 1009−1016.
(93) Hou, X.; Hu, Y.; Liu, H.; Mei, A.; Li, X.; Duan, M.; Zhang, G.; Rong, Y.; Han, H. Effect of guanidinium on mesoscopic perovskite solar cells. *J. Mater. Chem. A* **2017**, *5* (1), 73−78.
(94) Ke, W.; Spanopoulos, I.; Stoumpos, C. C.; Kanatzidis, M. G. Myths and reality of $HPbI_3$ in halide perovskite solar cells. *Nat. Commun.* **2018**, *9* (1), 4785.
(95) Eperon, G. E.; Stone, K. H.; Mundt, L. E.; Schloemer, T. H.; Habisreutinger, S. N.; Dunfield, S. P.; Schelhas, L. T.; Berry, J. J.; Moore, D. T. The Role of Dimethylammonium in Bandgap Modulation for Stable Halide Perovskites. *ACS Energy Lett.* **2020**, *5* (6), 1856−1864.
(96) Abdi-Jalebi, M.; Andaji-Garmaroudi, Z.; Cacovich, S.; Stavrakas, C.; Philippe, B.; Richter, J. M.; Alsari, M.; Booker, E. P.; Hutter, E. M.; Pearson, A. J.; Lilliu, S.; Savenije, T. J.; Rensmo, H.; Divitini, G.; Ducati, C.; Friend, R. H.; Stranks, S. D. Maximizing and stabilizing luminescence from halide perovskites with potassium passivation. *Nature* **2018**, *555* (7697), 497−501.
(97) Pering, S. R.; Deng, W.; Troughton, J. R.; Kubiak, P. S.; Ghosh, D.; Niemann, R. G.; Brivio, F.; Jeffrey, F. E.; Walker, A. B.; Islam, M. S.; Watson, T. M.; Raithby, P. R.; Johnson, A. L.; Lewis, S. E.; Cameron, P. J. Azetidinium Lead Iodide for Perovskite Solar Cells. *J. Mater. Chem. A* **2017**, *5* (39), 20658−20665.
(98) Spanopoulos, I.; Ke, W.; Stoumpos, C. C.; Schueller, E. C.; Kontsevoi, O. Y.; Seshadri, R.; Kanatzidis, M. G. Unraveling the Chemical Nature of the 3D "Hollow" Hybrid Halide Perovskites. *J. Am. Chem. Soc.* **2018**, *140* (17), 5728−5742.
(99) Zarick, H. F.; Soetan, N.; Erwin, W. R.; Bardhan, R. Mixed Halide Hybrid Perovskites: A Paradigm Shift in Photovoltaics. *J. Mater. Chem. A* **2018**, *6* (14), 5507−5537.
(100) Prasanna, R.; Gold-Parker, A.; Leijtens, T.; Conings, B.; Babayigit, A.; Boyen, H.-G.; Toney, M. F.; McGehee, M. D. Band Gap Tuning via Lattice Contraction and Octahedral Tilting in Perovskite Materials for Photovoltaics. *J. Am. Chem. Soc.* **2017**, *139* (32), 11117−11124.
(101) Tao, S.; Schmidt, I.; Brocks, G.; Jiang, J.; Tranca, I.; Meerholz, K.; Olthof, S. Absolute energy level positions in tin- and lead-based halide perovskites. *Nat. Commun.* **2019**, *10* (1), 2560.
(102) Hao, F.; Stoumpos, C. C.; Cao, D. H.; Chang, R. P. H.; Kanatzidis, M. G. Lead-free solid-state organic−inorganic halide perovskite solar cells. *Nat. Photonics* **2014**, *8* (6), 489−494.
(103) Noel, N. K.; Stranks, S. D.; Abate, A.; Wehrenfennig, C.; Guarnera, S.; Haghighirad, A.-A.; Sadhanala, A.; Eperon, G. E.; Pathak, S. K.; Johnston, M. B.; Petrozza, A.; Herz, L. M.; Snaith, H. J. Lead-free organic−inorganic tin halide perovskites for photovoltaic applications. *Energy Environ. Sci.* **2014**, *7* (9), 3061−3068.

https://dx.doi.org/10.1021/jacs.0c07338
J. Am. Chem. Soc. 2020, 142, 19413−19437

(104) Liang, L.; Gao, P. Lead-Free Hybrid Perovskite Absorbers for Viable Application: Can We Eat the Cake and Have It too? *Adv. Sci.* **2018**, *5* (2), 1700331.
(105) Eperon, G. E.; Ginger, D. S. B-Site Metal Cation Exchange in Halide Perovskites. *ACS Energy Lett.* **2017**, *2* (5), 1190−1196.
(106) Eperon, G. E.; Leijtens, T.; Bush, K. A.; Prasanna, R.; Green, T.; Wang, J. T.-W.; McMeekin, D. P.; Volonakis, G.; Milot, R. L.; May, R.; Palmstrom, A.; Slotcavage, D. J.; Belisle, R. A.; Patel, J. B.; Parrott, E. S.; Sutton, R. J.; Ma, W.; Moghadam, F.; Conings, B.; Babayigit, A.; Boyen, H.-G.; Bent, S.; Giustino, F.; Herz, L. M.; Johnston, M. B.; McGehee, M. D.; Snaith, H. J. Perovskite-perovskite tandem photovoltaics with optimized band gaps. *Science* **2016**, *354* (6314), 861−865.
(107) Zhao, B.; Abdi-Jalebi, M.; Tabachnyk, M.; Glass, H.; Kamboj, V. S.; Nie, W.; Pearson, A. J.; Puttisong, Y.; Gödel, K. C.; Beere, H. E.; Ritchie, D. A.; Mohite, A. D.; Dutton, S. E.; Friend, R. H.; Sadhanala, A. High Open-Circuit Voltages in Tin-Rich Low-Bandgap Perovskite-Based Planar Heterojunction Photovoltaics. *Adv. Mater.* **2017**, *29* (2), 1604744.
(108) Leijtens, T.; Prasanna, R.; Bush, K. A.; Eperon, G. E.; Raiford, J. A.; Gold-Parker, A.; Wolf, E. J.; Swifter, S. A.; Boyd, C. C.; Wang, H.-P.; Toney, M. F.; Bent, S. F.; McGehee, M. D. Tin−lead halide perovskites with improved thermal and air stability for efficient all-perovskite tandem solar cells. *Sustainable Energy Fuels* **2018**, *2* (11), 2450−2459.
(109) Ke, W.; Kanatzidis, M. G. Prospects for low-toxicity lead-free perovskite solar cells. *Nat. Commun.* **2019**, *10* (1), 965.
(110) Slavney, A. H.; Leppert, L.; Saldivar Valdes, A.; Bartesaghi, D.; Savenije, T. J.; Neaton, J. B.; Karunadasa, H. I. Small-Band-Gap Halide Double Perovskites. *Angew. Chem., Int. Ed.* **2018**, *57* (39), 12765−12770.
(111) Du, K.-z.; Meng, W.; Wang, X.; Yan, Y.; Mitzi, D. B. Bandgap Engineering of Lead-Free Double Perovskite $Cs_2AgBiBr_6$ through Trivalent Metal Alloying. *Angew. Chem., Int. Ed.* **2017**, *56* (28), 8158−8162.
(112) Volonakis, G.; Haghighirad, A. A.; Milot, R. L.; Sio, W. H.; Filip, M. R.; Wenger, B.; Johnston, M. B.; Herz, L. M.; Snaith, H. J.; Giustino, F. $Cs_2InAgCl_6$: A New Lead-Free Halide Double Perovskite with Direct Band Gap. *J. Phys. Chem. Lett.* **2017**, *8* (4), 772−778.
(113) Luo, J.; Li, S.; Wu, H.; Zhou, Y.; Li, Y.; Liu, J.; Li, J.; Li, K.; Yi, F.; Niu, G.; Tang, J. $Cs_2AgInCl_6$ Double Perovskite Single Crystals: Parity Forbidden Transitions and Their Application For Sensitive and Fast UV Photodetectors. *ACS Photonics* **2018**, *5* (2), 398−405.
(114) Zhou, J.; Xia, Z.; Molokeev, M. S.; Zhang, X.; Peng, D.; Liu, Q. Composition design, optical gap and stability investigations of lead-free halide double perovskite $Cs_2AgInCl_6$. *J. Mater. Chem. A* **2017**, *5* (29), 15031−15037.
(115) Shi, Z.; Guo, J.; Chen, Y.; Li, Q.; Pan, Y.; Zhang, H.; Xia, Y.; Huang, W. Lead-Free Organic−Inorganic Hybrid Perovskites for Photovoltaic Applications: Recent Advances and Perspectives. *Adv. Mater.* **2017**, *29* (16), 1605005.
(116) Etgar, L. The merit of perovskite's dimensionality; can this replace the 3D halide perovskite? *Energy Environ. Sci.* **2018**, *11* (2), 234−242.
(117) Grancini, G.; Nazeeruddin, M. K. Dimensional tailoring of hybrid perovskites for photovoltaics. *Nat. Rev. Mater.* **2019**, *4* (1), 4−22.
(118) Cao, D. H.; Stoumpos, C. C.; Farha, O. K.; Hupp, J. T.; Kanatzidis, M. G. 2D Homologous Perovskites as Light-Absorbing Materials for Solar Cell Applications. *J. Am. Chem. Soc.* **2015**, *137* (24), 7843−7850.
(119) Tsai, H.; Nie, W.; Blancon, J.-C.; Stoumpos, C. C.; Asadpour, R.; Harutyunyan, B.; Neukirch, A. J.; Verduzco, R.; Crochet, J. J.; Tretiak, S.; Pedesseau, L.; Even, J.; Alam, M. A.; Gupta, G.; Lou, J.; Ajayan, P. M.; Bedzyk, M. J.; Kanatzidis, M. G.; Mohite, A. D. High-efficiency two-dimensional Ruddlesden−Popper perovskite solar cells. *Nature* **2016**, *536* (7616), 312−316.
(120) Mao, L.; Stoumpos, C. C.; Kanatzidis, M. G. Two-Dimensional Hybrid Halide Perovskites: Principles and Promises. *J. Am. Chem. Soc.* **2019**, *141* (3), 1171−1190.
(121) Smith, M. D.; Crace, E. J.; Jaffe, A.; Karunadasa, H. I. The Diversity of Layered Halide Perovskites. *Annu. Rev. Mater. Res.* **2018**, *48* (1), 111−136.
(122) Mao, L.; Ke, W.; Pedesseau, L.; Wu, Y.; Katan, C.; Even, J.; Wasielewski, M. R.; Stoumpos, C. C.; Kanatzidis, M. G. Hybrid Dion−Jacobson 2D Lead Iodide Perovskites. *J. Am. Chem. Soc.* **2018**, *140* (10), 3775−3783.
(123) Stoumpos, C. C.; Cao, D. H.; Clark, D. J.; Young, J.; Rondinelli, J. M.; Jang, J. I.; Hupp, J. T.; Kanatzidis, M. G. Ruddlesden−Popper Hybrid Lead Iodide Perovskite 2D Homologous Semiconductors. *Chem. Mater.* **2016**, *28* (8), 2852−2867.
(124) Soe, C. M. M.; Stoumpos, C. C.; Kepenekian, M.; Traoré, B.; Tsai, H.; Nie, W.; Wang, B.; Katan, C.; Seshadri, R.; Mohite, A. D.; Even, J.; Marks, T. J.; Kanatzidis, M. G. New Type of 2D Perovskites with Alternating Cations in the Interlayer Space, $(C(NH_2)_3)(CH_3NH_3)_nPbnI_{3n+1}$: Structure, Properties, and Photovoltaic Performance. *J. Am. Chem. Soc.* **2017**, *139* (45), 16297−16309.
(125) Soe, C. M. M.; Nagabhushana, G. P.; Shivaramaiah, R.; Tsai, H.; Nie, W.; Blancon, J.-C.; Melkonyan, F.; Cao, D. H.; Traoré, B.; Pedesseau, L.; Kepenekian, M.; Katan, C.; Even, J.; Marks, T. J.; Navrotsky, A.; Mohite, A. D.; Stoumpos, C. C.; Kanatzidis, M. G. Structural and thermodynamic limits of layer thickness in 2D halide perovskites. *Proc. Natl. Acad. Sci. U. S. A.* **2019**, *116* (1), 58−66.
(126) Li, L.; Sun, Z.; Wang, P.; Hu, W.; Wang, S.; Ji, C.; Hong, M.; Luo, J. Tailored Engineering of an Unusual $(C_4H_9NH_3)_2(CH_3NH_3)_2Pb_3Br_{10}$ Two-Dimensional Multilayered Perovskite Ferroelectric for a High-Performance Photodetector. *Angew. Chem., Int. Ed.* **2017**, *56* (40), 12150−12154.
(127) Leng, K.; Fu, W.; Liu, Y.; Chhowalla, M.; Loh, K. P. From bulk to molecularly thin hybrid perovskites. *Nat. Rev. Mater.* **2020**, *5* (7), 482−500.
(128) Saparov, B.; Mitzi, D. B. Organic−Inorganic Perovskites: Structural Versatility for Functional Materials Design. *Chem. Rev.* **2016**, *116* (7), 4558−4596.
(129) Du, K.-z.; Tu, Q.; Zhang, X.; Han, Q.; Liu, J.; Zauscher, S.; Mitzi, D. B. Two-Dimensional Lead(II) Halide-Based Hybrid Perovskites Templated by Acene Alkylamines: Crystal Structures, Optical Properties, and Piezoelectricity. *Inorg. Chem.* **2017**, *56* (15), 9291−9302.
(130) Milić, J. V.; Im, J.-H.; Kubicki, D. J.; Ummadisingu, A.; Seo, J.-Y.; Li, Y.; Ruiz-Preciado, M. A.; Dar, M. I.; Zakeeruddin, S. M.; Emsley, L.; Grätzel, M. Supramolecular Engineering for Formamidinium-Based Layered 2D Perovskite Solar Cells: Structural Complexity and Dynamics Revealed by Solid-State NMR Spectroscopy. *Adv. Energy Mater.* **2019**, *9* (20), 1900284.
(131) Lermer, C.; Harm, S. P.; Birkhold, S. T.; Jaser, J. A.; Kutz, C. M.; Mayer, P.; Schmidt-Mende, L.; Lotsch, B. V. Benzimidazolium Lead Halide Perovskites: Effects of Anion Substitution and Dimensionality on the Bandgap. *Z. Anorg. Allg. Chem.* **2016**, *642* (23), 1369−1376.
(132) Mitzi, D. B.; Chondroudis, K.; Kagan, C. R. Design, Structure, and Optical Properties of Organic−Inorganic Perovskites Containing an Oligothiophene Chromophore. *Inorg. Chem.* **1999**, *38* (26), 6246−6256.
(133) Guo, Z.; Wu, X.; Zhu, T.; Zhu, X.; Huang, L. Electron−Phonon Scattering in Atomically Thin 2D Perovskites. *ACS Nano* **2016**, *10* (11), 9992−9998.
(134) Hong, X.; Ishihara, T.; Nurmikko, A. V. Dielectric confinement effect on excitons in PbI_4-based layered semiconductors. *Phys. Rev. B: Condens. Matter Mater. Phys.* **1992**, *45* (12), 6961−6964.
(135) Tanaka, K.; Kondo, T. Bandgap and exciton binding energies in lead-iodide-based natural quantum-well crystals. *Sci. Technol. Adv. Mater.* **2003**, *4* (6), 599−604.
(136) Dou, L.; Wong, A. B.; Yu, Y.; Lai, M.; Kornienko, N.; Eaton, S. W.; Fu, A.; Bischak, C. G.; Ma, J.; Ding, T.; Ginsberg, N. S.; Wang, L.-W.; Alivisatos, A. P.; Yang, P. Atomically thin two-dimensional organic-inorganic hybrid perovskites. *Science* **2015**, *349* (6255), 1518−1521.
(137) Chin, X. Y.; Perumal, A.; Bruno, A.; Yantara, N.; Veldhuis, S. A.; Martínez-Sarti, L.; Chandran, B.; Chirvony, V.; Lo, A. S.-Z.; So, J.; Soci, C.; Grätzel, M.; Bolink, H. J.; Mathews, N.; Mhaisalkar, S. G. Self-

https://dx.doi.org/10.1021/jacs.0c07338
J. Am. Chem. Soc. 2020, 142, 19413−19437

assembled hierarchical nanostructured perovskites enable highly efficient LEDs via an energy cascade. *Energy Environ. Sci.* **2018**, *11* (7), 1770−1778.
(138) Cho, H.; Jeong, S.-H.; Park, M.-H.; Kim, Y.-H.; Wolf, C.; Lee, C.-L.; Heo, J. H.; Sadhanala, A.; Myoung, N.; Yoo, S.; Im, S. H.; Friend, R. H.; Lee, T.-W. Overcoming the electroluminescence efficiency limitations of perovskite light-emitting diodes. *Science* **2015**, *350* (6265), 1222−1225.
(139) Yuan, M.; Quan, L. N.; Comin, R.; Walters, G.; Sabatini, R.; Voznyy, O.; Hoogland, S.; Zhao, Y.; Beauregard, E. M.; Kanjanaboos, P.; Lu, Z.; Kim, D. H.; Sargent, E. H. Perovskite energy funnels for efficient light-emitting diodes. *Nat. Nanotechnol.* **2016**, *11* (10), 872−877.
(140) Grätzel, M. The Rise of Highly Efficient and Stable Perovskite Solar Cells. *Acc. Chem. Res.* **2017**, *50* (3), 487−491.
(141) Li, J.; Wang, J.; Ma, J.; Shen, H.; Li, L.; Duan, X.; Li, D. Self-trapped state enabled filterless narrowband photodetections in 2D layered perovskite single crystals. *Nat. Commun.* **2019**, *10* (1), 806.
(142) Tsai, H.; Liu, F.; Shrestha, S.; Fernando, K.; Tretiak, S.; Scott, B.; Vo, D. T.; Strzalka, J.; Nie, W. A sensitive and robust thin-film x-ray detector using 2D layered perovskite diodes. *Sci. Adv.* **2020**, *6* (15), No. eaay0815.
(143) Li, L.; Shang, X.; Wang, S.; Dong, N.; Ji, C.; Chen, X.; Zhao, S.; Wang, J.; Sun, Z.; Hong, M.; Luo, J. Bilayered Hybrid Perovskite Ferroelectric with Giant Two-Photon Absorption. *J. Am. Chem. Soc.* **2018**, *140* (22), 6806−6809.
(144) Shahrokhi, S.; Gao, W.; Wang, Y.; Anandan, P. R.; Rahaman, M. Z.; Singh, S.; Wang, D.; Cazorla, C.; Yuan, G.; Liu, J.-M.; Wu, T. Emergence of Ferroelectricity in Halide Perovskites. *Small Methods* **2020**, *4*, 2000149.
(145) Lu, H.; Xiao, C.; Song, R.; Li, T.; Maughan, A. E.; Levin, A.; Brunecky, R.; Berry, J. J.; Mitzi, D. B.; Blum, V.; Beard, M. C. Highly Distorted Chiral Two-Dimensional Tin Iodide Perovskites for Spin Polarized Charge Transport. *J. Am. Chem. Soc.* **2020**, *142* (30), 13030−13040.
(146) Ma, J.; Fang, C.; Chen, C.; Jin, L.; Wang, J.; Wang, S.; Tang, J.; Li, D. Chiral 2D Perovskites with a High Degree of Circularly Polarized Photoluminescence. *ACS Nano* **2019**, *13* (3), 3659−3665.
(147) Chen, C.; Gao, L.; Gao, W.; Ge, C.; Du, X.; Li, Z.; Yang, Y.; Niu, G.; Tang, J. Circularly polarized light detection using chiral hybrid perovskite. *Nat. Commun.* **2019**, *10* (1), 1927.
(148) Long, G.; Sabatini, R.; Saidaminov, M. I.; Lakhwani, G.; Rasmita, A.; Liu, X.; Sargent, E. H.; Gao, W. Chiral-perovskite optoelectronics. *Nat. Rev. Mater.* **2020**, *5* (6), 423−439.
(149) Saouma, F. O.; Stoumpos, C. C.; Wong, J.; Kanatzidis, M. G.; Jang, J. I. Selective enhancement of optical nonlinearity in two-dimensional organic-inorganic lead iodide perovskites. *Nat. Commun.* **2017**, *8* (1), 742.
(150) Kondo, T.; Iwamoto, S.; Hayase, S.; Tanaka, K.; Ishi, J.; Mizuno, M.; Ema, K.; Ito, R. Resonant third-order optical nonlinearity in the layered perovskite-type material $(C_6H_{13}NH_3)_2PbI_4$. *Solid State Commun.* **1998**, *105* (8), 503−506.
(151) Wang, J.; Mi, Y.; Gao, X.; Li, J.; Li, J.; Lan, S.; Fang, C.; Shen, H.; Wen, X.; Chen, R.; Liu, X.; He, T.; Li, D. Giant Nonlinear Optical Response in 2D Perovskite Heterostructures. *Adv. Opt. Mater.* **2019**, *7* (15), 1900398.
(152) Walters, G.; Haeberlé, L.; Quintero-Bermudez, R.; Brodeur, J.; Kéna-Cohen, S.; Sargent, E. H. Directional Light Emission from Layered Metal Halide Perovskite Crystals. *J. Phys. Chem. Lett.* **2020**, *11* (9), 3458−3465.
(153) Lanty, G.; Jemli, K.; Wei, Y.; Leymarie, J.; Even, J.; Lauret, J.-S.; Deleporte, E. Room-Temperature Optical Tunability and Inhomogeneous Broadening in 2D-Layered Organic−Inorganic Perovskite Pseudobinary Alloys. *J. Phys. Chem. Lett.* **2014**, *5* (22), 3958−3963.
(154) Zhang, F.; Lu, H.; Tong, J.; Berry, J. J.; Beard, M. C.; Zhu, K. Advances in two-dimensional organic−inorganic hybrid perovskites. *Energy Environ. Sci.* **2020**, *13* (4), 1154−1186.
(155) Smith, M. D.; Connor, B. A.; Karunadasa, H. I. Tuning the Luminescence of Layered Halide Perovskites. *Chem. Rev.* **2019**, *119* (5), 3104−3139.
(156) Niesner, D.; Wilhelm, M.; Levchuk, I.; Osvet, A.; Shrestha, S.; Batentschuk, M.; Brabec, C.; Fauster, T. Giant Rashba Splitting in $CH_3NH_3PbBr_3$ Organic-Inorganic Perovskite. *Phys. Rev. Lett.* **2016**, *117* (12), 126401.
(157) Isarov, M.; Tan, L. Z.; Bodnarchuk, M. I.; Kovalenko, M. V.; Rappe, A. M.; Lifshitz, E. Rashba Effect in a Single Colloidal $CsPbBr_3$ Perovskite Nanocrystal Detected by Magneto-Optical Measurements. *Nano Lett.* **2017**, *17* (8), 5020−5026.
(158) Mosconi, E.; Etienne, T.; De Angelis, F. Rashba Band Splitting in Organohalide Lead Perovskites: Bulk and Surface Effects. *J. Phys. Chem. Lett.* **2017**, *8* (10), 2247−2252.
(159) Che, X.; Traore, B.; Katan, C.; Kepenekian, M.; Even, J. Does Rashba splitting in $CH_3NH_3PbBr_3$ arise from 2 × 2 surface reconstruction? *Phys. Chem. Chem. Phys.* **2018**, *20* (14), 9638−9643.
(160) Zhai, Y.; Baniya, S.; Zhang, C.; Li, J.; Haney, P.; Sheng, C.-X.; Ehrenfreund, E.; Vardeny, Z. V. Giant Rashba splitting in 2D organic-inorganic halide perovskites measured by transient spectroscopies. *Sci. Adv.* **2017**, *3* (7), No. e1700704.
(161) Todd, S. B.; Riley, D. B.; Binai-Motlagh, A.; Clegg, C.; Ramachandran, A.; March, S. A.; Hoffman, J. M.; Hill, I. G.; Stoumpos, C. C.; Kanatzidis, M. G.; Yu, Z.-G.; Hall, K. C. Detection of Rashba spin splitting in 2D organic-inorganic perovskite via precessional carrier spin relaxation. *APL Mater.* **2019**, *7* (8), No. 081116.
(162) Giovanni, D.; Chong, W. K.; Dewi, H. A.; Thirumal, K.; Neogi, I.; Ramesh, R.; Mhaisalkar, S.; Mathews, N.; Sum, T. C. Tunable room-temperature spin-selective optical Stark effect in solution-processed layered halide perovskites. *Sci. Adv.* **2016**, *2* (6), No. e1600477.
(163) Long, G.; Jiang, C.; Sabatini, R.; Yang, Z.; Wei, M.; Quan, L. N.; Liang, Q.; Rasmita, A.; Askerka, M.; Walters, G.; Gong, X.; Xing, J.; Wen, X.; Quintero-Bermudez, R.; Yuan, H.; Xing, G.; Wang, X. R.; Song, D.; Voznyy, O.; Zhang, M.; Hoogland, S.; Gao, W.; Xiong, Q.; Sargent, E. H. Spin control in reduced-dimensional chiral perovskites. *Nat. Photonics* **2018**, *12* (9), 528−533.
(164) Giovanni, D.; Lim, J. W. M.; Yuan, Z.; Lim, S. S.; Righetto, M.; Qing, J.; Zhang, Q.; Dewi, H. A.; Gao, F.; Mhaisalkar, S. G.; Mathews, N.; Sum, T. C. Ultrafast long-range spin-funneling in solution-processed Ruddlesden−Popper halide perovskites. *Nat. Commun.* **2019**, *10* (1), 3456.
(165) Grancini, G.; Roldán-Carmona, C.; Zimmermann, I.; Mosconi, E.; Lee, X.; Martineau, D.; Narbey, S.; Oswald, F.; De Angelis, F.; Graetzel, M.; Nazeeruddin, M. K. One-Year stable perovskite solar cells by 2D/3D interface engineering. *Nat. Commun.* **2017**, *8* (1), 15684.
(166) Gao, P.; Bin Mohd Yusoff, A. R.; Nazeeruddin, M. K. Dimensionality engineering of hybrid halide perovskite light absorbers. *Nat. Commun.* **2018**, *9* (1), 5028.
(167) Schileo, G.; Grancini, G. Halide perovskites: current issues and new strategies to push material and device stability. *J. Phys. Energy* **2020**, *2* (2), No. 021005.
(168) Na Quan, L.; Ma, D.; Zhao, Y.; Voznyy, O.; Yuan, H.; Bladt, E.; Pan, J.; García de Arquer, F. P.; Sabatini, R.; Piontkowski, Z.; Emwas, A.-H.; Todorović, P.; Quintero-Bermudez, R.; Walters, G.; Fan, J. Z.; Liu, M.; Tan, H.; Saidaminov, M. I.; Gao, L.; Li, Y.; Anjum, D. H.; Wei, N.; Tang, J.; McCamant, D. W.; Roeffaers, M. B. J.; Bals, S.; Hofkens, J.; Bakr, O. M.; Lu, Z.-H.; Sargent, E. H. Edge stabilization in reduced-dimensional perovskites. *Nat. Commun.* **2020**, *11* (1), 170.
(169) Park, M.-H.; Kim, J. S.; Heo, J.-M.; Ahn, S.; Jeong, S.-H.; Lee, T.-W. Boosting Efficiency in Polycrystalline Metal Halide Perovskite Light-Emitting Diodes. *ACS Energy Lett.* **2019**, *4* (5), 1134−1149.
(170) Xiao, Z.; Kerner, R. A.; Zhao, L.; Tran, N. L.; Lee, K. M.; Koh, T.-W.; Scholes, G. D.; Rand, B. P. Efficient perovskite light-emitting diodes featuring nanometre-sized crystallites. *Nat. Photonics* **2017**, *11* (2), 108−115.
(171) Lin, H.; Zhou, C.; Tian, Y.; Siegrist, T.; Ma, B. Low-Dimensional Organometal Halide Perovskites. *ACS Energy Lett.* **2018**, *3* (1), 54−62.

https://dx.doi.org/10.1021/jacs.0c07338
J. Am. Chem. Soc. 2020, 142, 19413−19437

(172) Dohner, E. R.; Hoke, E. T.; Karunadasa, H. I. Self-Assembly of Broadband White-Light Emitters. *J. Am. Chem. Soc.* **2014**, *136* (5), 1718−1721.
(173) Katan, C.; Mercier, N.; Even, J. Quantum and Dielectric Confinement Effects in Lower-Dimensional Hybrid Perovskite Semiconductors. *Chem. Rev.* **2019**, *119* (5), 3140−3192.
(174) McCall, K. M.; Morad, V.; Benin, B. M.; Kovalenko, M. V. Efficient Lone Pair-Driven Luminescence: Structure-Property Relationships in Emissive $5s^2$ Metal Halides. *ACS Mater. Lett.* **2020**, *2* (9), 1218−1232.
(175) Levitt, M. H. *Spin Dynamics. Basics of Nuclear Magnetic Resonance*; John Wiley & Sons, Ltd.: Chichester, U.K., 2008.
(176) Keeler, J. *Understanding NMR Spectroscopy*; Wiley: Chichester, U.K., 2005.
(177) Duer, M. J. *Introduction to Solid-State NMR Spectroscopy*; Blackwell Publishing: Oxford, U.K., 2004.
(178) Anusca, I.; Balčiūnas, S.; Gemeiner, P.; Svirskas, Š.; Sanlialp, M.; Lackner, G.; Fettkenhauer, C.; Belovickis, J.; Samulionis, V.; Ivanov, M.; Dkhil, B.; Banys, J.; Shvartsman, V. V.; Lupascu, D. C. Dielectric Response: Answer to Many Questions in the Methylammonium Lead Halide Solar Cell Absorbers. *Adv. Energy Mater.* **2017**, *7* (19), 1700600.
(179) Miyata, K.; Atallah, T. L.; Zhu, X.-Y. Lead halide perovskites: Crystal-liquid duality, phonon glass electron crystals, and large polaron formation. *Sci. Adv.* **2017**, *3* (10), No. e1701469.
(180) Guo, Y.; Yaffe, O.; Hull, T. D.; Owen, J. S.; Reichman, D. R.; Brus, L. E. Dynamic emission Stokes shift and liquid-like dielectric solvation of band edge carriers in lead-halide perovskites. *Nat. Commun.* **2019**, *10* (1), 1175.
(181) Chu, W.; Zheng, Q.; Prezhdo, O. V.; Zhao, J.; Saidi, W. A. Low-frequency lattice phonons in halide perovskites explain high defect tolerance toward electron-hole recombination. *Sci. Adv.* **2020**, *6* (7), No. eaaw7453.
(182) Joshi, P. P.; Maehrlein, S. F.; Zhu, X. Dynamic Screening and Slow Cooling of Hot Carriers in Lead Halide Perovskites. *Adv. Mater.* **2019**, *31* (47), 1803054.
(183) Palmieri, T.; Baldini, E.; Steinhoff, A.; Akrap, A.; Kollár, M.; Horváth, E.; Forró, L.; Jahnke, F.; Chergui, M. Mahan excitons in room-temperature methylammonium lead bromide perovskites. *Nat. Commun.* **2020**, *11* (1), 850.
(184) Franssen, W. M. J.; Kentgens, A. P. M. Solid−state NMR of hybrid halide perovskites. *Solid State Nucl. Magn. Reson.* **2019**, *100*, 36−44.
(185) Bernard, G. M.; Wasylishen, R. E.; Ratcliffe, C. I.; Terskikh, V.; Wu, Q.; Buriak, J. M.; Hauger, T. Methylammonium Cation Dynamics in Methylammonium Lead Halide Perovskites: A Solid-State NMR Perspective. *J. Phys. Chem. A* **2018**, *122* (6), 1560−1573.
(186) Senocrate, A.; Maier, J. Solid state ionics of hybrid halide perovskites. *J. Am. Chem. Soc.* **2019**, *141* (21), 8382−8396.
(187) Bonhomme, C.; Gervais, C.; Babonneau, F.; Coelho, C.; Pourpoint, F.; Azaïs, T.; Ashbrook, S. E.; Griffin, J. M.; Yates, J. R.; Mauri, F.; Pickard, C. J. First-Principles Calculation of NMR Parameters Using the Gauge Including Projector Augmented Wave Method: A Chemist's Point of View. *Chem. Rev.* **2012**, *112* (11), 5733−5779.
(188) Charpentier, T.; Menziani, M. C.; Pedone, A. Computational simulations of solid state NMR spectra: a new era in structure determination of oxide glasses. *RSC Adv.* **2013**, *3* (27), 10550−10578.
(189) Ashbrook, S. E.; Hodgkinson, P. Perspective: Current advances in solid-state NMR spectroscopy. *J. Chem. Phys.* **2018**, *149* (4), No. 040901.
(190) Hidaka, M.; Okamoto, Y.; Zikumaru, Y. Structural Phase Transition of $CsPbCl_3$ below Room Temperature. *Phys. Status Solidi A* **1983**, *79* (1), 263−269.
(191) Karmakar, A.; Dodd, M. S.; Zhang, X.; Oakley, M. S.; Klobukowski, M.; Michaelis, V. K. Mechanochemical synthesis of 0D and 3D cesium lead mixed halide perovskites. *Chem. Commun.* **2019**, *55* (35), 5079−5082.
(192) Kubicki, D. J.; Prochowicz, D.; Hofstetter, A.; Zakeeruddin, S. M.; Grätzel, M.; Emsley, L. Phase Segregation in Cs-, Rb- and K-Doped Mixed-Cation $(MA)_x(FA)_{1-x}PbI_3$ Hybrid Perovskites from Solid-State NMR. *J. Am. Chem. Soc.* **2017**, *139* (40), 14173−14180.
(193) Kubicki, D. J.; Prochowicz, D.; Hofstetter, A.; Zakeeruddin, S. M.; Grätzel, M.; Emsley, L. Phase Segregation in Potassium-Doped Lead Halide Perovskites from ^{39}K solid-state NMR at 21.1 T. *J. Am. Chem. Soc.* **2018**, *140* (23), 7232−7238.
(194) Senocrate, A.; Moudrakovski, I.; Kim, G. Y.; Yang, T.-Y.; Gregori, G.; Grätzel, M.; Maier, J. The Nature of Ion Conduction in Methylammonium Lead Iodide: A Multimethod Approach. *Angew. Chem., Int. Ed.* **2017**, *56* (27), 7755−7759.
(195) Volkov, A. F.; Venevtsev, Y. N.; Semin, G. K. Nuclear Quadrupole Resonance (NQR) of ^{79}Br and ^{81}Br in Perovskite and Orthorhombic Forms of $CsPbBr_3$ and $CsPbJ_3$. *Phys. Status Solidi B* **1969**, *35* (2), K167−K169.
(196) Xu, Q.; Eguchi, T.; Nakayama, H.; Nakamura, N.; Kishita, M. Molecular Motions and Phase Transitions in Solid $CH_3NH_3PbX_3$ (X = Cl, Br, I) as Studied by NMR and NQR. *Z. Naturforsch., A: Phys. Sci.* **1991**, *46*, 240−246.
(197) Yamada, K.; Hino, S.; Hirose, S.; Yamane, Y.; Turkevych, I.; Urano, T.; Tomiyasu, H.; Yamagishi, H.; Aramaki, S. Static and Dynamic Structures of Perovskite Halides ABX_3 (B = Pb, Sn) and Their Characteristic Semiconducting Properties by a Hückel Analytical Calculation. *Bull. Chem. Soc. Jpn.* **2018**, *91* (8), 1196−1204.
(198) Stoumpos, C. C.; Kanatzidis, M. G. The Renaissance of Halide Perovskites and Their Evolution as Emerging Semiconductors. *Acc. Chem. Res.* **2015**, *48* (10), 2791−2802.
(199) Saliba, M.; Matsui, T.; Domanski, K.; Seo, J.; Zakeeruddin, S. M.; Tress, W. R.; Graetzel, M. Mixed Cation Perovskite Solid State Solar Cell and Fabrication Thereof. European Patent 3,272,757, 2018.
(200) Bing, J.; Lee, D. S.; Zheng, J.; Zhang, M.; Li, Y.; Kim, J.; Lau, C. F. J.; Cho, Y.; Green, M. A.; Huang, S.; Ho-Baillie, A. W. Y. Deconstruction-assisted perovskite formation for sequential solution processing of $Cs_{0.15}(MA_{0.7}FA_{0.3})_{0.85}PbI_3$ solar cells. *Sol. Energy Mater. Sol. Cells* **2019**, *203*, 110200.
(201) Christians, J. A.; Schulz, P.; Tinkham, J. S.; Schloemer, T. H.; Harvey, S. P.; Tremolet de Villers, B. J.; Sellinger, A.; Berry, J. J.; Luther, J. M. Tailored interfaces of unencapsulated perovskite solar cells for > 1,000 h operational stability. *Nat. Energy* **2018**, *3* (1), 68−74.
(202) Saidaminov, M. I.; Williams, K.; Wei, M.; Johnston, A.; Quintero-Bermudez, R.; Vafaie, M.; Pina, J. M.; Proppe, A. H.; Hou, Y.; Walters, G.; Kelley, S. O.; Tisdale, W. A.; Sargent, E. H. Multi-cation perovskites prevent carrier reflection from grain surfaces. *Nat. Mater.* **2020**, *19* (4), 412−418.
(203) Armstrong, R. L.; Lourens, J. A. J.; Stroud, J. D. ^{133}Cs spin-Lattice Relaxation Study of Phase Transitions in $CsPbCl_3$. *Phys. Rev. B* **1976**, *13* (11), 5099−5101.
(204) Plesko, S.; Kind, R.; Roos, J. Structural Phase Transitions in $CsPbCl_3$ and $RbCdCl_3$. *J. Phys. Soc. Jpn.* **1978**, *45* (2), 553−557.
(205) Sharma, S.; Weiden, N.; Weiss, A. Phase Transitions in $CsSnCl_3$ and $CsPbBr_3$ An NMR and NQR Study. *Z. Naturforsch., A: Phys. Sci.* **1991**, *46*, 329−336.
(206) Roiland, C.; Trippe-Allard, G.; Jemli, K.; Alonso, B.; Ameline, J.-C.; Gautier, R.; Bataille, T.; Le Polles, L.; Deleporte, E.; Even, J.; Katan, C. Multinuclear NMR as a Tool for Studying Local Order and Dynamics in $CH_3NH_3PbX_3$ (X = Cl, Br, I) Hybrid Perovskites. *Phys. Chem. Chem. Phys.* **2016**, *18* (39), 27133−27142.
(207) Acik, M.; Alam, T. M.; Guo, F.; Ren, Y.; Lee, B.; Rosenberg, R. A.; Mitchell, J. F.; Park, I. K.; Lee, G.; Darling, S. B. Substitutional Growth of Methylammonium Lead Iodide Perovskites in Alcohols. *Adv. Energy Mater.* **2018**, *8* (5), 1701726.
(208) Chen, Y.-F.; Tsai, Y.-T.; Hirsch, L.; Bassani, D. M. Kinetic Isotope Effects Provide Experimental Evidence for Proton Tunneling in Methylammonium Lead Triiodide Perovskites. *J. Am. Chem. Soc.* **2017**, *139* (45), 16359−16364.
(209) Fabini, D. H.; Siaw, T. A.; Stoumpos, C. C.; Laurita, G.; Olds, D.; Page, K.; Hu, J. G.; Kanatzidis, M. G.; Han, S.; Seshadri, R. Universal Dynamics of Molecular Reorientation in Hybrid Lead Iodide Perovskites. *J. Am. Chem. Soc.* **2017**, *139* (46), 16875−16884.

(210) Lu, J.; Jiang, L.; Li, W.; Li, F.; Pai, N. K.; Scully, A. D.; Tsai, C.-M.; Bach, U.; Simonov, A. N.; Cheng, Y.-B.; Spiccia, L. Diammonium and Monoammonium Mixed-Organic-Cation Perovskites for High Performance Solar Cells with Improved Stability. *Adv. Energy Mater.* **2017**, *7* (18), 1700444.
(211) Si, H.; Liao, Q.; Kang, Z.; Ou, Y.; Meng, J.; Liu, Y.; Zhang, Z.; Zhang, Y. Deciphering the NH_4PbI_3 Intermediate Phase for Simultaneous Improvement on Nucleation and Crystal Growth of Perovskite. *Adv. Funct. Mater.* **2017**, *27* (30), 1701804.
(212) Ban, M.; Zou, Y.; Rivett, J. P. H.; Yang, Y.; Thomas, T. H.; Tan, Y.; Song, T.; Gao, X.; Credgington, D.; Deschler, F.; Sirringhaus, H.; Sun, B. Solution-Processed Perovskite Light Emitting Diodes with Efficiency Exceeding 15% through Additive-Controlled Nanostructure Tailoring. *Nat. Commun.* **2018**, *9* (1), 3892.
(213) Colella, S.; Todaro, M.; Masi, S.; Listorti, A.; Altamura, D.; Caliandro, R.; Giannini, C.; Carignani, E.; Geppi, M.; Meggiolaro, D.; Buscarino, G.; De Angelis, F.; Rizzo, A. Light-Induced Formation of Pb^{3+} Paramagnetic Species in Lead Halide Perovskites. *ACS Energy Lett.* **2018**, *3* (8), 1840−1847.
(214) Kerner, R.; Schloemer, T. H.; Schulz, P.; Berry, J. J.; Schwartz, J.; Sellinger, A.; Rand, B. P. Amine Additive Reactions Induced by the Soft Lewis Acidity of Pb^{2+} in Halide Perovskites. Part I: Evidence for Pb-Alkylmide Formation. *J. Mater. Chem. C* **2019**, *7*, 5251−5259.
(215) Kubicki, D. J.; Prochowicz, D.; Hofstetter, A.; Saski, M.; Yadav, P.; Bi, D.; Pellet, N.; Lewiński, J.; Zakeeruddin, S. M.; Grätzel, M.; Emsley, L. Formation of Stable Mixed Guanidinium−Methylammonium Phases with Exceptionally Long Carrier Lifetimes for High-Efficiency Lead Iodide-Based Perovskite Photovoltaics. *J. Am. Chem. Soc.* **2018**, *140* (9), 3345−3351.
(216) Mencel, K.; Durlak, P.; Rok, M.; Jakubas, R.; Baran, J.; Medycki, W.; Ciżman, A.; Piecha-Bisiorek, A. Widely Used Hardly Known. An Insight into Electric and Dynamic Properties of Formamidinium Iodide. *RSC Adv.* **2018**, *8* (47), 26506−26516.
(217) Prochowicz, D.; Yadav, P.; Saliba, M.; Kubicki, D. J.; Tavakoli, M. M.; Zakeeruddin, S. M.; Lewiński, J.; Emsley, L.; Grätzel, M. One-Step Mechanochemical Incorporation of an Insoluble Cesium Additive for High Performance Planar Heterojunction Solar Cells. *Nano Energy* **2018**, *49*, 523−528.
(218) Yong, Z.-J.; Guo, S.-Q.; Ma, J.-P.; Zhang, J.-Y.; Li, Z.-Y.; Chen, Y.-M.; Zhang, B.-B.; Zhou, Y.; Shu, J.; Gu, J.-L.; Zheng, L.-R.; Bakr, O. M.; Sun, H.-T. Doping-Enhanced Short-Range Order of Perovskite Nanocrystals for Near-Unity Violet Luminescence Quantum Yield. *J. Am. Chem. Soc.* **2018**, *140* (31), 9942−9951.
(219) Franssen, W. M. J.; van Es, S. G. D.; Dervişoğlu, R.; de Wijs, G. A.; Kentgens, A. P. M. Symmetry, Dynamics, and Defects in Methylammonium Lead Halide Perovskites. *J. Phys. Chem. Lett.* **2017**, *8* (1), 61−66.
(220) Wasylishen, R. E.; Knop, O.; Macdonald, J. B. Cation Rotation in Methylammonium Lead Halides. *Solid State Commun.* **1985**, *56* (7), 581−582.
(221) Baikie, T.; Barrow, N. S.; Fang, Y.; Keenan, P. J.; Slater, P. R.; Piltz, R. O.; Gutmann, M.; Mhaisalkar, S. G.; White, T. J. A Combined Single Crystal Neutron/X-ray Diffraction and Solid-State Nuclear Magnetic Resonance Study of the Hybrid Perovskites $CH_3NH_3PbX_3$ (X = I, Br and Cl). *J. Mater. Chem. A* **2015**, *3* (17), 9298−9307.
(222) Kubicki, D. J.; Prochowicz, D.; Hofstetter, A.; Péchy, P.; Zakeeruddin, S. M.; Grätzel, M.; Emsley, L. Cation Dynamics in Mixed-Cation $(MA)_x(FA)_{1-x}PbI_3$ Hybrid Perovskites from Solid-State NMR. *J. Am. Chem. Soc.* **2017**, *139* (29), 10055−10061.
(223) Senocrate, A.; Moudrakovski, I.; Acartürk, T.; Merkle, R.; Kim, G. Y.; Starke, U.; Grätzel, M.; Maier, J. Slow $CH_3NH_3^+$ Diffusion in $CH_3NH_3PbI_3$ under Light Measured by Solid-State NMR and Tracer Diffusion. *J. Phys. Chem. C* **2018**, *122* (38), 21803−21806.
(224) Senocrate, A.; Moudrakovski, I.; Maier, J. Short-Range Ion Dynamics in Methylammonium Lead Iodide by Multinuclear Solid State NMR and ^{127}I NQR. *Phys. Chem. Chem. Phys.* **2018**, *20* (30), 20043−20055.
(225) Knop, O.; Wasylishen, R. E.; White, M. A.; Cameron, T. S.; Oort, M. J. M. V. Alkylammonium Lead Halides. Part 2. $CH_3NH_3PbX_3$ (X = Cl, Br, I) Perovskites: Cuboctahedral Halide Cages with Isotropic Cation Reorientation. *Can. J. Chem.* **1990**, *68* (3), 412−422.
(226) Dai, J.; Fu, Y.; Manger, L. H.; Rea, M. T.; Hwang, L.; Goldsmith, R. H.; Jin, S. Carrier Decay Properties of Mixed Cation Formamidinium−Methylammonium Lead Iodide Perovskite $[HC(NH_2)_2]_{1-x}[CH_3NH_3]_xPbI_3$ Nanorods. *J. Phys. Chem. Lett.* **2016**, *7* (24), 5036−5043.
(227) Chen, B.-X.; Li, W.-G.; Rao, H.-S.; Xu, Y.-F.; Kuang, D.-B.; Su, C.-Y. Large-Grained Perovskite Films via $FA_xMA_{1-x}Pb(I_xBr_{1-x})_3$ Single Crystal Precursor for Efficient Solar Cells. *Nano Energy* **2017**, *34*, 264−270.
(228) Huang, Y.; Li, L.; Liu, Z.; Jiao, H.; He, Y.; Wang, X.; Zhu, R.; Wang, D.; Sun, J.; Chen, Q.; Zhou, H. The Intrinsic Properties of $FA_{(1-x)}MA_xPbI_3$ Perovskite Single Crystals. *J. Mater. Chem. A* **2017**, *5* (18), 8537−8544.
(229) Jodlowski, A. D.; Roldán-Carmona, C.; Grancini, G.; Salado, M.; Ralaiarisoa, M.; Ahmad, S.; Koch, N.; Camacho, L.; de Miguel, G.; Nazeeruddin, M. K. Large Guanidinium Cation Mixed with Methylammonium in Lead Iodide Perovskites for 19% Efficient Solar Cells. *Nat. Energy* **2017**, *2* (12), 972−979.
(230) Li, C.; Zhou, Y.; Wang, L.; Chang, Y.; Zong, Y.; Etgar, L.; Cui, G.; Padture, N. P.; Pang, S. Methylammonium-Mediated Evolution of Mixed-Organic-Cation Perovskite Thin Films: A Dynamic Composition-Tuning Process. *Angew. Chem.* **2017**, *129* (26), 7782−7786.
(231) Li, W.-G.; Rao, H.-S.; Chen, B.-X.; Wang, X.-D.; Kuang, D.-B. A Formamidinium−Methylammonium Lead Iodide Perovskite Single Crystal Exhibiting Exceptional Optoelectronic Properties and Long-Term Stability. *J. Mater. Chem. A* **2017**, *5* (36), 19431−19438.
(232) Longo, G.; Wong, A.; Sessolo, M.; Bolink, H. J. Effect of the Precursor's Stoichiometry on the Optoelectronic Properties of Methylammonium Lead Bromide Perovskites. *J. Lumin.* **2017**, *189*, 120−125.
(233) Pont, S.; Bryant, D.; Lin, C.-T.; Aristidou, N.; Wheeler, S.; Ma, X.; Godin, R.; Haque, S. A.; Durrant, J. R. Tuning $CH_3NH_3Pb(I_{1-x}Br_x)_3$ Perovskite Oxygen Stability in Thin Films and Solar Cells. *J. Mater. Chem. A* **2017**, *5* (20), 9553−9560.
(234) Wang, C.; Yang, S.; Chen, X.; Wen, T.; Yang, H. G. Surface-Functionalized Perovskite Films for Stable Photoelectrochemical Water Splitting. *J. Mater. Chem. A* **2017**, *5* (3), 910−913.
(235) Daub, M.; Hillebrecht, H. Tailoring the Band Gap in 3D Hybrid Perovskites by Substitution of the Organic Cations: $(CH_3NH_3)_{1-2y}(NH_3(CH_2)_2NH_3)_{2y}Pb_{1-y}I_3$ ($0 \le y \le 0.25$). *Chem. - Eur. J.* **2018**, *24* (36), 9075−9082.
(236) Franssen, W.; Bruijnaers, B.; Portengen, V.; Kentgens, A. Dimethylammonium Incorporation in Lead Acetate based $MAPbI_3$ Perovskite Solar Cells. *ChemPhysChem* **2018**, *19*, 3107.
(237) Nayak, P. K.; Sendner, M.; Wenger, B.; Wang, Z.; Sharma, K.; Ramadan, A. J.; Lovrinčić, R.; Pucci, A.; Madhu, P. K.; Snaith, H. J. Impact of Bi^{3+} Heterovalent Doping in Organic−Inorganic Metal Halide Perovskite Crystals. *J. Am. Chem. Soc.* **2018**, *140* (2), 574−577.
(238) Pareja-Rivera, C.; Solís-Cambero, A. L.; Sánchez-Torres, M.; Lima, E.; Solis-Ibarra, D. On the True Composition of Mixed-Cation Perovskite Films. *ACS Energy Lett.* **2018**, *3* (10), 2366−2367.
(239) Saidaminov, M. I.; Kim, J.; Jain, A.; Quintero-Bermudez, R.; Tan, H.; Long, G.; Tan, F.; Johnston, A.; Zhao, Y.; Voznyy, O.; Sargent, E. H. Suppression of Atomic Vacancies via Incorporation of Isovalent Small Ions to Increase the Stability of Halide Perovskite Solar Cells in Ambient Air. *Nat. Energy* **2018**, *3* (8), 648−654.
(240) Sun, M.; Liang, C.; Zhang, H.; Ji, C.; Sun, F.; You, F.; Jing, X.; He, Z. Tailoring a Dynamic Crystalline Process during the Conversion of Lead-Halide Perovskite Layer to Achieve High Performance Solar Cells. *J. Mater. Chem. A* **2018**, *6*, 24793−24804.
(241) Tan, H.; Che, F.; Wei, M.; Zhao, Y.; Saidaminov, M. I.; Todorović, P.; Broberg, D.; Walters, G.; Tan, F.; Zhuang, T.; Sun, B.; Liang, Z.; Yuan, H.; Fron, E.; Kim, J.; Yang, Z.; Voznyy, O.; Asta, M.; Sargent, E. H. Dipolar Cations Confer Defect Tolerance in Wide-Bandgap Metal Halide Perovskites. *Nat. Commun.* **2018**, *9* (1), 3100.
(242) Van Gompel, W. T. M.; Herckens, R.; Reekmans, G.; Ruttens, B.; D'Haen, J.; Adriaensens, P.; Lutsen, L.; Vanderzande, D.

https://dx.doi.org/10.1021/jacs.0c07338
J. Am. Chem. Soc. 2020, 142, 19413−19437

Degradation of the Formamidinium Cation and the Quantification of the Formamidinium−Methylammonium Ratio in Lead Iodide Hybrid Perovskites by Nuclear Magnetic Resonance Spectroscopy. *J. Phys. Chem. C* **2018**, *122* (8), 4117−4124.
(243) Bakulin, A. A.; Selig, O.; Bakker, H. J.; Rezus, Y. L. A.; Müller, C.; Glaser, T.; Lovrincic, R.; Sun, Z.; Chen, Z.; Walsh, A.; Frost, J. M.; Jansen, T. L. C. Real-Time Observation of Organic Cation Reorientation in Methylammonium Lead Iodide Perovskites. *J. Phys. Chem. Lett.* **2015**, *6* (18), 3663−3669.
(244) Gong, J.; Yang, M.; Ma, X.; Schaller, R. D.; Liu, G.; Kong, L.; Yang, Y.; Beard, M. C.; Lesslie, M.; Dai, Y.; Huang, B.; Zhu, K.; Xu, T. Electron−Rotor Interaction in Organic−Inorganic Lead Iodide Perovskites Discovered by Isotope Effects. *J. Phys. Chem. Lett.* **2016**, *7* (15), 2879−2887.
(245) Motta, C.; El-Mellouhi, F.; Kais, S.; Tabet, N.; Alharbi, F.; Sanvito, S. Revealing the Role of Organic Cations in Hybrid Halide Perovskite $CH_3NH_3PbI_3$. *Nat. Commun.* **2015**, *6* (1), 7026.
(246) Varadwaj, P. R.; Varadwaj, A.; Marques, H. M.; Yamashita, K. Significance of hydrogen bonding and other noncovalent interactions in determining octahedral tilting in the $CH_3NH_3PbI_3$ hybrid organic-inorganic halide perovskite solar cell semiconductor. *Sci. Rep.* **2019**, *9* (1), 50.
(247) Cui, B.-B.; Han, Y.; Huang, B.; Zhao, Y.; Wu, X.; Liu, L.; Cao, G.; Du, Q.; Liu, N.; Zou, W.; Sun, M.; Wang, L.; Liu, X.; Wang, J.; Zhou, H.; Chen, Q. Locally collective hydrogen bonding isolates lead octahedra for white emission improvement. *Nat. Commun.* **2019**, *10* (1), 5190.
(248) Furukawa, Y.; Nakamura, D. Cationic Dynamics in the Crystalline Phases of $(CH_3NH_3)PbX_3$ (X: Cl, Br) as Studied by Proton Magnetic Resonance Techniques. *Z. Naturforsch., A: Phys. Sci.* **1989**, *44*, 1122−1126.
(249) Weller, M. T.; Weber, O. J.; Henry, P. F.; Di Pumpo, A. M.; Hansen, T. C. Complete structure and cation orientation in the perovskite photovoltaic methylammonium lead iodide between 100 and 352 K. *Chem. Commun.* **2015**, *51* (20), 4180−4183.
(250) Mozur, E. M.; Hope, M. A.; Trowbridge, J. C.; Halat, D. M.; Daemen, L. L.; Maughan, A. E.; Prisk, T. R.; Grey, C. P.; Neilson, J. R. Cesium Substitution Disrupts Concerted Cation Dynamics in Formamidinium Hybrid Perovskites. *Chem. Mater.* **2020**, *32* (14), 6266−6277.
(251) Franssen, W. M. J.; van Heumen, C. M. M.; Kentgens, A. P. M. Structural Investigations of $MA_{1-x}DMA_xPbI_3$ Mixed-Cation Perovskites. *Inorg. Chem.* **2020**, *59* (6), 3730−3739.
(252) Kanwat, A.; Yantara, N.; Ng, Y. F.; Hooper, T. J. N.; rana, p. j. s.; Febriansyah, B.; Harikesh, P. C.; Salim, T.; Vashishtha, P.; Mhaisalkar, S. G.; Mathews, N. Stabilizing the Electroluminescence of Halide Perovskites with Potassium Passivation. *ACS Energy Lett.* **2020**, *5* (6), 1804−1813.
(253) Grottel, M.; Szafrański, M.; Pająk, Z. NMR Study of Cation Motion in Guanidinium Iodoplumbates. *Z. Naturforsch., A: Phys. Sci.* **1997**, *52*, 783−788.
(254) Ueda, T.; Shimizu, K.; Ohki, H.; Okuda, T. ^{13}C CP/MAS NMR Study of the Layered Compounds $[C_6H_5CH_2CH_2NH_3]_2[CH_3NH_3]_{n-1}Pbnl_{3n+1}$ (n = 1, 2). *Z. Naturforsch., A: Phys. Sci.* **1996**, *51*, 910−914.
(255) Tremblay, M.-H.; Thouin, F.; Leisen, J.; Bacsa, J.; Srimath Kandada, A. R.; Hoffman, J. M.; Kanatzidis, M. G.; Mohite, A. D.; Silva, C.; Barlow, S.; Marder, S. R. $(4NPEA)_2PbI_4$ (4NPEA = 4-Nitrophenylethylammonium): Structural, NMR, and Optical Properties of a 3 × 3 Corrugated 2D Hybrid Perovskite. *J. Am. Chem. Soc.* **2019**, *141* (11), 4521−4525.
(256) Hong, L.; Milić, J. V.; Ahlawat, P.; Mladenović, M.; Kubicki, D. J.; Jahanabkhshi, F.; Ren, D.; Gélvez-Rueda, M. C.; Ruiz-Preciado, M. A.; Ummadisingu, A.; Liu, Y.; Tian, C.; Pan, L.; Zakeeruddin, S. M.; Hagfeldt, A.; Grozema, F. C.; Rothlisberger, U.; Emsley, L.; Han, H.; Graetzel, M. Guanine-Stabilized Formamidinium Lead Iodide Perovskites. *Angew. Chem., Int. Ed.* **2020**, *59* (12), 4691−4697.
(257) Gong, X.; Voznyy, O.; Jain, A.; Liu, W.; Sabatini, R.; Piontkowski, Z.; Walters, G.; Bappi, G.; Nokhrin, S.; Bushuyev, O.; Yuan, M.; Comin, R.; McCamant, D.; Kelley, S. O.; Sargent, E. H. Electron−phonon interaction in efficient perovskite blue emitters. *Nat. Mater.* **2018**, *17* (6), 550−556.
(258) Lim, A. R.; Jeong, S. Y. Twin Structure by ^{133}Cs NMR in Ferroelastic $CsPbCl_3$ Crystal. *Solid State Commun.* **1999**, *110* (3), 131−136.
(259) Lim, A. R.; Jeong, S.-Y. Ferroelastic Phase Transition and Twin Structure by ^{133}Cs NMR in a $CsPbCl_3$ Single Crystal. *Phys. B* **2001**, *304* (1), 79−85.
(260) Ran Lim, A.; Gyoo Kim, I. Phase Transition Study by using ^{133}Cs and ^{207}Pb Nuclear Magnetic Resonance in a $CsPbCl_3$ Single Crystal. *J. Phys. Soc. Jpn.* **2004**, *73* (2), 475−479.
(261) Chabin, M.; Gilletta, F. Theoretical Investigation of the Ferroelastic Domain Structure in Cesium Lead Chloride in the Monoclinic Phase. *J. Appl. Crystallogr.* **1980**, *13* (6), 533−538.
(262) Chabin, M.; Gilletta, F. Experiment Investigation of the Ferroelastic Domain Structure in Cesium Lead Chloride in the Monoclinic Phase. *J. Appl. Crystallogr.* **1980**, *13* (6), 539−543.
(263) Shin, E. J.; Jeong, H. K.; Kim, S. Y.; Jeong, J. The Orientation of Ferroelastic Domain in Single Crystal, $CsPbCl_3$. *J. Korean Assoc. Cryst. Growth* **1997**, *7* (1), 117−225.
(264) Ran Lim, A.; Jeong, S.-Y. Ferroelastic Phase Transition of $CsPbCl_3$ Single Crystals Studied by External Stress. *Phys. B* **1998**, *245* (3), 277−281.
(265) Hanrahan, M. P.; Men, L.; Rosales, B. A.; Vela, J.; Rossini, A. J. Sensitivity-Enhanced ^{207}Pb Solid-State NMR Spectroscopy for the Rapid, Non-Destructive Characterization of Organolead Halide Perovskites. *Chem. Mater.* **2018**, *30* (20), 7005−7015.
(266) Rosales, B. A.; Hanrahan, M. P.; Boote, B. W.; Rossini, A. J.; Smith, E. A.; Vela, J. Lead Halide Perovskites: Challenges and Opportunities in Advanced Synthesis and Spectroscopy. *ACS Energy Lett.* **2017**, *2* (4), 906−914.
(267) Rosales, B. A.; Men, L.; Cady, S. D.; Hanrahan, M. P.; Rossini, A. J.; Vela, J. Persistent Dopants and Phase Segregation in Organolead Mixed-Halide Perovskites. *Chem. Mater.* **2016**, *28* (19), 6848−6859.
(268) Askar, A. M.; Karmakar, A.; Bernard, G. M.; Ha, M.; Terskikh, V. V.; Wiltshire, B. D.; Patel, S.; Fleet, J.; Shankar, K.; Michaelis, V. K. Composition-Tunable Formamidinium Lead Mixed Halide Perovskites via Solvent-Free Mechanochemical Synthesis: Decoding the Pb Environments Using Solid-State NMR Spectroscopy. *J. Phys. Chem. Lett.* **2018**, *9* (10), 2671−2677.
(269) Karmakar, A.; Askar, A. M.; Bernard, G. M.; Terskikh, V. V.; Ha, M.; Patel, S.; Shankar, K.; Michaelis, V. K. Mechanochemical Synthesis of Methylammonium Lead Mixed−Halide Perovskites: Unraveling the Solid-Solution Behavior Using Solid-State NMR. *Chem. Mater.* **2018**, *30* (7), 2309−2321.
(270) Aebli, M.; Piveteau, L.; Nazarenko, O.; Benin, B. M.; Krieg, F.; Verel, R.; Kovalenko, M. V. Lead-Halide Scalar Couplings in ^{207}Pb NMR of $APbX_3$ Perovskites (A = Cs, Methylammonium, Formamidinium; X = Cl, Br, I). *Sci. Rep.* **2020**, *10* (1), 8229.
(271) Walsh, A.; Stranks, S. D. Taking control of ion transport in halide perovskite solar cells. *ACS Energy Lett.* **2018**, *3* (8), 1983−1990.
(272) Nazarenko, O.; Kotyrba, M. R.; Yakunin, S.; Aebli, M.; Rainò, G.; Benin, B. M.; Wörle, M.; Kovalenko, M. V. Guanidinium-Formamidinium Lead Iodide: A Layered Perovskite-Related Compound with Red Luminescence at Room Temperature. *J. Am. Chem. Soc.* **2018**, *140* (11), 3850−3853.
(273) Aebli, M.; Benin, B.; McCall, K. M.; Morad, V.; Thöny, D.; Grützmacher, H.; Kovalenko, M. V. White $CsPbBr_3$: Characterizing the One-Dimensional Cesium Lead Bromide Polymorph. *Helv. Chim. Acta* **2020**, *103*, No. e2000080.
(274) Bernard, G. M.; Goyal, A.; Miskolzie, M.; McKay, R.; Wu, Q.; Wasylishen, R. E.; Michaelis, V. K. Methylammonium Lead Chloride: A Sensitive Sample for an Accurate NMR Thermometer. *J. Magn. Reson.* **2017**, *283*, 14−21.
(275) Takahashi, T.; Kawashima, H.; Sugisawa, H.; Toshihide, B. ^{207}Pb Chemical Shift Thermometer at High Temperature for Magic Angle Spinning Experiments. *Solid State Nucl. Magn. Reson.* **1999**, *15* (2), 119−123.

https://dx.doi.org/10.1021/jacs.0c07338
J. Am. Chem. Soc. 2020, 142, 19413−19437

(276) Ullmann, H. *Strukturchemische und MAS-NMR-Spektroskopische Untersuchungen mit Quantenchemischen Berechnungen von Binären, Ternären und Quaternären Blei(II)-Halogeniden*; Herbert Utz Verlag Wissenschaft: Munich, 1998.
(277) Askar, A. M.; Bernard, G. M.; Wiltshire, B.; Shankar, K.; Michaelis, V. K. Multinuclear Magnetic Resonance Tracking of Hydro, Thermal, and Hydrothermal Decomposition of $CH_3NH_3PbI_3$. *J. Phys. Chem. C* **2017**, *121* (2), 1013−1024.
(278) Lermer, C.; Birkhold, S. T.; Moudrakovski, I. L.; Mayer, P.; Schoop, L. M.; Schmidt-Mende, L.; Lotsch, B. V. Toward Fluorinated Spacers for MAPI-Derived Hybrid Perovskites: Synthesis, Characterization, and Phase Transitions of $(FC_2H_4NH_3)_2PbCl_4$. *Chem. Mater.* **2016**, *28* (18), 6560−6566.
(279) Ramsey, N. F. Magnetic Shielding of Nuclei in Molecules. *Phys. Rev.* **1950**, *78* (6), 699−703.
(280) Tomaselli, M.; Yarger, J. L.; Bruchez, M.; Havlin, R. H.; deGraw, D.; Pines, A.; Alivisatos, A. P. NMR Study of InP Quantum Dots: Surface Structure and Size Effects. *J. Chem. Phys.* **1999**, *110* (18), 8861−8864.
(281) Piveteau, L.; Dirin, D. N.; Gordon, C. P.; Walder, B. J.; Ong, T.-C.; Emsley, L.; Copéret, C.; Kovalenko, M. V. Colloidal-ALD-Grown Core/Shell CdSe/CdS Nanoplatelets as Seen by DNP Enhanced PASS−PIETA NMR Spectroscopy. *Nano Lett.* **2020**, *20* (5), 3003−3018.
(282) Thayer, A. M.; Steigerwald, M. L.; Duncan, T. M.; Douglass, D. C. NMR Study of Semiconductor Molecular Clusters. *Phys. Rev. Lett.* **1988**, *60* (25), 2673−2676.
(283) Piveteau, L.; Ong, T.-C.; Walder, B. J.; Dirin, D. N.; Moscheni, D.; Schneider, B.; Bär, J.; Protesescu, L.; Masciocchi, N.; Guagliardi, A.; Emsley, L.; Copéret, C.; Kovalenko, M. V. Resolving the Core and the Surface of CdSe Quantum Dots and Nanoplatelets Using Dynamic Nuclear Polarization Enhanced PASS−PIETA NMR Spectroscopy. *ACS Cent. Sci.* **2018**, *4* (9), 1113−1125.
(284) Bernard, G. M.; Michaelis, V. K. Lead-207 NMR Spectroscopy at 1.4 T: Application of Benchtop Instrumentation to a Challenging I = 1/2 Nucleus. *Magn. Reson. Chem.* **2020**, 1−10.
(285) Ruiz-Preciado, M. A.; Kubicki, D. J.; Hofstetter, A.; McGovern, L.; Futscher, M. H.; Ummadisingu, A.; Gershoni-Poranne, R.; Zakeeruddin, S. M.; Ehrler, B.; Emsley, L.; Milić, J. V.; Grätzel, M. Supramolecular Modulation of Hybrid Perovskite Solar Cells via Bifunctional Halogen Bonding Revealed by Two-Dimensional ^{19}F Solid-State NMR Spectroscopy. *J. Am. Chem. Soc.* **2020**, *142* (3), 1645−1654.
(286) Abate, A.; Saliba, M.; Hollman, D. J.; Stranks, S. D.; Wojciechowski, K.; Avolio, R.; Grancini, G.; Petrozza, A.; Snaith, H. J. Supramolecular Halogen Bond Passivation of Organic−Inorganic Halide Perovskite Solar Cells. *Nano Lett.* **2014**, *14* (6), 3247−3254.
(287) Bi, S.; Wang, H.; Zhou, J.; You, S.; Zhang, Y.; Shi, X.; Tang, Z.; Zhou, H. Halogen bonding reduces intrinsic traps and enhances charge mobilities in halide perovskite solar cells. *J. Mater. Chem. A* **2019**, *7* (12), 6840−6848.
(288) Kaliaperumal, R.; Sears, R. E. J.; Finch, C. B. ^{19}F shielding anisotropy in $RbCaF_3$. *J. Chem. Phys.* **1987**, *87* (1), 68−72.
(289) Kaliaperumal, R.; Sears, R. E. J. ^{19}F shielding anisotropy in $KMgF_3$. *J. Chem. Phys.* **1988**, *88* (2), 1468−1469.
(290) Okuda, T.; Fukutonh, S.; Takesako, K.; Ohki, H.; Yamada, K. Fluoride Ion Conductors $RPbF_3$ (R = Rb, Cs) Studied by X-ray Diffraction and NMR. *Solid State Ionics* **2002**, 569−574.
(291) Payne, R. E.; Forman, R. A.; Kahn, A. H. Nuclear Magnetic Resonance in $RbMnF_3$. *J. Chem. Phys.* **1965**, *42* (11), 3806−3808.
(292) Grosescu, R.; Haeberlen, U. The Nuclear Magnetic Shielding of the ^{19}F-Nuclei in $KZnF_3$. *Z. Naturforsch., A: Phys. Sci.* **1985**, *40* (3), 283−293.
(293) Petrov, M. P.; Nedlin, G. M. Spin-Density Space Oscillations and Hyperfine Interaction in $RbCoF_3$. *J. Appl. Phys.* **1968**, *39* (2), 1012−1014.
(294) Smolenskii, G. A.; Petrov, M. P.; Pisarev, R. V. Spin-Density Distribution and Electronic Structure in Fluorides with the Perovskite Structure (ABF_3, where A = Na, Rb; B = Mn, Ni, Co). *J. Appl. Phys.* **1967**, *38* (3), 1269−1271.
(295) Engelsberg, M.; Rezende, S. M.; Soares, E. A. ^{19}F spin-lattice relaxation in antiferromagnets with the perovskite structure. *J. Appl. Phys.* **1979**, *50* (B3), 1929−1931.
(296) Cai, S.-H.; Yu, X.-Y.; Chen, Z.; Wan, H.-L. Theoretical study on ^{19}F magnetic shielding constants of some metal fluorides. *Magn. Reson. Chem.* **2003**, *41* (11), 902−907.
(297) Bureau, B.; Silly, G.; Buzaré, J. Y.; Emery, J. Superposition model for 19F isotropic chemical shift in ionic fluorides: from basic metal fluorides to transition metal fluoride glasses. *Chem. Phys.* **1999**, *249* (1), 89−104.
(298) Walker, M. B.; Stevenson, R. W. H. Nuclear magnetic resonance in $RbMnF_3$. *Proc. Phys. Soc., London* **1966**, *87* (1), 35−43.
(299) Elwell, D. ^{19}F nuclear magnetic resonance in some paramagnetic fluorides. *Proc. Phys. Soc., London* **1964**, *84* (3), 409−415.
(300) Bouznik, V. M.; Gabuda, S. P. Magnetic Screening of ^{19}F Nuclei in Perovskite $KMgF_3$. *Spectrosc. Lett.* **1969**, *2* (6), 185−189.
(301) Moskvin, O. I.; Voronov, V. N.; Vopilov, E. A.; Buznik, V. M. A study of the ^{19}F NMR chemical shifts in perovskites ABF_3. *J. Struct. Chem.* **1979**, *20* (3), 457−459.
(302) Schütz, F.; Lange, L.; Scheurell, K.; Scholz, G.; Kemnitz, E. Synthesis and Characterization of Perovskite-Type $[K_{1-x}Na_x]MgF_3$ Mixed Phases via the Fluorolytic Sol-Gel Synthesis. *Crystals* **2018**, *8* (2), 66.
(303) Martin, C. D.; Chaudhuri, S.; Grey, C. P.; Parise, J. B. Effect of A-site cation radius on ordering of BX_6 octahedra in $(K,Na)MgF_3$ perovskite. *Am. Mineral.* **2005**, *90* (10), 1522−1533.
(304) Düvel, A.; Wegner, S.; Efimov, K.; Feldhoff, A.; Heitjans, P.; Wilkening, M. Access to metastable complex ion conductors viamechanosynthesis: preparation, microstructure and conductivity of $(Ba,Sr)LiF_3$ with inverse perovskite structure. *J. Mater. Chem.* **2011**, *21* (17), 6238−6250.
(305) Kapturczak, J.; Pajak, Z.; Wachowski, L. ^1H and ^{19}F NMR in paramagnetic fluoroperovskite structures of $NH_4Co_xMg_{1-x}F_3$. *J. Phys. C: Solid State Phys.* **1986**, *19* (18), 3433−3441.
(306) Ahrens, M.; Scholz, G.; Kemnitz, E. Synthesis and Crystal Structure of $RbKLiAlF_6$ − the First Al-Elpasolite with Three Different Alkali Metals. *Z. Anorg. Allg. Chem.* **2008**, *634* (15), 2978−2981.
(307) Veenendaal, E. J.; Brom, H. B. Hyperfine splitting in the elpasolite Cs_2NaHoF_6, measured by enhanced ^{165}Ho NMR. *Physica B +C* **1982**, *113* (1), 118−120.
(308) Choy, J.-H.; Kim, J.-Y.; Kim, S.-J.; Sohn, J.-S.; Han, O. H. New Dion−Jacobson-Type Layered Perovskite Oxyfluorides, $ASrNb_2O_6F$ (A = Li, Na, and Rb). *Chem. Mater.* **2001**, *13* (3), 906−912.
(309) Chadwick, A. V.; Strange, J. H.; Ranieri, G. A.; Terenzi, M. Studies of ionic motion in perovskite fluorides. *Solid State Ionics* **1983**, *9−10*, 555−558.
(310) Bryce, D. L.; Widdifield, C. M.; Chapman, R. P.; Attrell, R. J. Chlorine, Bromine, and Iodine Solid-State NMR. *eMagRes.* **2007**, DOI: 10.1002/9780470034590.emrstm1214.
(311) Widdifield, C. M.; Chapman, R. P.; Bryce, D. L. Chapter 5 Chlorine, Bromine, and Iodine Solid-State NMR Spectroscopy. *Annu. Rep. NMR Spectrosc.* **2009**, *66*, 195−326.
(312) Szell, P. M. J.; Bryce, D. L. Chapter Three - Recent Advances in Chlorine, Bromine, and Iodine Solid-State NMR Spectroscopy. *Annu. Rep. NMR Spectrosc.* **2015**, *84*, 115−162.
(313) Das, T. P.; Hahn, E. L. *Nuclear Quadrupole Resonance Spectroscopy*; Academic Press, Inc.: London, 1958.
(314) Dean, C. Zeeman Splitting of Nuclear Quadrupole Resonances. *Phys. Rev.* **1954**, *96* (4), 1053−1059.
(315) Bersohn, R. Nuclear Electric Quadrupole Spectra in Solids. *J. Chem. Phys.* **1952**, *20* (10), 1505−1509.
(316) Cohen, M. H. Nuclear Quadrupole Spectra in Solids. *Phys. Rev.* **1954**, *96* (5), 1278−1284.
(317) Semin, G. K. On Solving Secular Equations for Half-Integer Spins (I = 5/2, 7/2, and 9/2) in NQR Spectroscopy. *Russ. J. Phys. Chem.* **2007**, *81* (1), 38−46.

(318) Man, P. P. Quadrupolar Interactions. *eMagRes.* **2007**, DOI: 10.1002/9780470034590.emrstm0429.pub2.
(319) Vega, A. J. Quadrupolar Nuclei in Solids. *eMagRes.* **2007**, DOI: 10.1002/9780470034590.emrstm0431.pub2.
(320) Piveteau, L.; Aebli, M.; Yazdani, N.; Millen, M.; Korosec, L.; Krieg, F.; Benin, B. M.; Morad, V.; Piveteau, C.; Shiroka, T.; Comas-Vives, A.; Copéret, C.; Lindenberg, A. M.; Wood, V.; Verel, R.; Kovalenko, M. V. Bulk and Nanocrystalline Cesium Lead-Halide Perovskites as Seen by Halide Magnetic Resonance. *ACS Cent. Sci.* **2020**, *6* (7), 1138−1149.
(321) Harris, R. K.; Becker, E. D.; Cabral de Menezes, S. M.; Goodfellow, R.; Granger, P. NMR Nomenclature: Nuclear Spin Properties and Conventions for Chemical Shifts: IUPAC Recommendations 2001. *Solid State Nucl. Magn. Reson.* **2002**, *22* (4), 458−483.
(322) Tovborg-Jensen, N. NQR Investigation of Phase Transitions in Cesium Plumbochloride. *J. Chem. Phys.* **1969**, *50* (1), 559−560.
(323) van Driel, H. M.; Armstrong, R. L. ^{35}Cl Spin-Lattice Relaxation Study of Phase Tansitions in $CsPbCl_3$. *Phys. Rev. B* **1975**, *12* (3), 839−841.
(324) Møller, C. K. A Phase Transition in Caesium Plumbochloride. *Nature* **1957**, *180* (4593), 981−982.
(325) Møller, C. K. Crystal Structure and Photoconductivity of Caesium Plumbohalides. *Nature* **1958**, *182* (4647), 1436−1436.
(326) Armstrong, R. L. Pure Nuclear Quadrupole Resonance Studies of Structural Phase Transitions. *J. Magn. Reson.* **1975**, *20* (2), 214−231.
(327) Cohen, M. I.; Young, K. F.; Chang, T. T.; Brower, W. S., Jr. Phase Transitions in $CsPbCl_3$. *J. Appl. Phys.* **1971**, *42* (13), 5267−5272.
(328) Weber, D. $CH_3NH_3PbX_3$, a Pb(II)-System with Cubic Perovskite Structure. *Z. Naturforsch., B: J. Chem. Sci.* **1978**, *33b*, 1443−1445.
(329) Protesescu, L.; Yakunin, S.; Bodnarchuk, M. I.; Krieg, F.; Caputo, R.; Hendon, C. H.; Yang, R. X.; Walsh, A.; Kovalenko, M. V. Nanocrystals of Cesium Lead Halide Perovskites ($CsPbX_3$, X = Cl, Br, and I): Novel Optoelectronic Materials Showing Bright Emission with Wide Color Gamut. *Nano Lett.* **2015**, *15* (6), 3692−3696.
(330) Becker, M. A.; Vaxenburg, R.; Nedelcu, G.; Sercel, P. C.; Shabaev, A.; Mehl, M. J.; Michopoulos, J. G.; Lambrakos, S. G.; Bernstein, N.; Lyons, J. L.; Stöferle, T.; Mahrt, R. F.; Kovalenko, M. V.; Norris, D. J.; Rainò, G.; Efros, A. L. Bright triplet excitons in caesium lead halide perovskites. *Nature* **2018**, *553* (7687), 189−193.
(331) Boles, M. A.; Ling, D.; Hyeon, T.; Talapin, D. V. The Surface Science of Nanocrystals. *Nat. Mater.* **2016**, *15* (2), 141−153.
(332) Kovalenko, M. V.; Manna, L.; Cabot, A.; Hens, Z.; Talapin, D. V.; Kagan, C. R.; Klimov, V. I.; Rogach, A. L.; Reiss, P.; Milliron, D. J.; Guyot-Sionnnest, P.; Konstantatos, G.; Parak, W. J.; Hyeon, T.; Korgel, B. A.; Murray, C. B.; Heiss, W. Prospects of Nanoscience with Nanocrystals. *ACS Nano* **2015**, *9* (2), 1012−1057.
(333) Hens, Z.; Martins, J. C. A Solution NMR Toolbox for Characterizing the Surface Chemistry of Colloidal Nanocrystals. *Chem. Mater.* **2013**, *25* (8), 1211−1221.
(334) De Roo, J.; Ibáñez, M.; Geiregat, P.; Nedelcu, G.; Walravens, W.; Maes, J.; Martins, J. C.; Van Driessche, I.; Kovalenko, M. V.; Hens, Z. Highly Dynamic Ligand Binding and Light Absorption Coefficient of Cesium Lead Bromide Perovskite Nanocrystals. *ACS Nano* **2016**, *10* (2), 2071−2081.
(335) Grisorio, R.; Di Clemente, M. E.; Fanizza, E.; allegretta, i.; Altamura, D.; Striccoli, M.; Terzano, R.; Giannini, C.; Irimia-Vladu, M.; Suranna, G. P. Exploring the Surface Chemistry of Cesium Lead Halide Perovskite Nanocrystals. *Nanoscale* **2019**, *11*, 986−999.
(336) Smock, S. R.; Williams, T. J.; Brutchey, R. L. Quantifying the Thermodynamics of Ligand Binding to CsPbBr3 Quantum Dots. *Angew. Chem., Int. Ed.* **2018**, *57* (36), 11711−11715.
(337) Chen, Y.; Smock, S. R.; Flintgruber, A. H.; Perras, F. A.; Brutchey, R. L.; Rossini, A. J. The Surface Termination of $CsPbBr_3$ Perovskite Quantum Dots Determined by Solid-State NMR Spectroscopy. *J. Am. Chem. Soc.* **2020**, *142* (13), 6117−6127.
(338) Brenner, P.; Bar-On, O.; Jakoby, M.; Allegro, I.; Richards, B. S.; Paetzold, U. W.; Howard, I. A.; Scheuer, J.; Lemmer, U. Continuous wave amplified spontaneous emission in phase-stable lead halide perovskites. *Nat. Commun.* **2019**, *10* (1), 988.
(339) Wang, L.; Meng, L.; Chen, L.; Huang, S.; Wu, X.; Dai, G.; Deng, L.; Han, J.; Zou, B.; Zhang, C.; Zhong, H. Ultralow-Threshold and Color-Tunable Continuous-Wave Lasing at Room-Temperature from In Situ Fabricated Perovskite Quantum Dots. *J. Phys. Chem. Lett.* **2019**, *10* (12), 3248−3253.
(340) Shrestha, S.; Fischer, R.; Matt, G. J.; Feldner, P.; Michel, T.; Osvet, A.; Levchuk, I.; Merle, B.; Golkar, S.; Chen, H.; Tedde, S. F.; Schmidt, O.; Hock, R.; Rührig, M.; Göken, M.; Heiss, W.; Anton, G.; Brabec, C. J. High-performance direct conversion X-ray detectors based on sintered hybrid lead triiodide perovskite wafers. *Nat. Photonics* **2017**, *11* (7), 436−440.
(341) Sutherland, B. R.; Hoogland, S.; Adachi, M. M.; Wong, C. T. O.; Sargent, E. H. Conformal Organohalide Perovskites Enable Lasing on Spherical Resonators. *ACS Nano* **2014**, *8* (10), 10947−10952.
(342) Xiang, W.; Wang, Z.; Kubicki, D. J.; Tress, W.; Luo, J.; Prochowicz, D.; Akin, S.; Emsley, L.; Zhou, J.; Dietler, G.; Grätzel, M.; Hagfeldt, A. Europium-Doped $CsPbI_2Br$ for Stable and Highly Efficient Inorganic Perovskite Solar Cells. *Joule* **2019**, *3* (1), 205−214.
(343) Miller, J. B.; Barrall, G. A. Explosives Detection with Nuclear Quadrupole Resonance: An Emerging Technology will Help to Uncover Land Mines and Terrorist Bombs. *Am. Sci.* **2005**, *93* (1), 50−57.
(344) Balchin, E.; Malcolme-Lawes, D. J.; Poplett, I. J. F.; Rowe, M. D.; Smith, J. A. S.; Pearce, G. E. S.; Wren, S. A. C. Potential of Nuclear Quadrupole Resonance in Pharmaceutical Analysis. *Anal. Chem.* **2005**, *77* (13), 3925−3930.
(345) Pérez, S. C.; Cerioni, L.; Wolfenson, A. E.; Faudone, S.; Cuffini, S. L. Utilization of pure nuclear quadrupole resonance spectroscopy for the study of pharmaceutical crystal forms. *Int. J. Pharm.* **2005**, *298* (1), 143−152.
(346) Trontelj, Z.; Pirnat, J.; Jazbinšek, V.; Lužnik, J.; Srčič, S.; Lavrič, Z.; Beguš, S.; Apih, T.; Žagar, V.; Seliger, J. Nuclear Quadrupole Resonance (NQR)—A Useful Spectroscopic Tool in Pharmacy for the Study of Polymorphism. *Crystals* **2020**, *10* (6), 450.